



SAPIENZA  
UNIVERSITÀ DI ROMA

---

MATHEMATICS DEPARTMENT 'GUIDO CASTELNUOVO'

Ph.D. Program in Mathematics  
XXXII cycle

Mathematical modeling  
and numerical investigation  
of traveling waves  
in biomedicine and geophysics

Advisor:  
Corrado Mascia

Candidate:  
Pierfrancesco Moschetta

Co-Advisor:  
Chiara Simeoni

Academic Year 2018-2019



# Contents

<b>1</b>	<b>Introduction</b>	<b>5</b>
1.1	Motivations, presentation and aims . . . . .	5
1.2	Mathematical framework and tools . . . . .	11
<b>2</b>	<b>Mathematical modeling of EMT-MET</b>	<b>17</b>
2.1	Introduction . . . . .	17
2.2	A simple PDE model for phase transitions . . . . .	19
2.2.1	Adimensionalization . . . . .	20
2.2.2	Space independent solutions . . . . .	21
2.2.3	Stability of steady states . . . . .	24
2.2.4	Planar solutions . . . . .	25
2.2.5	An identity for the wave speed . . . . .	26
2.3	Numerical experiments . . . . .	28
2.3.1	Discretization algorithm . . . . .	29
2.3.2	Numerical evaluation of the propagation speed . . . . .	30
2.3.3	Computational results . . . . .	33
2.3.4	Sensitivity analysis with respect to $\tau$ and $\lambda$ . . . . .	36
<b>3</b>	<b>Study of the Gatenby-Gawlinski model</b>	<b>39</b>
3.1	Introduction . . . . .	39
3.2	The Gatenby-Gawlinski model . . . . .	42
3.3	The numerical algorithm . . . . .	44
3.4	One-dimensional simulation results . . . . .	47
3.5	Some useful model reductions . . . . .	53
3.5.1	Two-equations-based model reduction . . . . .	54
3.5.2	One-equation-based model reduction . . . . .	57
3.6	Multidimensional simulations . . . . .	65
3.6.1	Two-dimensional experiments . . . . .	67

3.6.2	Three-dimensional experiments . . . . .	72
<b>4</b>	<b>Study of the Burridge-Knopoff model</b>	<b>77</b>
4.1	Introduction . . . . .	77
4.2	The Burridge-Knopoff model . . . . .	79
4.3	Numerical algorithm and its reliability . . . . .	82
4.3.1	Numerical adjustment . . . . .	84
4.3.2	One block . . . . .	86
4.3.3	A bit more complex configuration . . . . .	88
4.3.4	More blocks and the Gutenberg-Richter law . . . . .	89
4.4	Wave speed estimate and almost convergence . . . . .	94
	<b>Bibliography</b>	<b>98</b>
	<b>Sitography</b>	<b>107</b>

# Chapter 1

## Introduction

### 1.1 Motivations, presentation and aims

Applied Sciences field is doubtless one of the most promising and interesting contexts modern research is based on. As well as the advances made in each specific scientific framework, which go hand in hand with the impressive and constantly faster pace of technological development in recent years, a major contribution to the improvement of research results can be recognized in the mutual cooperation among different disciplines in approaching problems. In this scenario, a significant role is played by Applied Mathematics, whose transverse nature lends itself to accomplish the purpose of properly meeting and supporting other subjects requirements.

In this thesis, special emphasis is laid on the great progress achieved in the biomedical field through a fruitful cooperation with mathematics: specifically, mathematical modeling turns out to be a powerful tool of analysis experimental study might rely on in order to pursue investigation concerning cancer research. Nowadays, indeed, trials in cancer are one of the most challenging, interdisciplinary contexts and the possibility of improving strategies for approaching the subject to deliver better and faster results is at the order of the day. A lot of effort is particularly made with the aim of developing suitable models that could account for the processes leading to production and spread of cancerous cells. Although such techniques are bound by limitations that mathematical abstraction inevitably brings with it, recognition of their indispensability and relevance is increasingly growing among research groups: the remarkable contribution in terms of predicting cell evolution, potentially even diagnosing and forecasting treatments, is an effective research path worth being deeply investigated.

A valuable support to mathematical modeling, especially for biomedicine and cancer research, is provided by scientific computing: as a matter of fact, the pos-

sibility of performing even more reliable simulations with the help of suitable software and powerful devices, is playing a remarkable role for getting more detailed results both in the processing and post-processing phases. Indeed, after a preliminary stage consisting in framing the phenomenon object of study within the proper theoretical framework and in providing the resulting formalization, the discretization step is to be properly carried out by means of the most up-to-date procedures, thus producing best quality results for ensuring fruitful subsequent assessments and inspections by experts in the biomedical field. In this respect, the contribution made by investigating multidimensional configurations becomes extremely valuable to support experimental data, that is why, in this thesis, a lot of effort is spent on performing two-dimensional and three-dimensional simulations as well. Ultimately, the mathematical approach consists of three distinct aspects: analytical framing, numerical treatment and data post-processing, which are the stages to be referred to throughout the whole dissertation.

Concerning the conceptual point of view, in order to get the best contextualization, the so-called *Systems Biology* paradigm [2, 61, 62, 92] will be often relied on for approaching some biological problems. This kind of analysis turns out to change the reductionist perspective (breaking an entity down in order to approach the entire system through its elementary components) research is frequently ruled by: it allows to deal with complex biomedical dynamics by assuming the system as a whole, specifically, through an holistic idea by virtue of which the biomedical processes analysis cannot be exhausted considering the system as the mere sum of its components. That is why, instead of focusing on the role of individual agents, the main purpose is to define how essential components interact to characterize the collective dynamics. With particular reference to oncology, the Systems Biology approach is aimed to seize complexity in the genesis of cancer [12].

The thesis is organized as follows: after a brief summary concerning the main mathematical topics and tools, the core of the work essentially consists in introducing and analyzing two biomedical contexts related to cancer research. The first one involves the *Epithelial-to-Mesenchymal Transition* and its reverse process, the *Mesenchymal-to-Epithelial Transition* [92] (EMT and MET in short), which are crucial steps at the base of *morphogenesis* and, consequently, critical phenomena in terms of malignant features acquiring or losing for cancerous cells<sup>1</sup> (see Chapter 2); the second one takes into account the so-called *Warburg effect* [97, 98] and frames a biomedical stage in which the carcinogenesis has already occurred, thus focusing on tumour cells spreading within a healthy tissue (see Chapters 3). The dissertation is provided with a final section devoted to a further mathematical modeling theme

---

<sup>1</sup>The mathematical investigation has been greatly motivated by fruitful discussions with the researchers of the Systems Biology Group Lab [113] headed by prof. Bizzarri and settled at the Department of Experimental Medicine, Sapienza University of Rome (Italy), within the project *Phase Transitions in Biology through Mathematical Modelling*.

(see Chapter 4), which goes beyond the purely biomedical framework: indeed, on the heels of the thematic affinity concerning some mathematical topics to be relied on in the following, such as *traveling waves*, the geophysical field will be referred to in order to perform simulations about the earthquakes occurrences [14, 71]. The aim of this geophysical analysis also consists in exhibiting a further and effective proof about the versatility applied mathematics is characterized by, specifically in such a socially relevant field.

For the ease of the reader, the current section ends providing a synthetic and exhaustive framing concerning each of the main themes introduced above.

## EMT-MET

From a biomedical point of view, cell phenotypic differentiation is a crucial step for determining cancer onset and evolution. Concerning EMT, indeed, it is important to point out that this kind of transition allows epithelial cells, characterized by cohesion and strong junctions, to become scattered and acquire motility, namely the mesenchymal-like state, thus defining a potentially very suitable scenario in terms of malignant features spreading, as depicted in Figure 1.1. The possibility of inducing MET, namely the reverse process, by means of some external stimuli, is giving rise to perform promising studies at the base of which lies the ultimate ambition to revert an apparently already sealed fate for cells having acquired malignant features.

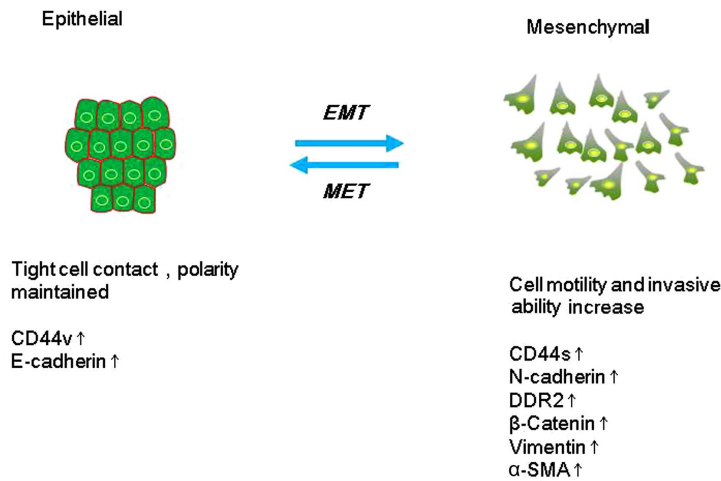


Figure 1.1. Epithelial and mesenchymal cells features and associated biomarkers (the image is taken from [105]).

In this work, taking advantage of mathematical modeling, EMT-MET analysis is carried out by exploiting a simplified one-dimensional hyperbolic-parabolic PDE model. The epithelial and mesenchymal phenotypes are the unknown functions and the main purpose consists in establishing the existence of traveling waves by means of numerical simulations. With the aim of estimating the propagating fronts speed, the so-called *LeVeque-Yee formula* [52] is invoked and used to validate an analytical identity specifically set up for such a PDE system provided with a nonlinear function assumed to be S-shaped. One of the most interesting results arising from the model object of investigation, lies in the possibility of reproducing the property of being invasive or not, according to the dependence on two control parameters, the relaxation time  $\tau$  and the invasiveness parameter  $\lambda$  respectively, whose influence is carefully checked through a sensitivity analysis. Numerical simulations, based on finite difference schemes [77, 78], are carried out by employing an Implicit-Explicit strategy. Both data processing phase and graphical results post-processing are performed by using Matlab [106].

Speaking about the perspectives, it would be interesting trying to develop a solid theoretical counterpart in order to prove the existence of traveling waves in the general framework  $\tau > 0$ : in this respect, a possible strategy might take advantage of *singular perturbation techniques*, taking as reference the parameter  $\tau$ . Moreover, the possibility of setting up a realistic quantitative model, capable of going beyond the detection of qualitative features, is extremely challenging and worth being deeply explored.

## Warburg effect

The phenomenological context concerning the Warburg effect relies on the experimental results achieved by Otto Warburg [97] in the 1920s, which essentially prove that tumour cells lean on anaerobic glycolysis, regardless of the available oxygen amount, for adenosine triphosphate production, thus causing lactic acid fermentation, as shown in Figure 1.2. Such a behaviour leads to the so-termed acid-mediated-invasion-hypothesis, whose mathematical modeling is realized by means of a three-equations-based reaction-diffusion system known as *Gatenby-Gawlinski model* [30, 32]. The main feature for mathematical investigation is the traveling waves existence [10, 11, 26, 32, 33, 34, 35, 93, 94].

In this dissertation, the Gatenby-Gawlinski model structural aspects are deeply investigated: in the one-dimensional case, taking into account a finite volume approximation (refer to [100], for instance) set up through an Implicit-Explicit strategy as far as the time discretization, considerable numerical and computational effort is made to show the onset of propagating fronts and estimate the associated wave speed by invoking the LeVeque-Yee formula. Furthermore, reasonable assumptions are considered in order to define some system reductions and numerical



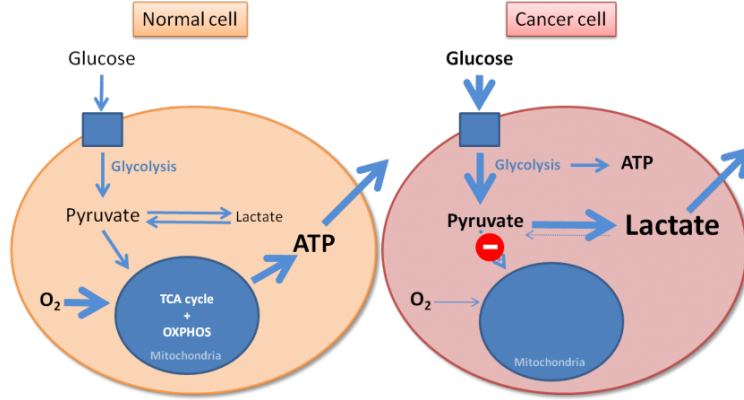


Figure 1.2. Difference between normal and cancer cells metabolism: healthy cells exploit oxidative phosphorylation to produce energy, while cancer cells employ anaerobic glycolysis (the image is taken from [107]).

evidence of the *sharpness* [84] of the fronts is provided for a one-equation-based reduction (see Chapter 3). All these results, achieved in the one-dimensional framework, are performed through Matlab.

For the full model case, two-dimensional as well as three-dimensional configurations are considered too: important qualitative aspects related to experimental observations are emphasized by means of a finite element approach [78] performed taking advantage of the COMSOL Multiphysics environment [108]. Concerning the post-processing stage for the three-dimensional graphical results, the choice has fallen into leaning on ParaView [109].

Future works might be conceived in order to further investigate the Gatenby-Gawliniski model on unstructured meshes, taking advantage of the general derivation with variable spatial mesh size proposed in this thesis for the finite volume strategy. Moreover, as concerns the system reductions field, it is currently under examination the possibility of extending the sharpness investigation with the aim of getting analytical and numerical results for the two-equations-based reduction. Finally, on the heels of the achievements reached through the multidimensional framework analysis, it is promising trying to improve the computational effectiveness by invoking the *parallel computation paradigm*.

## Geophysical context: earthquakes simulations

The geophysical field concerning earthquakes phenomena is explored by means of the so-called *Burridge-Knopoff model* [14], namely a spring-block model, defined by a system of ODEs provided with a discontinuous right hand side, which is

direct consequence of the *stick-slip dynamics* [13], whose contextualization on an earthquake fault is depicted in Figure 1.3.

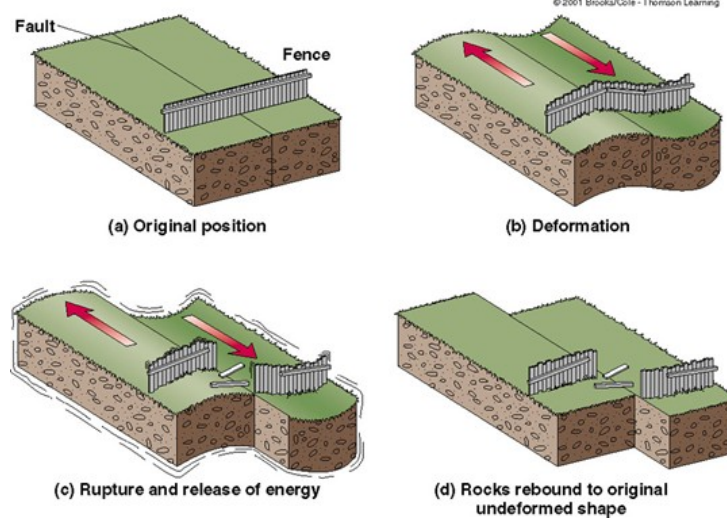


Figure 1.3. Stick-slip dynamics on a fault: the steady accumulation of stress characterizes the stick-phase, while the release of tension, through a seismic event, happens in the slip-phase (the image is taken from [110]).

In this thesis, numerical simulations are performed by relying on a *Predictor-Corrector strategy* [77], with the aim of proving the *almost convergence property* [8, 54] of the wave speeds for the Burridge-Knopoff model with velocity-weakening friction [15, 16, 17]. The propagating fronts speed approximation is computed by exploiting a suitable rearrangement of the LeVeque-Yee formula and numerical evidence of the almost convergence property is provided along with a consistent phenomenological explanation within the seismological context. Simulations are carried out employing the *Fortran language*, due to the increasing computational effort required as the size of the differential system grows up significantly, depending on the number of blocks involved; finally, the Matlab environment is considered for the post-processing phase of graphical results.

As far as the work perspectives, it is challenging trying to fathom the model with the aim of looking for other evidence related to the propagating fronts theory. Such an attempt is expected to be fruitful, due to the belonging of the model to a class of systems capable of producing traveling waves, as pointed out in [71].

## 1.2 Mathematical framework and tools

From a mathematical point of view, all the results related to the biomedical and geophysical problems mentioned in Section 1.1, are contextualized within the traveling waves theory, which is the analytical reference point the numerical core of the thesis is based on. Indeed, starting from the propagating fronts research area, by means of mathematical modeling, it is possible to set up a fruitful ground to carry out several and interesting numerical investigations. Furthermore, taking advantage of specific tools concerning scientific computing, qualitatively and quantitatively significant results are provided for processing data.

Nonlinear-reaction-diffusion models are taken into account for the PDE field and, as regards the numerical framework, the time discretization strategy essentially relies on the *IMEX approach*, namely Implicit-Explicit algorithms, thus resulting, for instance, in explicit approximations for nonlinear contributions and implicit treatments for the linear ones (see Chapter 2): the IMEX choice turns out to be very effective and showing its full potential is one of the key aims of this work. As a matter of fact, these methods allow to employ less expensive time steps compared to full explicit strategies, thus considerably reducing the computation effort without preventing results accuracy. Finally, concerning the spatial discretization, a wide variety of techniques is considered, embracing finite difference, finite element and finite volume schemes [77, 78, 100]. Actually, huge emphasis is placed on pursuing numerical investigations throughout the whole work: indeed, numerical strategies prove itself to be a very powerful tool to approach traveling fronts theory, due to it is often not possible to count on exact solutions.

With the aim of introducing the traveling waves analytical framework, a prototype example, whose solution can be explicitly computed [46], is now provided. Specifically, a scalar reaction-diffusion equation is taken into account, where  $u(x, t) \in \mathbb{R}$  is the unknown function and  $f(u)$  is a reaction term, such as  $f \in \mathcal{C}^2(\mathbb{R})$ , satisfying for some  $\alpha \in (0, 1)$  the following hypothesis:

- $f(0) = f(\alpha) = f(1) = 0$ ,
- $f'(0), f'(1) < 0$ ,
- $f(s) \neq 0 \quad \forall s \notin \{0, \alpha, 1\}$ .

A fitting choice for a reaction part whose trend perfectly matches the above requirements, consists in assuming a cubic form, namely  $f(u) = u(u - \alpha)(1 - u)$ , thus leading to the *bistable equation*:

$$\frac{\partial u}{\partial t} = \frac{\partial^2 u}{\partial x^2} + u(u - \alpha)(1 - u). \quad (1.1)$$

As regards the equation (1.1), let us assume  $\int_0^1 f > 0$ : the need for investigations about traveling fronts is justified as the question, concerning the way the transition from the steady state 0 towards the steady state 1 happens, arises. In this scenario, it is natural trying to look for a solution behaving as a propagating front of the form

$$u(x, t) = \phi(\xi) = \phi(x - ct),$$

being  $\phi : \mathbb{R} \rightarrow \mathbb{R}$  an increasing function such as  $\phi(-\infty) = 0, \phi(+\infty) = 1$  and  $c \in \mathbb{R}$  the correspondent wave speed. By imposing that  $\phi$  is a solution of (1.1), we get a nonlinear differential equation that reads as

$$\phi'' + c\phi' + \phi(\phi - \alpha)(1 - \phi) = 0,$$

which can be comfortably rewritten to become a system of first-order equations as follows

$$\begin{cases} \phi' = \psi \\ \psi' = -c\psi - \phi(\phi - \alpha)(1 - \phi). \end{cases} \quad (1.2)$$

At this stage, supposing  $\psi = D\phi(1 - \phi)$  with  $D \in \mathbb{R}$  to be determined (see [46]), the second equation in (1.2) looks like

$$D^2\phi(1 - \phi)(1 - 2\phi) + cD\phi(1 - \phi) + \phi(\phi - \alpha)(1 - \phi) = 0,$$

which, after standard manipulations, leads to

$$(1 - 2D^2)\phi + D^2 + cD - \alpha = 0.$$

The identity above is satisfied selecting  $c = (2\alpha - 1)/\sqrt{2}$  and  $D = 1/\sqrt{2}$ , thus producing the following Bernoulli differential equation:

$$\phi' = \frac{1}{\sqrt{2}}(\phi - \phi^2), \quad (1.3)$$

whose solution can be achieved imposing  $\theta(\xi) := 1/\phi(\xi)$ , resulting in the family of functions

$$\theta(\xi) = \exp\left(-\frac{\xi + C}{\sqrt{2}}\right) + 1. \quad (1.4)$$

Finally, taking advantage of (1.4), it is possible to infer that the solution for the bistable equation (1.1) is a traveling wave, whose speed is given by  $c = (2\alpha - 1)/\sqrt{2}$ , belonging to the family

$$u(x, t) = \frac{1}{\exp\left(-\frac{x - ct + C}{\sqrt{2}}\right) + 1}$$

where a specific function might be selected by assigning a Cauchy problem for (1.1).

The bistable equation is doubtless an interesting study case and a useful reference within the traveling fronts theory, but as said before, dealing with most of the problems arising from applications often involves being able to rely on numerical analysis, thus resulting in approximations and estimates. Concerning the traveling waves context, besides computing an approximated solution for the propagating fronts, estimating the associated wave speed is crucial as well. In this respect, the LeVeque-Yee formula [52], mentioned in Section 1.1, turns out to be one of the key topics discussed in the thesis: its use within the reaction-diffusion system environment (see Chapters 2 and 3) and the rearrangement proposed (see Chapter 4) to fit the ODE field, constitute original and effective applications for a tool being borrowed from the conservation laws context. Some guidance about its derivation is provided below.

Let us suppose to be interested in quantifying the wave speed at time  $t$  for a traveling wave, namely  $u(x, t)$ , by means of the LeVeque-Yee approximation, which is a space-averaged estimation. Starting from the analytical counterpart (see Chapter 2 for details), if  $\phi$  is meant to be a differentiable function suitable to describe the traveling front profile, we can state

$$\int_{\mathbb{R}} [\phi(\xi + h) - \phi(\xi)] d\xi = h(\phi_+ - \phi_-),$$

where  $h$  is an increment,  $\phi_+$  and  $\phi_-$  are the asymptotic states for the function  $\phi$  (heteroclinic traveling fronts). Given  $\Delta t > 0$ , by setting  $h = -c\Delta t$ , we get an integral equation for the propagation speed that reads as

$$c = \frac{1}{[\phi]\Delta t} \int_{\mathbb{R}} [\phi(\xi) - \phi(\xi - c\Delta t)] d\xi,$$

where  $[\phi] := \phi_+ - \phi_-$ .

At this stage, as previously observed in the bistable equation case, it is important to recall that a traveling front profile is related to the actual solution through the change of variable  $\xi = x - ct$ . Thus, in discrete form, the space-averaged wave speed estimation for the function  $u(x, t)$  over a uniform spatial mesh at time  $t^n$ , being  $\Delta x$  and  $\Delta t$  the fixed spatial and time steps respectively and  $u_i^n$  an approximation of  $u(x_i, t^n)$ , is given by

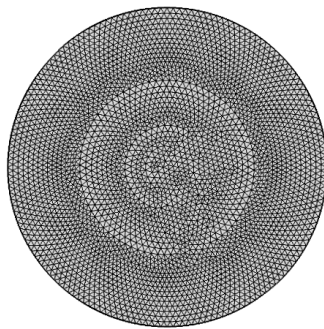
$$c^n = \frac{\Delta x}{[u]\Delta t} \sum_i (u_i^n - u_i^{n+1}), \quad (1.5)$$

with  $[u] := u_+ - u_-$ , where  $u_+$  and  $u_-$  are the stationary states of  $u(x, t)$ . Particular emphasis is to be given to a crucial point: the effectiveness of estimation (1.5) lies in its independence of the dynamics of the solutions produced by the underlying equation, that means independence from (1.1) in the bistable case. As a result, the LeVeque-Yee formula is always numerically computable.

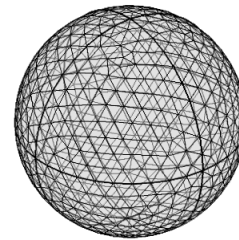
## Scientific computing tools: the COMSOL Multiphysics environment

The last part of this introductory chapter is devoted to describe the COMSOL Multiphysics environment, which turns out to be a very powerful resource in order to perform multidimensional simulations whose outcomes might be extremely useful in terms of experimental comparison, especially in the biomedical field. In this respect, the COMSOL software is employed for two-dimensional and three-dimensional simulations of the Gatenby-Gawlinski model in Chapter 3 and, concerning the graphical post-processing of three-dimensional data, a full volumetric representation is provided through a transparency technique implemented exploiting ParaView as visualization platform.

COMSOL Multiphysics allows benefiting from the advantages of an interactive environment specially designed for quickly accessing resources and tools by invoking advanced numerical methods based on finite element strategies. The range of applications encompasses mechanical, electromagnetic, fluid flow, heat transfer, acoustics, optics modeling and much more. It is possible both accounting for specific physics-based problems and taking advantage of the flexibility and generalization provided by the *Equation-Based Modeling section*, which allows building multiphysics models that suit best for the user. This last tool has widely been exploited in this work, due to the possibility of having complete control over the models underlying the biomedical context, which means capability of tailoring them to specific requirements and adding complexity according to user's tastes and needs.



(a) *two-dimensional grid*



(b) *three-dimensional grid*

Figure 1.4. Example of finite element mesh generation with COMSOL: triangular (a) and tetrahedral (b) meshes.

The COMSOL environments also allows to carefully take care of everything concerning the finite element mesh generation and refinement: in Figure 1.4, as an example, meshes suitably realized for arranging multidimensional biomedical simulations (see Chapter 3) are depicted, specifically, the case of triangular and tetrahedral grids for radial symmetric experimental domains.

As far as the models setting up, it is possible relying on weak and strong formulations for both stationary and time-dependent problems, where appropriate employing *Discontinuous Galerkin methods*, or selecting among different kinds of finite elements such as *Lagrange*, *Hermite*, *Argyris* and choosing a suitable polynomial degree for interpolation. Finally, as regards the step size for the time evolution of the numerical solutions, the time-dependent solver leans on *Runge-Kutta*, *Generalized Alpha* and *Backwards Differentiation Formula (BDF) methods*.





# Chapter 2

## Mathematical modeling of EMT-MET<sup>1</sup>

### 2.1 Introduction

*Epithelial-to-Mesenchymal Transition* (EMT) and its reverse process *Mesenchymal-to-Epithelial Transition* (MET) are crucial steps during tissues and organs remodeling, a phenomenon at the basis of what is generally called *morphogenesis*. Epithelial and mesenchymal cells exhibit different phenotypes, the former being characterized by tight junctions and cohesion, while the latter being more scattered and with a high degree of motility [95, 104]. As such, their emergences are also recognized as critical events which enable/forbid cancer cells in acquiring/losing malignant features.

Altogether, EMT and MET display dynamical behaviours which resemble those observed in physical systems during abrupt macroscopic changes between qualitatively separated stable states, also known as *phase transitions* [20]. A characteristic element to be taken into consideration is that even gradual variation in a few control parameters and unknowns density can switch cells into specific and distinct phenotypes.

The description of the interplay between the two phenotypes, namely epithelial and mesenchymal, has been largely explored using various strategies and tools (see [63, 103] and references therein). The most traditional approach is based on a bottom-up procedure, supposed to be paramount for describing how global structures are the result of underlying microscopic counterparts. However, in the last decades, such point of view has been widely disputed, leaving the space to

---

<sup>1</sup>The contents are collected in [57]; a further manuscript concerning the topics of the chapter is in preparation for the special issue ‘*Where are the biological sciences going?*’, *Organisms. Journal of Biological Sciences*.

different approaches based on special types of modeling programmes [9]. Indeed, it has been proposed that critical events are the result of emerging properties at a scale that is larger than the microscopic ones, according to the influence of external constraints. Therefore, a different approach should be applied, based on what it is now a well-established discipline, following the *Systems Biology* perspective [92]. More specifically, instead of focusing on the role of individual genes, proteins or other local pathways in biological phenomena, its aim is to characterize the ways molecular parts adopt for interacting with each other to determine the collective dynamics of the system as a whole. Recently, the Systems Biology approach has been successfully extended to the field of oncology, with the ambitious idea of grasping complexity in the genesis of cancer [12].

We propose a simplified mathematical model which is, in principle, capable to catch the basic qualitative behaviour of EMT and MET, in an uncomplicated setting. We stress that the presence of a (single) nonlinear term is crucial, since it guarantees the existence of propagating fronts through the emergence of several stationary states. Incidentally, we observe that the same kind of mechanism can be considered for the description of *wound healing* experiments [7].

Entering the heart of the matter, we focus here on a diffusive variation of the ODE model originally proposed in [92] which, after an appropriate adimensionalisation, reads as

$$\begin{cases} \tau \partial_t u = v - u \\ \partial_t v = \Delta_{\mathbf{x}} v - v + \lambda g(u) \end{cases} \quad \text{for } \mathbf{x} \in \mathbb{R}^d, \quad t > 0, \quad (2.1)$$

with some positive parameters  $\tau, \lambda$  and a saturating-type reaction function  $g$ , which is typically assumed to be S-shaped: concrete examples are provided by

$$g(u) = \frac{u^p}{1 + u^p} = 1 - \frac{1}{1 + u^p}, \quad (2.2)$$

with  $p \geq 2$ . Roughly speaking, the variable  $u$  can be interpreted as the density of cells exhibiting an epithelial phenotype, while the variable  $v$  is the density for the mesenchymal phenotype, its motility described by the presence of the Laplace operator  $\Delta_{\mathbf{x}}$  in the second equation<sup>2</sup>. The main advantage of system (2.1) is to collect into two constants, namely  $\tau$  and  $\lambda$ , the global characteristics of the physical model: the first corresponds to a *relaxation time* and the latter describes *invasiveness* of the tumour cells. On that account, such a model does not claim to provide a quantitative biological description, but only a qualitative one; the main

---

<sup>2</sup>The interpretation of the unknowns provided in [92] is actually different: the variable  $u$  refers to the *E-cadherin boundary values* and  $v$  stands for the *coherency*. Being the latter too vague to be rigorously quantified, here we have opted for an alternative meaning in terms of cells phenotypes, which appear to be experimentally more robust and, ideally, measurable.

point is to show that the invasion process could be, in principle, reversible and that such reversion could be measured by means of a limited number of parameters. A realistic quantitative model would require a more tailored definition of the objects under examination.

This chapter is structured as follows. In Section 2.2, we present the general form of the mathematical model and deduce its corresponding adimensionalisation [92]. After a brief discussion on the basic properties of the underlying kinetic mechanism, that is relative to the description of space-independent solutions, we consider the special case of planar solutions, then concentrating the attention to traveling wave solutions for which an identity for the propagation speed of the front is determined. Section 2.3 addresses the computational analysis of the one-dimensional version of the model, choosing an implicit-explicit finite difference algorithm (the linear terms are discretized implicitly and an explicit approximation is reserved to the nonlinear term). Several numerical simulations are performed by considering the so-called *LeVeque-Yee formula* as a reference for the evaluation of propagation speed. In addition, we perform a sensitivity analysis with respect to the parameters  $\tau$  and  $\lambda$ , collecting the conclusions of the analysis performed.

## 2.2 A simple PDE model for phase transitions

Let  $\Omega$  denote a domain in  $\mathbb{R}^d$  with smooth boundary  $\partial\Omega$ . We consider the initial-boundary value problem for the system of partial differential equations

$$\begin{cases} \tau \partial_t u = \alpha v - \beta u \\ \gamma \partial_t v = \varepsilon^2 \Delta_{\mathbf{x}} v - \mu v + \lambda g(u) \end{cases} \quad \text{for } \mathbf{x} \in \Omega, \quad t > 0, \quad (2.3)$$

with some external parameters  $\tau, \alpha, \beta, \gamma, \varepsilon, \lambda, \mu$  and a structural function  $g$  to be specified later on. This system is determined by the (non-negative) initial conditions

$$u(\mathbf{x}, 0) = u_0(\mathbf{x}), \quad v(\mathbf{x}, 0) = v_0(\mathbf{x}), \quad (2.4)$$

and the zero-flux boundary conditions

$$\nabla_{\mathbf{x}} u \cdot \mathbf{n} \big|_{\partial\Omega} = 0, \quad \nabla_{\mathbf{x}} v \cdot \mathbf{n} \big|_{\partial\Omega} = 0, \quad (2.5)$$

where  $\mathbf{n}$  denotes the exterior normal vector of the boundary  $\partial\Omega$ . We remark that assumption (2.5) is biologically meaningful especially when dealing with *in vitro* experiments settled on a *Petri dish*, for example. However, for the mathematical analysis, the requirement on boundary data for the unknown  $u$  is not needed, because its dynamics is described by an ODE model.

The reaction function  $g$  in (2.3) is assumed to be a transformation of  $[0, +\infty)$  into

itself and, additionally, it satisfies the following hypotheses:

- H1.** it is sufficiently smooth, strictly increasing and such that  $g(0) = 0$ ;
- H2.** it is convex in  $[0, \bar{u}]$  and concave in  $[\bar{u}, +\infty)$  for some  $\bar{u} > 0$ ;
- H3.** it converges toward a given positive (saturating) limit  $g_\infty$  at  $+\infty$ .

### 2.2.1 Adimensionalization

We apply to system (2.3) the rescaling

$$\tilde{u} = \frac{u}{U}, \quad \tilde{v} = \frac{v}{V}, \quad s = \frac{t}{T}, \quad \mathbf{y} = \frac{\mathbf{x}}{X},$$

so that it becomes

$$\begin{cases} \tilde{\tau} \partial_s \tilde{u} = \tilde{v} - \tilde{u} \\ \partial_s \tilde{v} = \Delta_{\mathbf{y}} \tilde{v} - \tilde{v} + \tilde{\lambda} \tilde{g}(\tilde{u}) \end{cases}$$

where

$$V = \frac{\beta U}{\alpha}, \quad T = \frac{\gamma}{\mu}, \quad X = \frac{\varepsilon}{\sqrt{\mu}} \quad \text{and} \quad \tilde{\tau} = \frac{\mu \tau}{\beta \gamma}, \quad \tilde{\lambda} = \frac{\alpha \lambda}{\beta \mu},$$

together with  $\tilde{g}(\tilde{u}) := \frac{1}{U} g(U\tilde{u})$ , and choosing the constant value  $U$  for  $\tilde{g}$  to be equal to 1 at  $+\infty$ , that is

$$U = g_\infty := g(+\infty).$$

Hence, from now on, we study the solutions to the adimensionalized hyperbolic-parabolic system (2.1), where, for the sake of readability, we consider the original variables  $(\mathbf{x}, t)$ , the parameters  $\tau, \lambda$  and unknowns  $(u, v)$ , also assuming  $g(+\infty) = 1$ , with the initial-boundary conditions described in (2.4)-(2.5).

It is worth noticing that first equation in (2.1) can also be rewritten as a truncated first order Taylor expansion of the delayed expression

$$u(\mathbf{x}, t + \tau) = u(\mathbf{x}, t) + \tau \partial_t u(\mathbf{x}, t) + o(\tau) \approx u(\mathbf{x}, t) + \tau \partial_t u(\mathbf{x}, t).$$

Moreover, system (2.1) is equivalent to the *one-field equation* for the unknown  $u$  given by

$$\tau \partial_{tt} u + (1 + \tau) \partial_t u = \Delta_{\mathbf{x}}(u + \tau \partial_t u) - u + \lambda g(u), \quad (2.6)$$

which is a third order hyperbolic equation for the scalar variable  $u$ . Viceversa, the system (2.1) is also equivalent to an integro-differential parabolic equation for the unknown  $v$  given by

$$\partial_t v = \Delta_{\mathbf{x}} v - v + \lambda g \left( u_0(\mathbf{x}) e^{-t/\tau} + \frac{1}{\tau} \int_0^t e^{-(t-s)/\tau} v(\mathbf{x}, s) ds \right),$$

which is obtained by solving the first equation in (2.1) with respect to  $u$  and then coupling with the second condition for the variable  $v$ .

Incidentally, let us observe that system (2.1) is *positivity preserving*, meaning that if the initial data  $u_0$  and  $v_0$  are non-negative, the same is true for the solutions to the corresponding initial-boundary value problem. Indeed, the two equations of the system, considered separately, are scalar equations; thus, they both satisfy a *comparison principle*: in particular, the solution  $u$  to the linear ODE model

$$\tau \partial_t u + u = F(\mathbf{x}, t) \geq 0, \quad u(\mathbf{x}, 0) = u_0(\mathbf{x}) \geq 0,$$

is non-negative, and similarly the solution  $v$  to the linear parabolic operator

$$\partial_t v - \Delta_{\mathbf{x}} v + v = G(\mathbf{x}, t) \geq 0, \quad v(\mathbf{x}, 0) = v_0(\mathbf{x}) \geq 0,$$

is non-negative (with both conditions being satisfied by the model under analysis).

### 2.2.2 Space independent solutions

To start with, let us consider space independent solutions, so that system (2.1) reduces to

$$\tau \frac{du}{dt} = v - u, \quad \frac{dv}{dt} = -v + \lambda g(u), \quad (2.7)$$

which coincides with the ODE model originally proposed in [92]. Analogous models are already present in the literature since decades: among others, we quote [38] and its descendants, where the *FitzHugh-Nagumo system* is proposed in the context of axon signalling, with variables  $u$  and  $v$  describing approximately the potential of the nerve axons and a (qualitative) feature of the ionic channels opening/closure mechanism, respectively. Of course, the action of the variable  $u$  inside the equation for  $v$  is completely different with respect to the model presented in this work: indeed, we attempt at simulating a different type of cellular mechanism, characterized by a *cooperative-type coupling*, for which each variable positively contributes to the increase of the other. Finally, in [44] a similar system based on the *mass action law* is considered in the context of *wound healing* experiments [7], with the variables  $u$  and  $v$  describing, respectively, the area of dead tissue and the spatially-evolving section of the wound.

The main interest in the model presented in this work is the form of the reaction function  $g$ , as in (2.2), which is supposed to have a *saturating Hill shape*. Ideally, such a formula can be recovered by applying some variation of the *Michaelis-Menten reduction* from a more involved enzyme-type model (see [36, 64, 99], for instance) and this kind of shape is sometimes also referred to as the *Langmuir adsorption model* function [59]. Numerical simulations will be provided in Section 2.3.3 for the special case  $p = 2$ , for which the modeling function  $g$  is said to have a *Holling type III response* form [43].

Next, we concentrate on the steady states of the ODE system (2.7), which are also steady stationary states of the original PDE system (2.1). Time independent solutions are couple of real numbers such that  $v - u = 0$  and  $v - \lambda g(u) = 0$ , hence they correspond to values  $\bar{u}$  such that

$$h(\bar{u}; \lambda) := \bar{u} - \lambda g(\bar{u}) = 0. \quad (2.8)$$

Under the additional assumptions on the alternating convexity/concavity of  $g$  introduced above (see **H1**, **H2** and **H3** at the beginning of Section 2.2), it is possible to distinguish three different configurations depending on the value taken by the external parameter  $\lambda$  (refer to Figure 2.1).

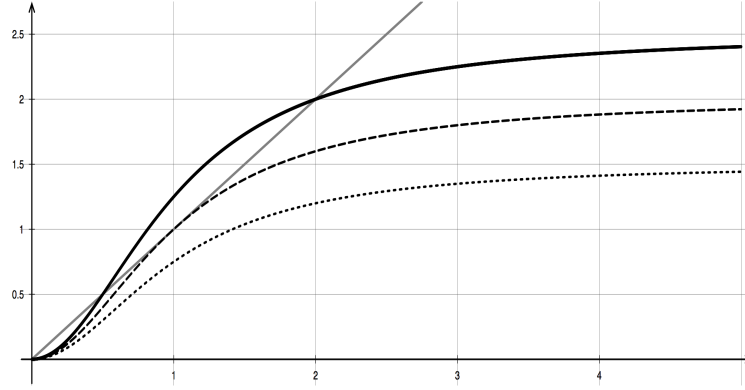


Figure 2.1. Graphs of the straight line  $v = u$  (continuous, gray) and the reaction function  $v = \lambda g(u)$ , with  $g(u) = \frac{u^2}{1 + u^2}$ , for  $\lambda = 1.5$  (dotted),  $\lambda = 2.0$  (dashed) and  $\lambda = 2.5$  (continuous).

Specifically, there is a (strictly) positive threshold value  $\lambda_* > 0$ , such that:

1. for  $\lambda < \lambda_*$ , the point  $(0, 0)$  is the unique intersection of the straight line  $v = u$  with the curve  $v = \lambda g(u)$ , which corresponds to a stable equilibrium for the underlying ODE system;
2. for  $\lambda = \lambda_*$ , there are two intersections with abscissae  $u = 0$  and  $u = u_* > 0$  (unstable state);
3. for  $\lambda > \lambda_*$ , there are three intersections for  $u = 0$ ,  $u = u_-$  and  $u = u_+$  such that  $0 < u_- < u_+$ , with the extremal values which correspond to stable equilibria and the intermediate one that is unstable for the underlying ODE system.

The threshold  $\lambda_*$ , which separates the two limiting regimes, is given by the unique value such that

$$h(u_*; \lambda_*) = u_* - \lambda_* g(u_*) = 0 \quad \text{and} \quad \frac{dh}{du}(u_*; \lambda_*) = 1 - \lambda_* \frac{dg}{du}(u_*) = 0,$$

for some  $u_\star > 0$ . Hence, it holds  $\lambda_\star = \frac{u_\star}{g(u_\star)}$  and  $\frac{1}{\lambda_\star} = \frac{dg}{du}(u_\star)$ , so that finally we obtain the pointwise identity

$$u_\star \frac{dg}{du}(u_\star) = g(u_\star).$$

**Example 2.2.1.** We consider an example of reaction function (2.2) with  $p = 2$ . For this case, the intersection values  $\bar{u}$  in (2.8) are explicitly computable: upon substitution, for  $\lambda \geq 2$ , we infer that  $h(\bar{u}; \lambda) = 0$  if and only if  $\bar{u}(\bar{u}^2 - \lambda\bar{u} + 1) = 0$ , that is  $\bar{u} \in \{0, u_-(\lambda), u_+(\lambda)\}$  with

$$u_\pm(\lambda) = \frac{1}{2} \left( \lambda \pm \sqrt{\lambda^2 - 4} \right).$$

For  $0 < \lambda < 2$ ,  $h(\bar{u}; \lambda) = 0$  for physically admissible solutions if and only if  $\bar{u} = 0$ . In particular, the threshold value is  $\lambda_\star = 2.0$ , corresponding to the abscissa  $u_\star = 1$  (refer to Figure 2.2). As for the general case, the value  $u_+(\lambda)$  is monotone increasing with respect to the invasiveness parameter  $\lambda$ , and it holds

$$u_+(\lambda) = \lambda + o(1) \quad \text{as } \lambda \rightarrow +\infty.$$

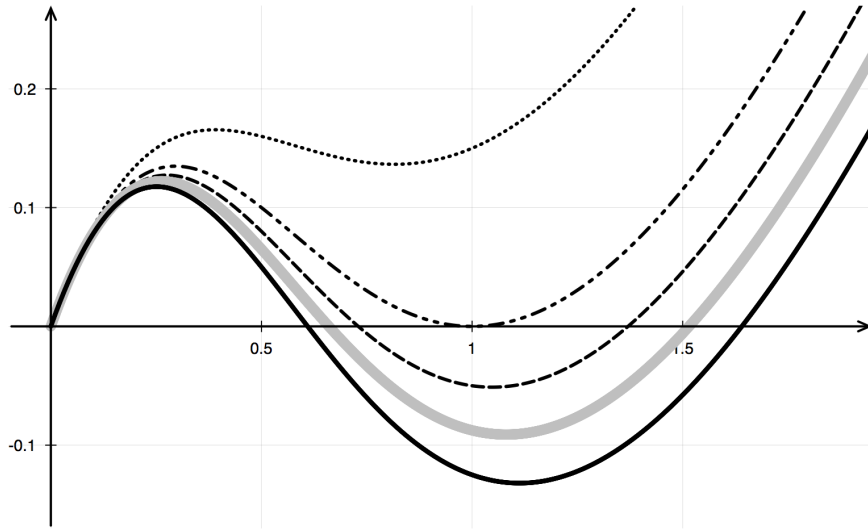


Figure 2.2. Graphs of the function  $h(u; \lambda) = u - \lambda g(u)$ , with  $g(u) = \frac{u^2}{1 + u^2}$ , for  $\lambda = 1.7$  (dotted),  $\lambda = \lambda_\star = 2.0$  (dot-dashed),  $\lambda = 2.1$  (dashed),  $\lambda = \lambda_0 = 2.175063$  (continuous, gray) and  $\lambda = 2.25$  (continuous).

### 2.2.3 Stability of steady states

We start by dealing with the limiting regime  $\tau = 0$  in system (2.7). Denoting by  $H(\cdot; \lambda)$  the primitive with respect to the first argument of the function  $h(\cdot; \lambda)$  and by  $G$  the primitive of  $g$ , we deduce that

$$H(v; \lambda) = \int_0^v [u - \lambda g(u)] du = \frac{1}{2} v^2 - \lambda G(v), \quad (2.9)$$

which is called the *potential* of the function  $h$  defined in (2.8), because the dynamical system (2.7) with  $\tau = 0$  is equivalent to the scalar equation (ODE in gradient formulation)

$$\frac{dv}{dt} = -\partial_v H(v; \lambda). \quad (2.10)$$

Note that there exists a unique positive  $\lambda_0$  and its corresponding  $u_0 := u_+(\lambda_0)$  such that the two wells of the potential  $H$  have the same depth (refer to Figure 2.3). For the prototype reaction function (2.2) with  $p = 2$ , the values  $\lambda_0$  and  $u_0$  are explicitly computable by applying the *iterative Newton method*, so that

$$u_0 \approx 1.5149946 \quad \text{and} \quad \lambda_0 \approx 2.175063 > \lambda_\star = 2.0.$$

Such configuration is particularly relevant, as it will be further discussed later on.

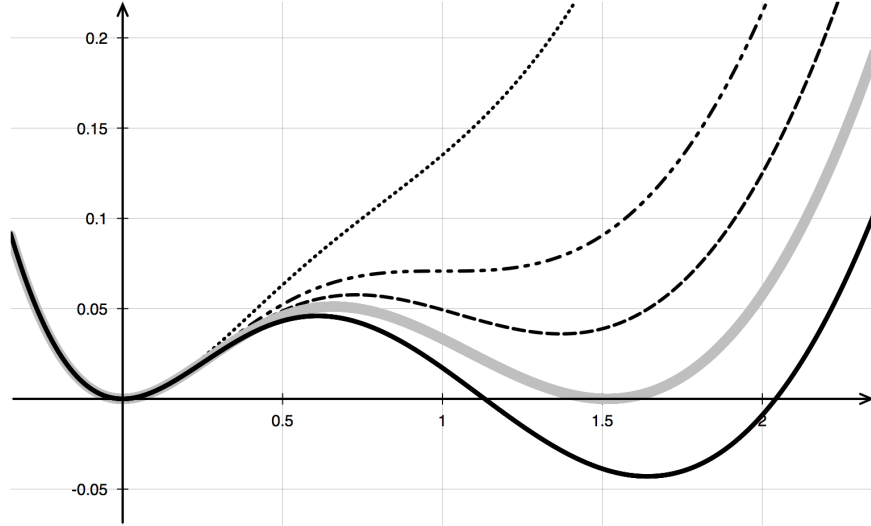


Figure 2.3. Graphs of the potential  $H(u; \lambda)$  associated with  $g(u) = \frac{u^2}{1+u^2}$  for  $\lambda = 1.7$  (dotted),  $\lambda = \lambda_\star = 2.0$  (dot-dashed),  $\lambda = 2.1$  (dashed),  $\lambda = \lambda_0 = 2.175063$  (continuous, gray) and  $\lambda = 2.25$  (continuous).



For  $\tau = 0$ , the stability of the equilibria for equation (2.10) is readily checked, being determined by the sign of the derivative of the function  $h(\cdot; \lambda)$  in (2.8) with respect to the first argument: when this derivative is positive, the equilibrium is stable, and when negative, the equilibrium is unstable.

For  $\tau > 0$ , the situation is only slightly more complicated. Indeed, the linearization of equation (2.6) for space independent solutions at some equilibrium  $\tilde{u}$  reads

$$\tau \frac{d^2 u}{dt^2} + (1 + \tau) \frac{du}{dt} + \partial_u h(\tilde{u}; \lambda) u = 0$$

and the corresponding *characteristic values* are

$$\mu_{\pm}(\tau) = \frac{1}{2\tau} \left[ -(1 + \tau) \pm \sqrt{(1 - \tau)^2 + 4\tau \lambda \frac{dg}{du}} \right].$$

In particular, it is readily checked that  $\mu_-$  is always strictly negative (with order  $1/\tau$ ) and  $\mu_+$  is negative (with order 1) if and only if

$$\partial_u h(\tilde{u}; \lambda) = 1 - \lambda \frac{dg}{du}(\tilde{u}) > 0,$$

matching completely the limiting regime  $\tau \rightarrow 0^+$ .

### 2.2.4 Planar solutions

Next, let us consider special solutions possessing planar symmetry – labelled as the original unknowns with an abuse of notation – given by  $u(\mathbf{k} \cdot \mathbf{x}, t)$  and  $v(\mathbf{k} \cdot \mathbf{x}, t)$ , for some vector  $\mathbf{k} \in \mathbb{R}^d$  with unit norm. Substituting this assumption in system (2.1), we infer the one-dimensional PDE model

$$\begin{cases} \tau \partial_t u = v - u \\ \partial_t v = \partial_{xx} v - v + \lambda g(u) \end{cases} \quad (2.11)$$

with the zero-flux boundary conditions (2.5) reducing to

$$\partial_x v(a, t) = \partial_x v(b, t) = 0 \quad \text{for } \Omega = (a, b). \quad (2.12)$$

In the case  $\Omega = \mathbb{R}$ , system (2.11) is expected to possess special solutions consisting in a rigid motion with some velocity  $c$  of a fixed configuration  $(U, V)$ , according to the following definition.

**Definition 2.2.1.** *A solution  $(u, v)$  of the special form  $(u, v)(x, t) = (U, V)(\xi)$ , with  $\xi := x - ct$  and asymptotic states  $(U, V)(\pm\infty) = (U_{\pm}, V_{\pm})$  with  $(U_-, V_-) \neq (U_+, V_+)$  is called a propagating front.*

*The function  $(U, V)$  is the profile of the front and  $c$  is its speed.*

The ODE model for traveling wave solutions deduced from (2.11) reads

$$c\tau \frac{dU}{d\xi} + V - U = 0, \quad \frac{d^2V}{d\xi^2} + c \frac{dV}{d\xi} - V + \lambda g(U) = 0. \quad (2.13)$$

In particular, being the system (2.13) autonomous, the profiles  $(U, V)$  – whenever they exist – are determined up to translations in the variable  $\xi$  (the so-called *translational invariance* of traveling fronts). Moreover, it is customarily assumed that  $\frac{dV}{d\xi} \rightarrow 0$  as  $\xi \rightarrow \pm\infty$ , because that is actually the case for solutions with (constant) asymptotic states.

### 2.2.5 An identity for the wave speed

For  $\tau = 0$ , the existence and stability of a *heteroclinic orbit* connecting the two stable states is a well known result (see [27] and references therein). Moreover, the corresponding speed is uniquely determined by the location of the asymptotic states. In such a singular limiting regime, the model (2.11) reduces to a "fake" two-dimensional system, being actually equivalent to the scalar reaction-diffusion equation  $\partial_t v = \partial_{xx} v - \partial_v H(v; \lambda)$ , where  $H(\cdot; \lambda)$  is given in (2.9). Whenever the potential  $H$  exhibits two wells, which is the case if and only if  $\lambda > \lambda_*$  (refer to Figure 2.3), it can be shown that there exists a propagating front connecting the two minima of  $H$ , thus corresponding to the extremal zeros of  $h$ , with speed that is linked to the difference of depth of the wells. Indeed, for  $\tau = 0$ , multiplying the reduced ODE for traveling waves (2.13) by  $\frac{dV}{d\xi}$  and integrating over  $\mathbb{R}$ , we infer the identity

$$c(0, \lambda) = \frac{H(V_+; \lambda) - H(V_-; \lambda)}{\int_{-\infty}^{+\infty} (dV/d\xi)^2 d\xi} = \frac{H(u_+; \lambda)}{\int_{-\infty}^{+\infty} (dV/d\xi)^2 d\xi} \quad \text{for all } \lambda \geq \lambda_*, \quad (2.14)$$

where  $V_{\pm} = V(\pm\infty)$  indicate the asymptotic states, with  $V_- = 0$  and  $V_+ = u_+$ , since  $H(0; \lambda) = 0$ .

For  $\tau > 0$ , we can mimic the same procedure obtaining a generalization of the above identity.

**Proposition 2.2.1.** *Assume that  $\tau > 0$  is chosen so that system (2.11) supports traveling wave solutions connecting  $(0, 0)$  with  $(u_+(\lambda), u_+(\lambda))$ . Then, the speed of propagation  $c(\tau, \lambda)$  satisfies the identity*

$$c(\tau, \lambda) = \frac{H(u_+; \lambda)}{\int_{-\infty}^{+\infty} \left[ \tau \lambda \frac{dg}{du} (dU/d\xi)^2 + (dV/d\xi)^2 \right] d\xi}. \quad (2.15)$$

*Proof.* Multiplying the first equation of system (2.13) by  $\lambda \frac{dg}{d\xi}$  and the second by  $\frac{dV}{d\xi}$ , we deduce

$$c\tau\lambda \frac{dg}{d\xi} \frac{dU}{d\xi} + \lambda \frac{dg}{d\xi} V - \lambda \frac{dg}{d\xi} U = 0, \quad \frac{d^2V}{d\xi^2} \frac{dV}{d\xi} + c \left( \frac{dV}{d\xi} \right)^2 - V \frac{dV}{d\xi} + \lambda g \frac{dV}{d\xi} = 0,$$

which can be rewritten as

$$c\tau\lambda \frac{dg}{du} \left( \frac{dU}{d\xi} \right)^2 + \lambda \frac{dg}{d\xi} V - \lambda \frac{dg}{du} U \frac{dU}{d\xi} = 0$$

and

$$c \left( \frac{dV}{d\xi} \right)^2 + \frac{d}{d\xi} \left[ \frac{1}{2} \left( \frac{dV}{d\xi} \right)^2 - \frac{1}{2} V^2 \right] + \lambda g \frac{dV}{d\xi} = 0.$$

Then, summing up these two equations and recalling that  $G$  is a primitive of  $g$ , we conclude that

$$\begin{aligned} & c \left[ \tau\lambda \frac{dg}{du} \left( \frac{dU}{d\xi} \right)^2 + \left( \frac{dV}{d\xi} \right)^2 \right] \\ & + \frac{d}{d\xi} \left[ \frac{1}{2} \left( \frac{dV}{d\xi} \right)^2 - \frac{1}{2} V^2 + \lambda G(U) + \lambda(V - U)g(U) \right] = 0, \end{aligned}$$

since a straightforward application of the integration by parts formula provides

$$\int u \frac{dg}{du} du = u g(u) - \int g(u) du = u g(u) - G(u) + \text{constant}.$$

Finally, integrating with respect to  $\xi \in \mathbb{R}$ , under the assumption that  $\frac{dV}{d\xi} \rightarrow 0$  as  $\xi \rightarrow \pm\infty$ , we obtain the equality (2.15) for  $U_- = V_- = 0$  and  $U_+ = V_+ = u_+$  because  $H(0; \lambda) = 0$  from its definition (2.9).  $\square$

It is worth comparing the general identity (2.15) with its reduced version (2.14). Moreover, we stress the fact that identity (2.15) cannot be regarded as an equality, since the right-hand side of the formula depends on the derivatives of the front profile, which in turn depends on the velocity itself.

There exists a critical value  $\lambda_0$ , strictly greater than  $\lambda_*$ , such that system (2.11) possesses a special traveling wave which is actually a stationary solution  $(U, V) =$

$(U(x), V(x))$  with null velocity. Such value separates positive and negative speeds of propagation, and it is determined by the requirements

$$h(u_0; \lambda_0) = u_0 - \lambda_0 g(u_0) = 0 \quad \text{and} \quad H(u_0; \lambda_0) = \frac{1}{2} u_0^2 - \lambda_0 G(u_0) = 0.$$

The first condition above translates the fact that  $u_0$  is a zero of the function  $h(u; \lambda)$ , hence a singular point of the potential  $H(u; \lambda)$ , and consequently a candidate for the asymptotic state  $u_+$  in Proposition 2.2.1.

The second one corresponds to the requisite that the two wells of  $H$  have same depth (refer to Figure 2.3) and implies that  $c(\tau, \lambda_0) = 0$  from identity (2.15). Specifically, the values  $u_0 \neq 0$  and  $\lambda_0$  are such that

$$G(u_0) - \frac{1}{2} u_0 g(u_0) = 0 \quad \text{and} \quad \lambda_0 = \frac{u_0}{g(u_0)}.$$

In this framework, one can compute the stationary traveling front  $(U, V)$  by using the standard construction of a steady heteroclinic orbit for the double-well potential with wells of equal depth [27].

We conclude this section by recalling that an analytical proof of the existence of propagating fronts for the system (2.11) is still an open problem, in the general case  $\lambda > \lambda_*$ , and currently under investigation.

A reasonable conjecture states that, given any couple of parameters  $\tau, \lambda$  with  $\tau > 0$  and  $\lambda > \lambda_*$ , there is a unique propagation speed  $c(\tau, \lambda)$  for the possible profile connecting the two stable steady states  $(0, 0)$  (on the left) and  $(u_+, u_+)$  (on the right).

For the limiting case  $\lambda = \lambda_*$ , the behaviour is well-described by the *Zeldovich equation* (more details are provided at the end of Section 2.3.3). Therefore, we expect that a variation of the results presented in [91] should hold, suggesting the presence of a single heteroclinic profile with a given critical (strictly positive) speed  $c_*$ , which is exponential decreasing to 0, together with a family of algebraically decaying profiles with speeds  $c > c_*$ .

## 2.3 Numerical experiments

In this section, we perform simulations of system (2.11)-(2.12) to reproduce the special type of planar solutions to system (2.1) described in Section 2.2.4, and we discuss extensively the numerical results.

As regards the numerical strategy, we have tested different approaches and finally decided to employ an implicit-explicit finite difference algorithm. Such a choice allows adopting less expensive time steps compared to fully explicit schemes,

which are instead heavily conditioned by the restrictions that stability requires. On the other hand, it avoids further computational efforts needed in the case of a fully implicit scheme, specifically dealing with large algebraic systems arising from the discretization of the non linear term inside the second equation. As a matter of fact, our numerical algorithm discretizes implicitly all the linear terms, so only an implicit treatment of the reaction function  $g$  is considered. We observe that this technique does not prevent the results from keeping their quantitative and qualitative accuracy.

### 2.3.1 Discretization algorithm

We firstly consider a spatial discretization, leading to a semi-discrete version of system (2.11). Denoting by  $dx$  the spatial mesh size, and employing a standard numerical treatment for the Laplacian, we get

$$\begin{cases} \tau \frac{du_j}{dt} = v_j - u_j \\ \frac{dv_j}{dt} = \frac{v_{j+1} - 2v_j + v_{j-1}}{dx^2} - v_j + \lambda g(u_j) \end{cases}$$

where  $u_j$  and  $v_j$  are synthetic notations for the pointwise approximation of  $u(jdx, t)$  and  $v(jdx, t)$ ,  $j \in \mathbb{Z}$ , in which time dependence is continuous.

Afterwards, we introduce a semi-implicit time discretization with time step  $dt$ , by assuming that  $u(jdx, ndt)$  and  $v(jdx, ndt)$ , together with their approximations  $u_j^n$  and  $v_j^n$ ,  $n \in \mathbb{N}^+$ , are evaluated at discrete spatio-temporal points. Therefore, the fully discrete scheme becomes

$$\begin{cases} \tau \frac{u_j^{n+1} - u_j^n}{dt} = v_j^{n+1} - u_j^{n+1} \\ \frac{v_j^{n+1} - v_j^n}{dt} = \frac{v_{j+1}^{n+1} - 2v_j^{n+1} + v_{j-1}^{n+1}}{dx^2} - v_j^{n+1} + \lambda g(u_j^n) \end{cases} \quad (2.16)$$

with suitable initial and boundary conditions. By means of consistency and stability arguments, it is possible to prove that the numerical method introduced above is convergent: specifically, that strategy turns out to be first order accurate in time and second order in space (see [78], for instance).

After some algebraic manipulations, we deduce a matrix equation for (2.16) as follows,

$$\begin{pmatrix} (1 + \tau^{-1} dt)\mathbf{I} & -\tau^{-1} dt \mathbf{I} \\ \mathbf{O} & (1 + dt)\mathbf{I} + \frac{dt}{dx^2} \mathbf{D} \end{pmatrix} \begin{pmatrix} u^{n+1} \\ v^{n+1} \end{pmatrix} = \begin{pmatrix} u^n \\ v^n + \lambda g(u^n) dt \end{pmatrix}, \quad (2.17)$$

where  $\mathbf{I}$  and  $\mathbf{O}$  denote, respectively, the identity and the null matrix, and  $\mathbf{D} = (-\delta_{i+1,j} + 2\delta_{i,j} - \delta_{i,j+1})$  is the standard discrete Laplacian, with  $\delta_{i,j}$  the *Kronecker delta* function of discrete variables  $i$  and  $j$ .

By taking advantage of the block-matrix structure in (2.17), we notice that a matrix equation for  $v^{n+1}$  can be defined and separately solved, due to the low blocks independence from  $u^{n+1}$ . Indeed, by imposing  $\mathbf{A} := (1 + dt)\mathbf{I} + \frac{dt}{dx^2}\mathbf{D}$ , we solve the tridiagonal linear system  $\mathbf{A}v^{n+1} = v^n + \lambda g(u^n) dt$  and, then, we use the function  $v^{n+1}$  to update  $u^{n+1}$  from the upper blocks. Such backward substitution technique avoids to operate on the whole matrix equation (2.17), thus allowing to save computational time.

For the experimental simulations, in order to collect information about the numerical error produced by the scheme (2.16), we detect a sample solution of system (2.11) which would play the role of an "exact" solution, by considering an extremely fine spatio-temporal mesh (precisely, we take  $dt = 5.0 \times 10^{-3}$  and  $dx = 1.25 \times 10^{-2}$ ). It is important to point out how the structure of matrix  $\mathbf{A}$  lends itself well to invoke the *Thomas algorithm* [78], which is a method of linear complexity with respect to the problem size. Actually, as it is possible to recognize by checking the results in Table 2.1, the computational time increases almost linearly with the size of matrix  $\mathbf{A}$  (for example, by halving the mesh size, namely doubling up the matrix size, the corresponding computational time also approximately doubles up).

All numerical tests are carried out by fixing  $dt = 5.0 \times 10^{-2}$  and  $dx = 1.0 \times 10^{-1}$ , which satisfy the so-called *parabolic CFL condition* [78], and the numerical solutions are compared to the sample solution by means of  $L^\infty$ - and  $L^2$ -norm error analysis (refer to Table 2.1 where these values are highlighted in bold).

### 2.3.2 Numerical evaluation of the propagation speed

In order to provide a numerical approximation of the propagation speed, we refer to the approach originally proposed in [52], and already successfully applied to reaction-diffusion systems in [51, 70].

Let us provide a brief recasting of the basic idea behind such method: given a differentiable function  $\phi$  with asymptotic states  $\phi_\pm = \phi(\pm\infty)$ , the following identity holds

$$\int_{\mathbb{R}} [\phi(x+h) - \phi(x)] dx = h \int_{\mathbb{R}} \int_0^1 \frac{d\phi}{dx}(x+\theta h) d\theta dx = h \int_0^1 \int_{\mathbb{R}} \frac{d\phi}{d\eta}(\eta) d\eta d\theta = h [\phi],$$

for some  $h \in \mathbb{R}$ , where  $[\phi] := \phi_+ - \phi_-$ , which is obtained by simply interchanging the order of integration. In particular, for an increment  $h$  equal to  $-c dt$ , the above

Table 2.1: Error estimates at final time  $T = 100$  for three different temporal mesh sizes  $\text{dt} = 2.5 \times 10^{-2}$  (first table),  $5.0 \times 10^{-2}$  (second table) and  $1.0 \times 10^{-1}$  (third table).

dx	$L^\infty$ -error	$L^2$ -error	CPU time
$2.5 \times 10^{-2}$	$1.56 \times 10^{-2}$	$6.1 \times 10^{-3}$	230.63
$5.0 \times 10^{-2}$	$1.82 \times 10^{-2}$	$7.1 \times 10^{-3}$	190.20
$1.0 \times 10^{-1}$	$2.34 \times 10^{-2}$	$9.2 \times 10^{-3}$	53.69
$2.0 \times 10^{-1}$	$3.42 \times 10^{-2}$	$1.34 \times 10^{-2}$	26.61
$4.0 \times 10^{-1}$	$5.72 \times 10^{-2}$	$2.23 \times 10^{-2}$	10.61

dx	$L^\infty$ -error	$L^2$ -error	CPU time
$2.5 \times 10^{-2}$	$3.31 \times 10^{-2}$	$1.30 \times 10^{-2}$	118.95
$5.0 \times 10^{-2}$	$3.57 \times 10^{-2}$	$1.39 \times 10^{-2}$	56.70
<b><math>1.0 \times 10^{-1}</math></b>	<b><math>4.09 \times 10^{-2}</math></b>	<b><math>1.59 \times 10^{-2}</math></b>	<b>27.92</b>
$2.0 \times 10^{-1}$	$5.16 \times 10^{-2}$	$2.02 \times 10^{-2}$	13.92
$4.0 \times 10^{-1}$	$7.47 \times 10^{-2}$	$2.91 \times 10^{-2}$	5.61

dx	$L^\infty$ -error	$L^2$ -error	CPU time
$2.5 \times 10^{-2}$	$6.67 \times 10^{-2}$	$2.60 \times 10^{-2}$	57.53
$5.0 \times 10^{-2}$	$6.93 \times 10^{-2}$	$2.70 \times 10^{-2}$	27.63
$1.0 \times 10^{-1}$	$7.45 \times 10^{-2}$	$2.91 \times 10^{-2}$	13.88
$2.0 \times 10^{-1}$	$8.52 \times 10^{-2}$	$3.32 \times 10^{-2}$	6.91
$4.0 \times 10^{-1}$	$1.08 \times 10^{-1}$	$4.20 \times 10^{-2}$	2.75

identity provides

$$c = \frac{1}{[\phi] \, \text{dt}} \int_{\mathbb{R}} [\phi(x) - \phi(x - ct)] \, dx. \quad (2.18)$$

Assuming that  $\phi_j^{n+1}$  is an approximation – in the sense of a propagating front – of  $\phi(x_j - ct^n)$ , with  $x_j = j \, \text{dx}$  and  $t^n = n \, \text{dt}$ , we numerically compute the integral in (2.18) by means of the *midpoint algorithm* and we deduce the *LeVeque-Yee formula* for the discrete wave speed, namely

$$c_{LY}^n := \frac{\sum_j (\phi_j^n - \phi_j^{n+1}) \, \text{dx}}{[\phi] \, \text{dt}}. \quad (2.19)$$

Such approximation is indeed exact whenever  $\phi_j^n$  is related to a traveling wave solution  $\phi$  with constant velocity  $c$  and asymptotic states  $\phi_\pm$ . In general, the value  $c_{LY}^n$  in (2.19) can be regarded as a space-averaged propagation speed, which stabilizes to  $c$  when  $\phi_j^n$  converges to the given traveling profile  $\phi$ .

Because system (2.11) has two dynamical variables  $u$  and  $v$ , the respective speed values can be computed through the *LeVeque–Yee formula* (2.19) as

$$c_{u,LV}^n := \frac{\sum_j (u_j^n - u_j^{n+1}) dx}{[u] dt} \quad \text{and} \quad c_{v,LV}^n := \frac{\sum_j (v_j^n - v_j^{n+1}) dx}{[v] dt}, \quad (2.20)$$

thus furnishing two (possibly distinct) values  $c_{u,LV}^n$  and  $c_{v,LV}^n$ .

There are two possible approaches to validate the approximation (2.20) for experimental simulations, either by comparison with a variation of the *Rankine–Hugoniot relation* for reaction-diffusion equations [53], or rather by putting together with the identity (2.15). Note that, in both the last methods, the dynamics of system (2.11) is explicitly taken into account to evaluate the propagation speed; differently, for establishing the formula (2.20), the dynamics of the couple  $(u, v)$  issued from the PDE model is never used. We regard at this property as an irreproachable advantage of the *LeVeque–Yee formula*.

More precisely, we call a variation of the *Rankine–Hugoniot relation* simply the result of a separate integration of the balance laws constituting the one-dimensional system (2.11). Assuming the special type of solutions  $u(x, t) = U(\xi)$  and  $v(x, t) = V(\xi)$ , with  $\xi = x - ct$ , by integrating with respect to  $x$  the first and second equation of system (2.13), we obtain

$$c_{u,RH} = \frac{1}{\tau[u]} \int_{\mathbb{R}} (U - V) dx \quad \text{and} \quad c_{v,RH} = \frac{1}{[v]} \int_{\mathbb{R}} [V - \lambda g(U)] dx,$$

where  $[u] = U_+ - U_-$  and  $[v] = V_+ - V_-$  with the asymptotic states from Definition 2.2.1.

A standard discretization of the above integrals produces

$$c_{u,RH}^n = \frac{\sum_j (u_j^n - v_j^n) dx}{\tau[u]} = \frac{\sum_j (u_j^n - u_j^{n+1}) dx}{[u] dt} = c_{u,LV}^n,$$

where we have used the first equation of (2.16). Analogously, for the second equation it holds

$$c_{v,RH}^n = \frac{\sum_j [v_j^n - \lambda g(u_j^n)] dx}{[v]} = (1 + dt) \frac{\sum_j (v_j^n - v_j^{n+1}) dx}{[v] dt} = (1 + dt) c_{v,LV}^n,$$

thanks to the property of null summation of the discrete Laplacian in (2.16). This computation shows that – apart from a multiplying factor of order  $dt$  – the variation of the *Rankine–Hugoniot relation* and the *LeVeque–Yee formula* are equivalent and, therefore, they cannot be considered as a reliable test for establishing the validity of each other.



On the other hand, comparing the formula (2.20) with the exact identity (2.15) is more favorable, as a consequence of the fact that an independent procedure is required for obtaining a discrete version of (2.15).

Here, we rely on the results provided in Figure 2.4 to support the validity of the *LeVeque-Yee formula* (2.20).

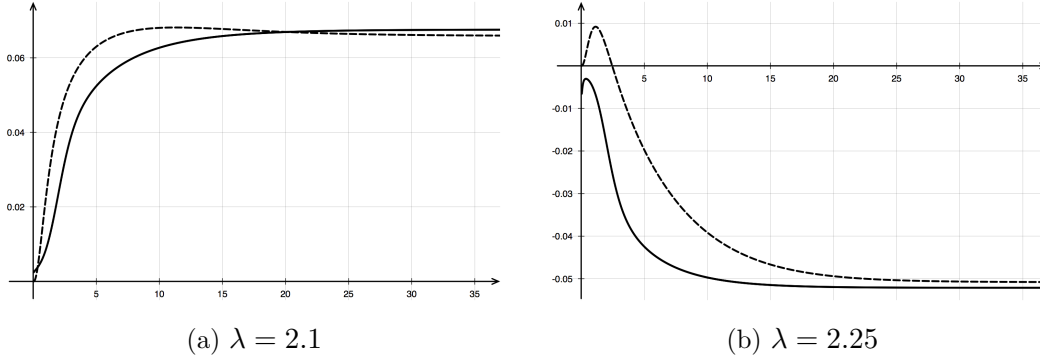


Figure 2.4. Comparison between the function  $t \mapsto c(t)$  for  $t \in (0, 35)$  as given by the exact identity (2.15) (continuous) and the estimation by the *LeVeque-Yee formula* (2.20) (dashed) relative to the values  $\lambda = 2.1$  (a) and  $\lambda = 2.25$  (b).

The errors exhibited in the simulations about the (constant) asymptotic speed values have actually a size of order  $10^{-3}$  and, hence, these numerical results are widely acceptable. Similar experimental errors are also shared by different ranges of the parameter  $\lambda$  and are omitted.

### 2.3.3 Computational results

In the limiting case  $\tau = 0$ , the model (2.11) reduces to a standard parabolic reaction-diffusion equation for the mesenchymal phenotype, whose dynamical behaviour is well-known (see [27] and references therein).

As already discussed in Section 2.2, no invasion is possible for  $0 < \lambda < \lambda_*$  and a complete Mesenchymal-to-Epithelial Transition (MET) represented by the regression to the steady state  $(0, 0)$  is always the final fate of the solution  $(u, v)$ . Then, increasing  $\lambda$  and trespassing the first threshold  $\lambda_*$ , but staying below the second threshold  $\lambda_0$ , translates into the presence of traveling waves with positive speed, thus corresponding again to the case of MET regression. Finally, for choices of  $\lambda > \lambda_0$ , the traveling wave passes from positive to negative values of the speed, corresponding to the case of a possible invasive regime, which is typical of an Epithelial-to-Mesenchymal Transition (EMT).

The general case  $\tau > 0$  follows the same qualitative analysis with respect to the parameter  $\lambda$ .

In particular, for the reaction function (2.2) with  $p = 2$ , the thresholds  $\lambda_\star$  and  $\lambda_0$  can be explicitly computed and are given by

$$0 < \lambda_\star = 2.0 < \lambda_0 = 2.175063.$$

For  $\lambda < \lambda_\star$ , the situation is straightforward, since any positive initial datum generates a solution that converges to  $(0,0)$  as  $t \rightarrow +\infty$  with exponential rate. Then, we concentrate on the regime  $\lambda \geq \lambda_\star$ .

The numerical results reported below describe only the profile for the component  $u$ , the profile of  $v$  being qualitatively very similar. Here, we limit the presentation to the evolution dynamics exhibited by the Riemann problem, but we can guarantee that also much more oscillating initial data show the same kind of large-time behaviour. In addition, we provide different graphical representations of numerical solutions with the same scale in the vertical axis, so that the height and width of the front profiles can be compared between different simulations.

The discussion of the critical case  $\lambda = \lambda_\star = 2.0$  is postponed to the final part of this section.

$\lambda = 2.1 \in (\lambda_\star, \lambda_0)$  – For this choice of the parameter  $\lambda$ , numerical evidence of the existence of a traveling front is obtained. Moreover, being the stable state  $u_+(\lambda)$  closer to the critical state corresponding to the threshold value  $\lambda_\star$ , the solution exhibits a regressive (MET) behaviour, namely the front travels toward the right-hand side with positive speed (refer to Figure 2.5).

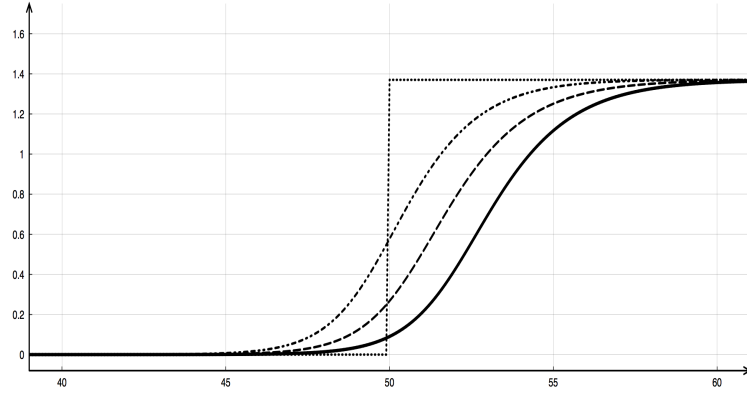


Figure 2.5. Regressive regime (MET) for  $\lambda = 2.1$ . Numerical simulation of the traveling wave solution to the Riemann problem at times  $t = 0$  (dotted),  $t = 10$  (dash-dotted),  $t = 30$  (dashed) and  $t = 50$  (continuous).

$\lambda = \lambda_0 \approx 2.175063$  – Since the two wells of the potential function (2.9) have the same depth for this value of  $\lambda$  (refer to Figure 2.3), system (2.11) possesses a stationary solution with the required asymptotic behaviour for  $\tau = 0$ . In particular, the dynamics is independent from the relaxation parameter  $\tau$  and the existence of a traveling wave in the regime  $\tau > 0$  is a straightforward consequence of the observation that the fronts are actually steady states. For a short time-scale, the solution to the Riemann problem converges to a smoothed version of the jump from  $u = 0$  to  $u = u_+(\lambda_0)$ . Thus, for the sake of shortness, we do not present any numerical simulation for such a simple dynamics.

$\lambda = 2.25 > \lambda_0$  – Again, numerical evidence of the existence of propagating fronts emerges as the long-time behaviour of the solution to the Riemann problem (refer to Figure 2.6). The traveling wave has now a negative speed, so that we are in a situation for which invasion (EMT) is possible, at least for Riemann initial data. For more general initial data, a sort of competition between different parts of the solution starts playing a crucial role in the determination of the large-time behaviour.

As far as  $\lambda$  increases, the numerically computed speed of the propagating front increases in absolute value and, thus, invasive EMT regimes are more and more probable (see Section 2.3.4).

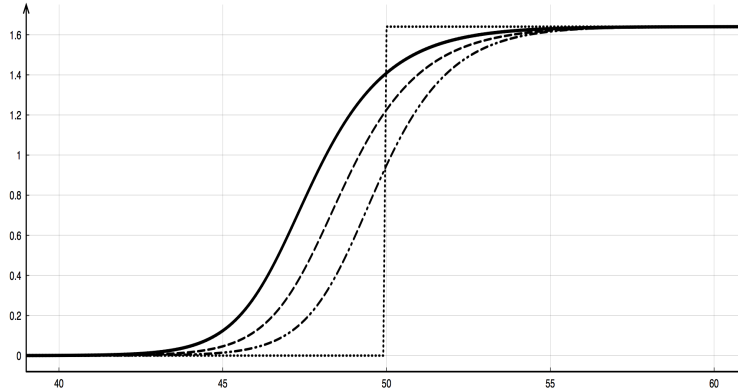


Figure 2.6. Invasive regime (EMT) for  $\lambda = 2.25$ . Numerical simulation of the traveling wave solution to the Riemann problem at times  $t = 0$  (dotted),  $t = 10$  (dash-dotted),  $t = 30$  (dashed) and  $t = 50$  (continuous).

Finally, we come back to the case of the threshold value  $\lambda_*$ .

$\lambda = \lambda_* = 2.0$  – As previously observed, the behaviour of the solutions in this limiting case should be described analogously to what is done in [91] and its descendants for the equation

$$\partial_t u = \partial_{xx} u + u^2(1 - u), \quad (2.21)$$

whose characteristic is the presence of a multiple (second-order) zero at 0. We note that equation (2.21) is sometimes referred to in the literature as the *Zeldovich equation* and it typically arises in the description *combustion phenomena* (see [37], for instance).

In this framework, there exist infinitely many traveling wave solutions (up to translations), with one profile for any given speed greater than or equal to some positive threshold value  $c_*$  (which has an explicit representation exactly when the specific equation (2.21) is considered). The distinguishing feature of the profile  $U_*$  associated to the speed  $c_*$  is that it is the unique profile with an exponential decay to both the asymptotic states. On the contrary, whenever  $c > c_*$ , the decay to the unstable state has merely an algebraic rate. We conjecture the same to be true also for the bi-dimensional system (2.11), although at the moment we are not able to give an analytical proof of such a statement.

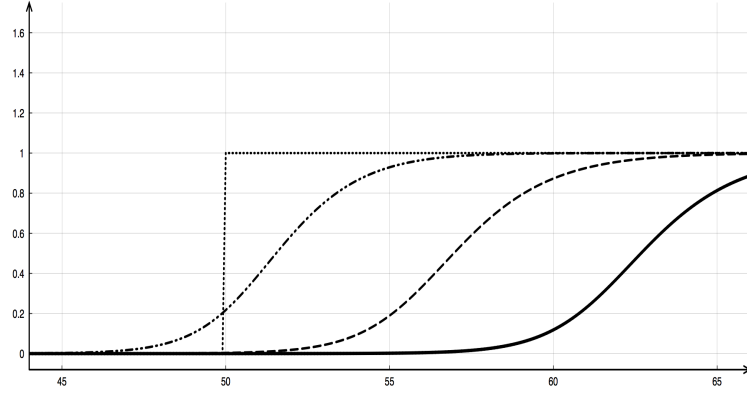


Figure 2.7. Critical regime for  $\lambda = \lambda_* = 2.0$ . Numerical simulation of the traveling wave solution to the Riemann problem at times  $t = 0$  (dotted),  $t = 10$  (dash-dotted),  $t = 30$  (dashed) and  $t = 50$  (continuous).

Here, we limit the presentation to numerical results of the large-time behaviour determined by Riemann initial data, with asymptotic states given by  $(0, 0)$  and  $(u_+(\lambda_*), u_+(\lambda_*))$ . The emergence of a traveling wave solution is apparent, propagating to the right-hand side with some speed  $c_* > 0$  (refer to Figure 2.7).

### 2.3.4 Sensitivity analysis with respect to $\tau$ and $\lambda$

We finally turn our attention to the *sensitivity* of the numerical solutions to system (2.11) with respect to the parameters  $\tau$  and  $\lambda$ , which is measured by considering as principal unknown the speed of propagation of the traveling fronts as evaluated by the *LeVeque-Yee formula* (2.20).

*Relaxation time  $\tau$ .* The dependence from the relaxation parameter  $\tau$  is very smooth and it does not manifest any special feature from a numerical point of view (refer to Figure 2.8).

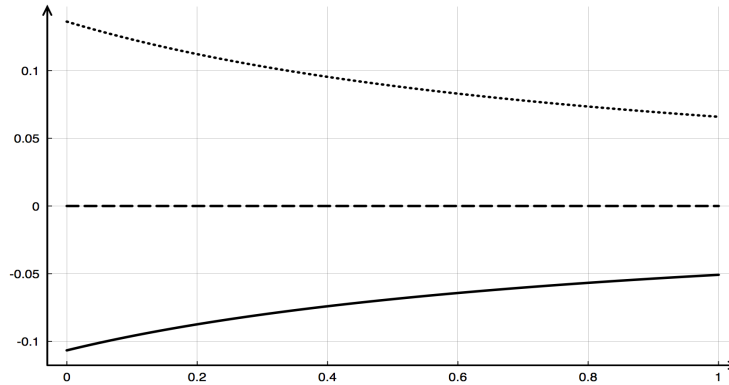


Figure 2.8. Graphs of  $c(\cdot, \lambda)$  as a function of the relaxation parameter  $\tau \in [0, 1]$  for  $\lambda = 2.1$  (dots),  $\lambda = \lambda_0 = 2.175063$  (dashed line) and  $\lambda = 2.25$  (continuous), computed at the final time  $T = 100$ .

Monotonicity of the propagation speed with respect to  $\tau$  can be conjectured as a computational evidence, at least in the range of values under consideration. For  $\tau > 0$  and  $\lambda \in (\lambda_*, \lambda_0)$ , the graph of the function is monotone decreasing, while the monotonicity is reversed in the complementary regime  $\lambda > \lambda_0$ . The two regimes are separated by the threshold value  $\lambda_0 = 2.175063$ , which indeed corresponds to the emergence of a stationary solution. This translates into the fact that both regression (MET) and invasion (EMT) are slowed down when  $\tau$  increases, and that modification is actually relevant, since the regression/invasion speed changes by a percentage greater than 50% when  $\tau$  passes from 0 to 1. Hence, the relaxation time  $\tau$  has a (smoothly) distributed delay-type impact on the dynamics, and this feature has to be taken into account while building more quantitative models.

*Invasiveness parameter  $\lambda$ .* As expected, the dependence from the parameter  $\lambda$  is more interesting, the results exhibiting a strong variation in the vicinity of the threshold value  $\lambda_*$  (refer to Figure 2.9).

As a matter of fact, the function  $c(\tau, \cdot)$  is monotonically decreasing, that reproduces – at least numerically – the experimental observation of propagating fronts expecting to become more and more invasive as  $\lambda$  increases (namely, the preeminent motion is toward the left for our choice of the Riemann data). In particular, the graph of the variation function  $\partial_\lambda c(\tau, \cdot)$  suggests that  $\partial_\lambda c(\tau, \lambda) \rightarrow -\infty$  as  $\lambda \rightarrow \lambda_*$ .

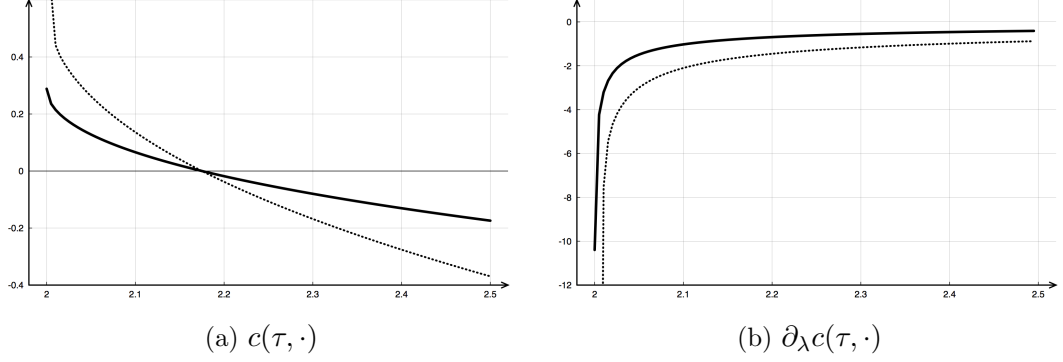


Figure 2.9. Graphs of  $c(\tau, \cdot)$  (a) and its variation  $\partial_\lambda c(\tau, \cdot)$  (b) as functions of the invasiveness parameter  $\lambda \in [2, 2.5]$  for  $\tau = 0$  (dots) and  $\tau = 1$  (continuous), computed at the final time  $T = 100$ .

We conclude this section by recalling that, as a consequence of the convexity/concavity assumptions on the reaction function  $g$ , for any  $\lambda > \lambda_\star$  the system (2.11) possesses two stable steady states  $(0, 0)$  and  $(u_+(\lambda), v_+(\lambda))$ , and therefore it is expected to support a propagating front connecting these asymptotic values (see Section 2.2.3). It is particularly interesting to remark how the simple PDE model (2.11) integrates the typical property of propagating fronts of being/not being invasive merely thanks to the use of two control parameters  $\tau$  and  $\lambda$ . Moreover, we have determined explicit transition thresholds  $\lambda_\star$  and  $\lambda_0$  which separate regression regimes (MET) from invasive ones (EMT), and these parameters are indeed independent from the value of the relaxation time  $\tau$ . Also, in the limiting case  $\tau = 0$ , system (2.11) reduces to a standard scalar reaction-diffusion equation and, thus, a possible strategy for obtaining a complete and rigorous proof of the existence of traveling waves could be based on *singular perturbation* techniques (with respect to the parameter  $\tau$ ).

# Chapter 3

## Study of the Gatenby-Gawlinski model<sup>1</sup>

### 3.1 Introduction

Nowadays, cancer research is one of the most active and interdisciplinary investigation fields. A lot of effort is made in order to improve the actual strategies and get significant results: this is certainly a very challenging point, but it is interesting to notice how, more and more often, new answers are developed changing the point of view the entire research is ruled by and employing approaches whose most appreciable feature is their transverse nature. In this scenario, a remarkable role is played, for instance, by the *Systems Biology* paradigm [2, 61, 62, 92], whose crucial point is the awareness that any complex biomedical problem, such as cancer, must be faced adequately considering the system as a whole, something more than the mere sum of its components, according to an holistic point of view.

This kind of approach is an example among the most interesting strategies that have spread out involving scientists from different fields and the key point, recognizable within all the modern research paths, is the requirement for relying on mathematical modeling. As a matter of fact, applied mathematics is turning out to be a powerful tool for ensuring deeper investigations, especially in the biomedical fields, where suitable models can be developed to support experimental studies. Indeed, although such models are often subject to limitations, the awareness of their indispensability within cancer research is widely spreading, especially for the possibility of both trying and forecasting therapies [31, 35] regardless the mathematical framework complexity, which is not an essential requirement.

The focus of this chapter is the so-called Warburg effect [97, 98] and its mathematical modeling by means of the acid-mediated invasion hypothesis, namely the

---

<sup>1</sup>The contents are mostly collected in [70].

typical strategy of acidity increasing against the environment operated by tumours to regulate their growth, which is already mentioned in [28] and then popularly translated into a system of reaction-diffusion equations [30, 60], whose main feature for mathematical investigation is the existence of traveling waves [10, 11, 26, 32, 33, 34, 35, 93, 94]. Although the Gatenby-Gawlinski model as originally presented in [30, 32] is somehow outmoded, since more sophisticated systems have been introduced to account for improved approximations of realistic biomedical experiments, our interest in that context is exploring the multidimensional framework for which analytical results are neither available nor supportive.

Before starting the investigation, it is worth framing adequately the biomedical context behind the model, specifically describing the hallmarks the *Warburg effect* is characterized by. This phenomenon concerns the metabolism of cancer cells, essentially providing their glucose uptake rates: it has been firstly observed by Otto Warburg [97] in the 1920s, and afterwards confirmed through many experiments, that tumour cells tend to rely on glycolytic metabolism even in presence of huge oxygen amounts. Indeed, from a strictly biomedical point of view, it is important noticing that normal cells undergo glucose metabolism by employing oxidative phosphorylation pathways, which is the most effective process in terms of adenosine triphosphate production and requires oxygen as main resource. Tumour cells behaviour seems to forbear the conventional pathway and appeal instead to glycolysis, inducing lactic acid fermentation, a product generally released in hypoxia regime (see Figure 3.1).

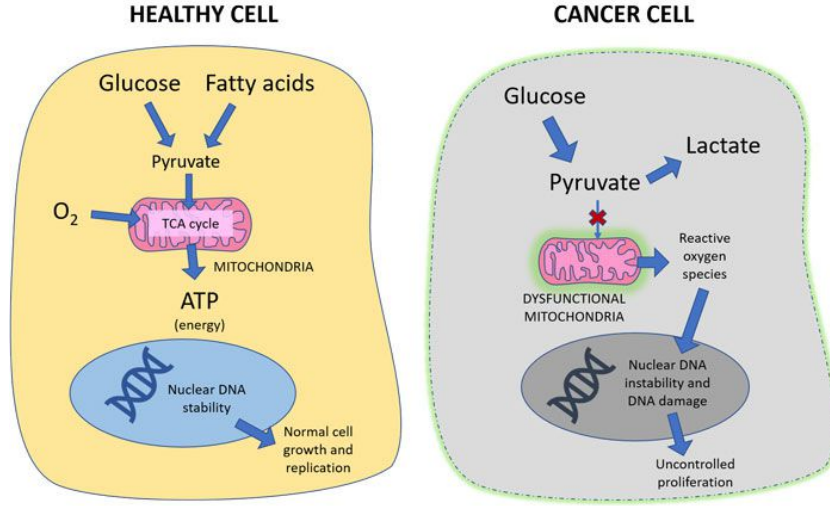


Figure 3.1. Different pathways of healthy and cancer cells metabolism [111].

Although the Warburg effect has been intensely studied by now, how this phenomenon happens and affects cancer proliferation is still an open problem, pro-



ducing discussions about the detection of any possible advantage tumour cells might benefit from. In [89], for instance, a computational model is proposed with the aim of explaining the Warburg effect and its consequences in the tumour microenvironment, deducing the glycolytic property of tumours to proliferate in poorly vascularized tissues avoiding neo-vascularization. The transition between normal to glycolytic metabolism is object of study in [4], through a mathematical model developed to explore the Warburg effect in tumour cords: it is pointed out the capacity of tumours to lean solely on glycolysis. By exploiting a combination of modeling and in vitro experiments, instead, in [18] it is shown how cancer metabolic changes are able to define a microenvironment where the better adapted malignant cells overwhelm the others and spatial structures are created. And in [3], by means of a multiplayer game theory with specific payoff functions, the Warburg effect is approached as a sort of cooperation involving cancer cells, assuming that the public good consists in glycolysis products.

As regards the analysis carried out in this work, the above mentioned *acid-mediated invasion hypothesis* is doubtless the phenomenological key point. The crucial assumption consists in that acidification caused by lactic acid production is globally advantageous for the cancer cells population, whilst defining a toxic microenvironment for healthy cells. On that account, the original modeling based on reaction-diffusion equations developed by Gatenby and Gawlinski [30] is suitable to perform numerical investigations, because it translates the previous qualitative statements to deal with invasive species evolving and modifying within a specific microenvironment belonging to a healthy population. In that context, a novel attempt has been made to extend the analysis to the multidimensional framework, which is not deeply explored yet. Actually, in [79] an investigation of the two-dimensional context is carried out by means of an inverse problem formulation: we have explored the two-dimensional problem as well, and we have reached beyond by considering also some three-dimensional configurations [28].

The contents of the chapter are organized as follows. In Section 3.2, the general form of the model is illustrated along with its adimensionalization, and the main features of the system are considered, without neglecting the corresponding biomedical motivations. Section 3.3 is devoted at building a suitable numerical algorithm, based on a finite volume approximation for the spatial discretization, while a semi-implicit approach is invoked for the time discretization. In Section 3.4, simulations are performed on the ground of the results available in the literature: the wave speed approximation 2.19 is exploited to verify the existence of a stable threshold for the propagating fronts. Section 3.5 concerns with the possibility of assuming simplifying hypotheses in order to build some model reductions, however allowing to preserve important qualitative features. Finally, in Section 3.6, the

multidimensional environment is analyzed by means of a finite element approach, considering both two-dimensional and three-dimensional simulations.

### 3.2 The Gatenby-Gawlinski model

The model, firstly proposed by Gatenby and Gawlinski in [30], is developed in order to reproduce cancer cells invasion within a healthy tissue, starting from a stage in which the carcinogenesis has already happened and, then, it is not further taken into account. The authors instead focus on the interactions between malignant and healthy cells populations occurring at the tumour-host interface, where a significant role is played by the lactic acid production and spreading, because of the transition towards the glycolytic metabolism.

From a mathematical point of view, dealing with a *reaction-diffusion system* is required: the unknown functions are  $U(x, t)$ , which stands for the healthy tissue density, the tumour cells density  $V(x, t)$  and  $W(x, t)$  representing the extracellular lactic acid concentration in excess, so that the systems reads

$$\begin{cases} \frac{\partial U}{\partial t} = \rho_1 U \left(1 - \frac{U}{\kappa_1}\right) - \delta_1 U W \\ \frac{\partial V}{\partial t} = \rho_2 V \left(1 - \frac{V}{\kappa_2}\right) + D_2 \frac{\partial}{\partial x} \left[ \left(1 - \frac{U}{\kappa_1}\right) \frac{\partial V}{\partial x} \right] \\ \frac{\partial W}{\partial t} = \rho_3 V - \delta_3 W + D_3 \frac{\partial^2 W}{\partial x^2} \end{cases} \quad (3.1)$$

with initial and boundary conditions to be introduced later on. For the functions  $U$  and  $V$  a logistic growth is considered, with carrying capacities  $k_1$  and  $k_2$  respectively, while  $\rho_1$  and  $\rho_2$  are the growth rates; instead,  $\delta_1$  is a death rate proportional to  $W$ , this term being involved to reproduce healthy cells degradation due to the interactions with the lactic acid.

The structure of the degenerate diffusion term within the second equation is indeed a very interesting feature of the model (3.1) and its importance for tumour cells density is justifiable by means of biomedical arguments. As a matter of fact, the coefficient  $D_2$  stands for a diffusion constant of the neoplastic tissue when there is a complete lack of healthy tissue. On the other hand, when the local healthy tissue concentration is at its carrying capacity, the diffusion coefficient equals zero and the cancer cells are unable to spread out. As a result, no tumour spreading is allowed unless the surrounding healthy cells concentration is no longer equal to its carrying capacity. This is aimed at simulating a realistic defense mechanism regarding tumour confinement [30, 84]: it is postulated that, for neoplastic tissue, the diffusion rate diminishes in proportion to the healthy tissue concentration,

whilst diffusion is assumed to be negligible for normal tissue (that should be intended as compared to the neoplastic tissue for its mesenchymal phenotype [92]). It is important to notice that, despite its initial originality, the diffusion term pertaining to the tumour cells population inside the Gatenby-Gawlinski model (3.1) is also one of its severe limitations, because experimental observations suggest that it should actually account for the contribution of tumour cells as well; moreover, it is reasonable to define a global density threshold, including healthy and tumour cells, which inhibits not only diffusion but also proliferation of both  $U$  and  $V$  as regulated by their combination or rather competition [29, 42].

Finally, in the third equation, a standard diffusion process with constant  $D_3$  is considered for the spatial spreading of the lactic acid. Moreover, a growth rate  $\rho_3$  is involved for the acid production, which is linearly proportional to  $V$ , while  $\delta_3$  is a physiological reabsorption rate.

In order to deal with more manageable quantities, it is advisable making the system (3.1) non-dimensionalized, as already done in [30], so that we have

$$\begin{cases} \frac{\partial u}{\partial t} = u(1 - u) - duw \\ \frac{\partial v}{\partial t} = rv(1 - v) + D \frac{\partial}{\partial x} \left[ (1 - u) \frac{\partial v}{\partial x} \right] \\ \frac{\partial w}{\partial t} = c(v - w) + \frac{\partial^2 w}{\partial x^2} \end{cases} \quad (3.2)$$

and the experimental domain is assumed to be the one-dimensional interval  $[-L, L]$ , with  $t \geq 0$ . This resultant version allows to operate with fewer (positive) parameters  $d$ ,  $r$ ,  $D$  and  $c$ , thus reducing their original range and coping with scaled functions  $u(x, t)$ ,  $v(x, t)$  and  $w(x, t)$ . As regards the boundary data, the homogeneous Neumann problem is contemplated for the numerical simulations.

For the one-dimensional framework, a comprehensive study of the traveling fronts associated to the Gatenby-Gawlinski model (3.1) is performed in [26] to identify the key qualitative features of wave propagation, because no rigorous proof of the existence of traveling waves seems to be presently available. By making use of *matched asymptotic expansions*, the system of traveling wave solutions with suitable asymptotic and boundary conditions is analyzed after appropriate rescaling; moreover, conditions for the appearance of a *tumour-host interstitial gap* are provided, thus confirming and extending the estimates proposed in [30, 32]. The numerical results shown in Section 3.4 are consistent with those illustrated in [26].

We conclude this section by mentioning that a generalized version of (3.1) and (3.2) is proposed in [60], including terms for acid-mediated tumour cells death and mutual competition between healthy and cancer cells. Other models for tu-

mour invasion for which the existence of propagating fronts is crucial are based on combined mechanisms of extracellular matrix dynamics and haptotaxis [75, 76].

### 3.3 The numerical algorithm

We have adopted a numerical strategy based on cell-centered finite volume approximations for the spatial discretization (refer to [100], for instance). The choice of a *finite volume method* is motivated by the possibility of relying on the integral formulation of the system equations, that is a suitable ground to guarantee consistency in terms of closeness to the physics of the model.

In order to derive a semi-discrete finite volume approximation, we firstly look at the general case of a nonuniform mesh and impose that  $Z_i = [x_{i-\frac{1}{2}}, x_{i+\frac{1}{2}})$  is the finite volume centered at  $x_i = \frac{x_{i-\frac{1}{2}} + x_{i+\frac{1}{2}}}{2}$ , for  $i = 1, 2, \dots, N$ , where  $N$  is a fixed number of vertices to be selected on the one-dimensional mesh.

Let  $\Delta x_i = |x_{i+\frac{1}{2}} - x_{i-\frac{1}{2}}|$  be the (variable) spatial mesh size, so that  $|x_i - x_{i-1}| = \frac{\Delta x_{i-1}}{2} + \frac{\Delta x_i}{2}$  is the typical length for an interfacial interval (see Figure 3.2).

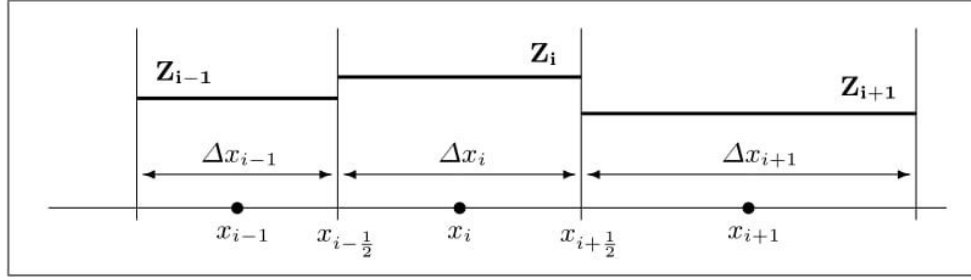


Figure 3.2. Piece-wise constant reconstruction on nonuniform mesh.

We start by taking into account the equation for the healthy tissue density in (3.2) and we examine its finite volume integral version,

$$\frac{1}{\Delta x_i} \int_{Z_i} \frac{\partial u}{\partial t}(x, t) dx = \frac{1}{\Delta x_i} \int_{Z_i} u(x, t)(1 - u(x, t)) dx - \frac{d}{\Delta x_i} \int_{Z_i} u(x, t)w(x, t) dx ,$$

which can be handled by introducing the usual notation for finite volume integral averages, namely  $u_i(t) \simeq \frac{1}{\Delta x_i} \int_{Z_i} u(x, t) dx$ , hence the semi-discrete equation reads

$$\frac{d}{dt} u_i(t) = u_i(t)(1 - u_i(t)) - d u_i(t)w_i(t) . \quad (3.3)$$

Similarly, the equation for the tumour cells density in (3.2) is rewritten as

$$\begin{aligned} \frac{1}{\Delta x_i} \int_{Z_i} \frac{\partial v}{\partial t}(x, t) dx &= \frac{r}{\Delta x_i} \int_{Z_i} v(x, t)(1 - v(x, t)) dx \\ &+ \frac{D}{\Delta x_i} \int_{Z_i} \frac{\partial}{\partial x} \left[ (1 - u(x, t)) \frac{\partial v}{\partial x}(x, t) \right] dx \end{aligned}$$

and a suitable approach must be arranged for the finite volume integral average of the diffusion term. In particular, we proceed by evaluating the differential term at the mesh interfaces as follows,

$$\begin{aligned} &\frac{D}{\Delta x_i} \left[ (1 - u(x_{i+\frac{1}{2}}, t)) \frac{\partial v}{\partial x}(x_{i+\frac{1}{2}}, t) - (1 - u(x_{i-\frac{1}{2}}, t)) \frac{\partial v}{\partial x}(x_{i-\frac{1}{2}}, t) \right] \\ &\simeq \frac{D}{\Delta x_i} \left[ \frac{(1 - u_i(t))\Delta x_i + (1 - u_{i+1}(t))\Delta x_{i+1}}{\Delta x_i + \Delta x_{i+1}} \cdot \frac{v_{i+1}(t) - v_i(t)}{\frac{\Delta x_i}{2} + \frac{\Delta x_{i+1}}{2}} \right. \\ &\quad \left. - \frac{(1 - u_{i-1}(t))\Delta x_{i-1} + (1 - u_i(t))\Delta x_i}{\Delta x_{i-1} + \Delta x_i} \cdot \frac{v_i(t) - v_{i-1}(t)}{\frac{\Delta x_{i-1}}{2} + \frac{\Delta x_i}{2}} \right], \end{aligned} \quad (3.4)$$

where the interfacial quantities are approximated by building weighted averages whose weights are the size of the adjacent finite volumes, so that  $\Delta x_i/\Delta x_{i+1}$  and  $\Delta x_{i-1}/\Delta x_i$  are employed at the interfaces  $x_{i+\frac{1}{2}}$  and  $x_{i-\frac{1}{2}}$ , respectively. The first order derivatives of  $v(x, t)$  are discretized by means of an interfacial formula which makes use of the function evaluations at the neighboring vertices.

Finally, as concerns the equation for the extracellular lactic acid in (3.2), we have

$$\begin{aligned} \frac{1}{\Delta x_i} \int_{Z_i} \frac{\partial w}{\partial t}(x, t) dx &= \frac{c}{\Delta x_i} \int_{Z_i} v(x, t) dx - \frac{c}{\Delta x_i} \int_{Z_i} w(x, t) dx \\ &+ \frac{1}{\Delta x_i} \int_{Z_i} \frac{\partial^2 w}{\partial x^2}(x, t) dx \end{aligned}$$

and, by proceeding as for the previous cases, we derive the approximation

$$\frac{d}{dt} w_i(t) = c(v_i(t) - w_i(t)) + \frac{1}{\Delta x_i} \left[ \frac{w_{i+1}(t) - w_i(t)}{\frac{\Delta x_i}{2} + \frac{\Delta x_{i+1}}{2}} - \frac{w_i(t) - w_{i-1}(t)}{\frac{\Delta x_{i-1}}{2} + \frac{\Delta x_i}{2}} \right]. \quad (3.5)$$

Henceforward, for the sake of simplicity, the quantity  $\Delta x_i$  is assumed to be constant, namely  $\Delta x_i = \Delta x$  for all  $i = 1, 2, \dots, N$ . Consequently, from (3.4) the

semi-discrete version of the equation for the cancer cells density becomes

$$\frac{d}{dt}v_i(t) = r v_i(t)(1 - v_i(t)) + \frac{D}{\Delta x} \left[ \frac{(1 - u_i(t)) + (1 - u_{i+1}(t))}{2} \cdot \frac{v_{i+1}(t) - v_i(t)}{\Delta x} - \frac{(1 - u_{i-1}(t)) + (1 - u_i(t))}{2} \cdot \frac{v_i(t) - v_{i-1}(t)}{\Delta x} \right]$$

and, after some conventional manipulations, it can be rearranged to get

$$\begin{aligned} \frac{d}{dt}v_i(t) = r v_i(t)(1 - v_i(t)) + \frac{D}{\Delta x^2} & \left[ (1 - u_i(t))(v_{i+1}(t) - 2v_i(t) + v_{i-1}(t)) \right. \\ & - \frac{1}{2}(v_{i+1}(t) - v_i(t))(u_{i+1}(t) - u_i(t)) \\ & \left. - \frac{1}{2}(v_i(t) - v_{i-1}(t))(u_i(t) - u_{i-1}(t)) \right]. \end{aligned} \quad (3.6)$$

Finally, the equation (3.5) in the case of a uniform mesh reads

$$\frac{d}{dt}w_i(t) = c(v_i(t) - w_i(t)) + \frac{w_{i+1}(t) - 2w_i(t) + w_{i-1}(t)}{\Delta x^2}. \quad (3.7)$$

It is worth noticing that approximation (3.6) exhibits a structure in which the presence of the discrete Laplace operator is recognizable, along with extra terms consisting of products of interfacial discretizations. These terms arise from the degenerate diffusion in the second equation of (3.2) and, indeed, the finite volume approach we have proposed leads to a diffusion splitting by autonomously selecting the first and second order contributions. By contrast, an algebraic manipulation culminating in a early separation, as it could be done for deriving finite difference schemes [78], it would entail the necessity of relying on a central discretization for the first order terms, thus not being allowed to choose a suitable propagation direction. As a consequence, the scheme provided with central approximations would prove itself to be far less stable.

For the time discretization of the semi-discrete system obtained by grouping (3.3), (3.6) and (3.7), we employ a semi-implicit strategy considering a fixed time step  $\Delta t$ , so that  $\Delta t = |t^{n+1} - t^n|$ , for  $n = 0, 1, \dots$ . In particular, the reaction terms are treated explicitly, while the differential terms on the right-hand sides

are approximated implicitly, as follows,

$$\left\{ \begin{array}{l} u_i^{n+1} = u_i^n + \Delta t \left[ u_i^n (1 - u_i^n) - d u_i^n w_i^n \right] \\ v_i^{n+1} = v_i^n + r \Delta t v_i^n (1 - v_i^n) \\ \quad + D \frac{\Delta t}{\Delta x^2} \left[ (1 - u_i^{n+1}) (v_{i+1}^{n+1} - 2 v_i^{n+1} + v_{i-1}^{n+1}) \right. \\ \quad \quad \left. - \frac{1}{2} (v_{i+1}^{n+1} - v_i^{n+1}) (u_{i+1}^{n+1} - u_i^{n+1}) \right. \\ \quad \quad \left. - \frac{1}{2} (v_i^{n+1} - v_{i-1}^{n+1}) (u_i^{n+1} - u_{i-1}^{n+1}) \right] \\ w_i^{n+1} = w_i^n + c \Delta t (v_i^n - w_i^n) + \frac{\Delta t}{\Delta x^2} (w_{i-1}^{n+1} - 2 w_i^{n+1} + w_{i+1}^{n+1}) \end{array} \right. \quad (3.8)$$

and Neumann-type boundary conditions  $u_1^n = u_2^n$ ,  $v_1^n = v_2^n$  and  $w_1^n = w_2^n$ , for  $n = 1, 2, \dots$  are also implemented. This explicit-implicit mixed approach allows to make less expensive choices for the time step, by contrast with purely explicit algorithms which would be heavily conditioned by the restrictions that stability usually requires. The possibility of adopting fully implicit schemes has also been considered, but such an idea has not been finally taken into account since no considerable accuracy in the approximation would have been gained but an increase of the computational time.

We point out that, in order to efficiently solve the discrete system (3.8), it is useful starting from the solution  $u^{n+1}$  for the healthy tissue, whose treatment turns out to be fully explicit; afterwards, by exploiting the block-matrix structure arising from the other equations, thus producing a reciprocal independence between the solutions  $v^{n+1}$  and  $w^{n+1}$ , it is easy to go ahead solving separately the corresponding equations and getting the global approximation evaluated at the discrete time  $t^{n+1}$ .

### 3.4 One-dimensional simulation results

Once a suitable numerical framework has been established, the natural step to be taken in order to proceed with experiments and simulations consists in defining a useful tool for the *wave speed estimation* of the numerical solutions. As a matter of fact, the most interesting qualitative feature arising from the analysis of the solutions to system (3.2) is the detection of the *traveling fronts* phenomenon [84]. Therefore, trying to quantify the associated wave speed becomes a necessary path to follow for verifying the existence of an asymptotic threshold. According to the strategy proposed in [52], with the aim of providing a numerical approximation for the wave speed of the function  $v$  at time  $t^n$ , we employ the space-averaged estimate (2.19).

In order to validate the numerical algorithm, numerical simulations have been performed using the scheme (3.8), together with the wave speed estimate. In this section, we are interested in recovering computational results described in the literature [26, 30, 32], therefore the experiments are carried out with the scaled parameters available in [60], as listed in Table 3.1, and then with the parameters in [26], as listed in Table 3.2. Besides the quantities already discussed for the model presentation in Section 3.2, we assume  $T$  as the final time instant, while the spatio-temporal mesh is built by fixing  $\Delta x = 0.005$  and  $\Delta t = 0.01$ .

Table 3.1: Numerical values for the simulation parameters [60].

$d$	$r$	$D$	$c$	$L$	$T$
$\{0.5, 1.5, 2.5, 3, 12.5\}$	1	$4 \cdot 10^{-5}$	70	1	20

For the choice of the initial profiles, according to what proposed in [60], a piecewise linear decreasing density is taken into account for the cancer cells extending out from its core, where  $v = 1$ , and getting towards zero; for the healthy cells density, the starting graph is simply obtained through a reflection, by imposing a complementary behaviour with respect to the cancer cells density; finally, the extracellular lactic acid concentration is initially equal to zero. The corresponding graphs are shown in Figure 3.3.

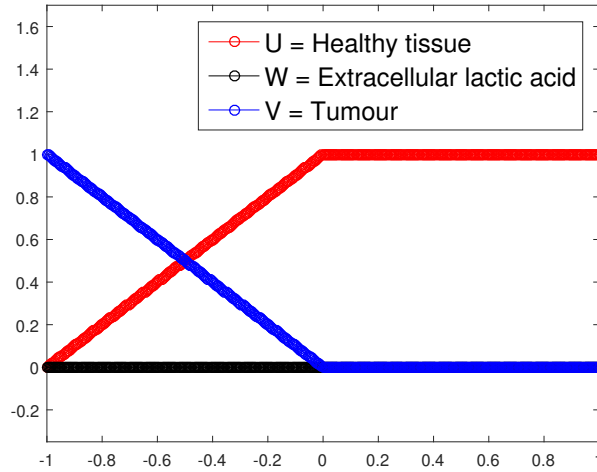


Figure 3.3. Graphs of the initial profiles for the numerical experiments.

The simulation results exhibit basically two different kinds of behaviours, both reported in Figure 3.4, which are regulated by the parameter  $d$  measuring the destructive influence of the environment acidity on the healthy tissue, and so



taken as an indicator of the tumour aggressiveness. From a qualitative point of view, all solutions evolve as forward propagation fronts moving from left to right with positive wave speed. The plot shown in Figure 3.4(a) corresponds to a phenomenological regime known as *heterogeneous invasion*, which turns out to happen when the condition  $d < 1$  is verified. It is characterized by the coexistence of tumour and healthy tissue behind the wavefront, because a fraction of normal cells survives to the chemical action of the tumour thanks to low sensitivity to the environment acidity. We remark that the boundary data considered in [26] are slightly different from those adopted for our numerical simulations, but the model dynamics implies that acid concentration immediately attains its carrying capacity at the left-hand boundary, and finally the level of the healthy cells density is exactly  $1 - d$  in the purely heterogeneous case.

On the other hand, when  $d \gg 1$ , a different evolution shape takes place, the so-called *homogeneous invasion* depicted in Figure 3.4(d), that is the most aggressive configuration. Indeed, the healthy tissue is being completely destroyed behind the advancing tumour cells wavefront because of the high level of acidity induced into the environment. A narrow overlapping zone actually persists for increasing values of  $d > 1$ , which produces *hybrid configurations* as shown in Figure 3.4(b) and Figure 3.4(c), but it reduces progressively as forecasted in [26]. A remarkable feature of the last configuration is the presence of a *tumour-host hypocellular interstitial gap*, namely a separation zone between the healthy and cancer cells populations. Such prediction, initially a mere mathematical result provided by the model, has been experimentally verified: its detection, in both unfixed in vitro experiments and in flash-frozen tissues, has provided stronger evidence to claim this phenomenon authentication [30]. Finally, as regards the lactic acid concentration, in all cases it tracks the tumour front with a smoother profile. These results are in agreement with the corresponding records provided in [60], aimed at recovering the dynamics firstly analyzed in [30].

From a mathematical point of view, the strong dissimilarity in terms of steepness of the wave profiles for the healthy and tumours densities observed in Figure 3.4 is justified by the fact that somehow  $U$  inherits the (parabolic) regularity of the acid concentration  $W$  through the reaction term, whereas the diffusion constant  $D$  of the neoplastic tissue is typically very small (refer to Table 3.1). As a matter of fact, when passing from the system (3.1) to its non-dimensionalized version (3.2), that parameter is deduced as  $D = D_2/D_3$  and it is physically relevant to assume that  $D_3$  is much larger than  $D_2$ . Therefore, the tumour propagating front  $V$  is normally steeper, despite its diffusivity (hindered by  $U$  through a degenerate factor) is selected as the driving mechanism of invasion, since no diffusion is considered for the healthy cells due to their epithelial phenotype [92]. Indeed, the wavefront  $U$  fails to keep its regularity once the equation for  $W$  is removed

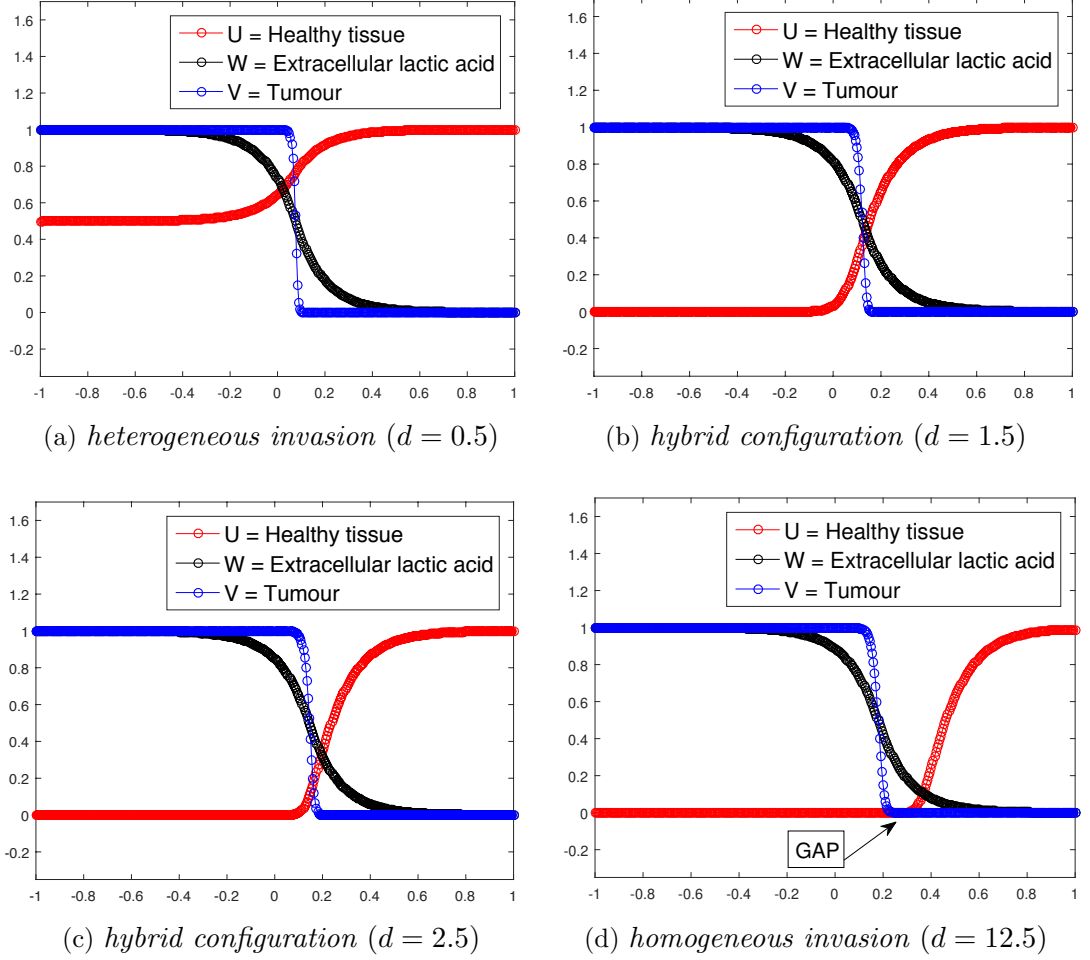


Figure 3.4. Different configurations of the numerical solution: comparison between heterogeneous evolution (a) and existence of the spatial interstitial *gap* within the homogeneous evolution (d).

from system (3.1), as demonstrated numerically in Figure 3.10 for the reduced model (3.9) in Section 3.5.

Another effect on the shape of the wave profiles can be appreciated dealing with the adimensional parameter  $r$ , which is expected to be greater than 1 since deduced as  $r = \rho_2/\rho_1$  from physical considerations (we report in Figure 3.5 the numerical simulation of an experimental case discussed in [26], for example).

We have attempted a qualitative comparison with the analytical results in [26] by computing numerical solutions using the parameters listed in Table 3.2. In particular, we are interested in tracking the formation of the interstitial *gap*, whose appearance is expected for  $d > 2$  (in which case its size can also be estimated).

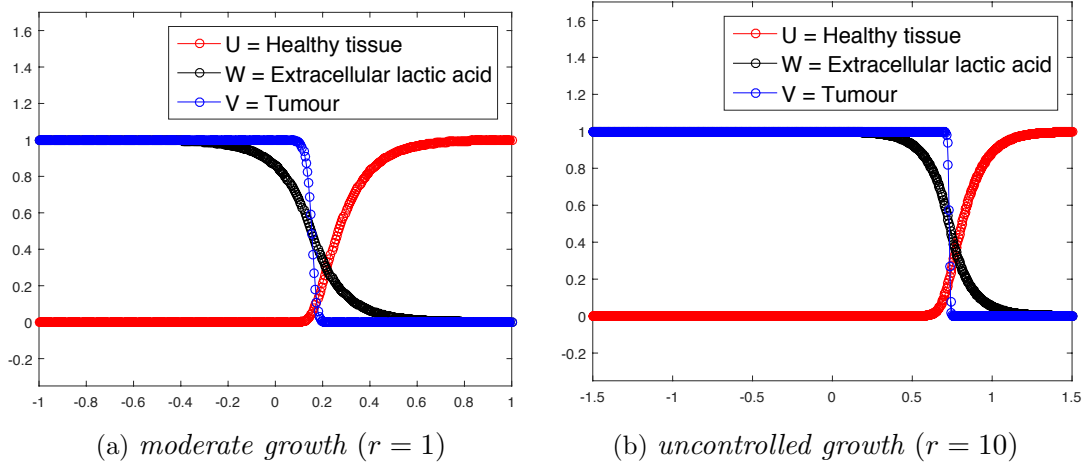


Figure 3.5. Qualitative analysis of tumour fronts steepness and spatial invasion as function of the adimensional growth rate (for  $d = 3$ ).

Table 3.2: Numerical values for the simulation parameters [26].

$d$	$r$	$D$	$c$	$L$	$T$
$\{1.5, 2.5, 4\}$	1	$4 \cdot 10^{-5}$	2	5	20

The numerical simulations reported in Figure 3.6 actually corroborate such prediction, although some discrepancies emerge concerning the smoothness of the wave profile for the healthy cells density, thus determining a smaller size for the *gap* separating the host and tumour populations. Besides the effects of a bigger diffusion constant  $D$  for the tumour cells, which slightly smooths out the steepness of the propagating fronts, we must recall that the analysis in [26] is based on asymptotic expansions and, therefore, solely the leading terms contribute to shape the solution profiles (this comment applies also to Figure 3.5).

As already mentioned above, the existence of propagating fronts is a key point for our investigation and information about their wave speed is crucial. In order to quantify these values, we take advantage of the space-averaged propagation speed approximation (2.19) and we apply it to better understand the wavefronts behaviour of the Gatenby-Gawinski model. For instance, graphs related to the heterogeneous invasion are considered: the plot proposed in Figure 3.7(a) is meant for capturing front evolution starting from the initial profile and, by means of different colors, the tumour cells density function is plotted at different times until it reaches the shape of a propagating front defined by a stable wave speed. The graph in Figure 3.7(b) shows the discrete wave speed estimate (2.19) computed

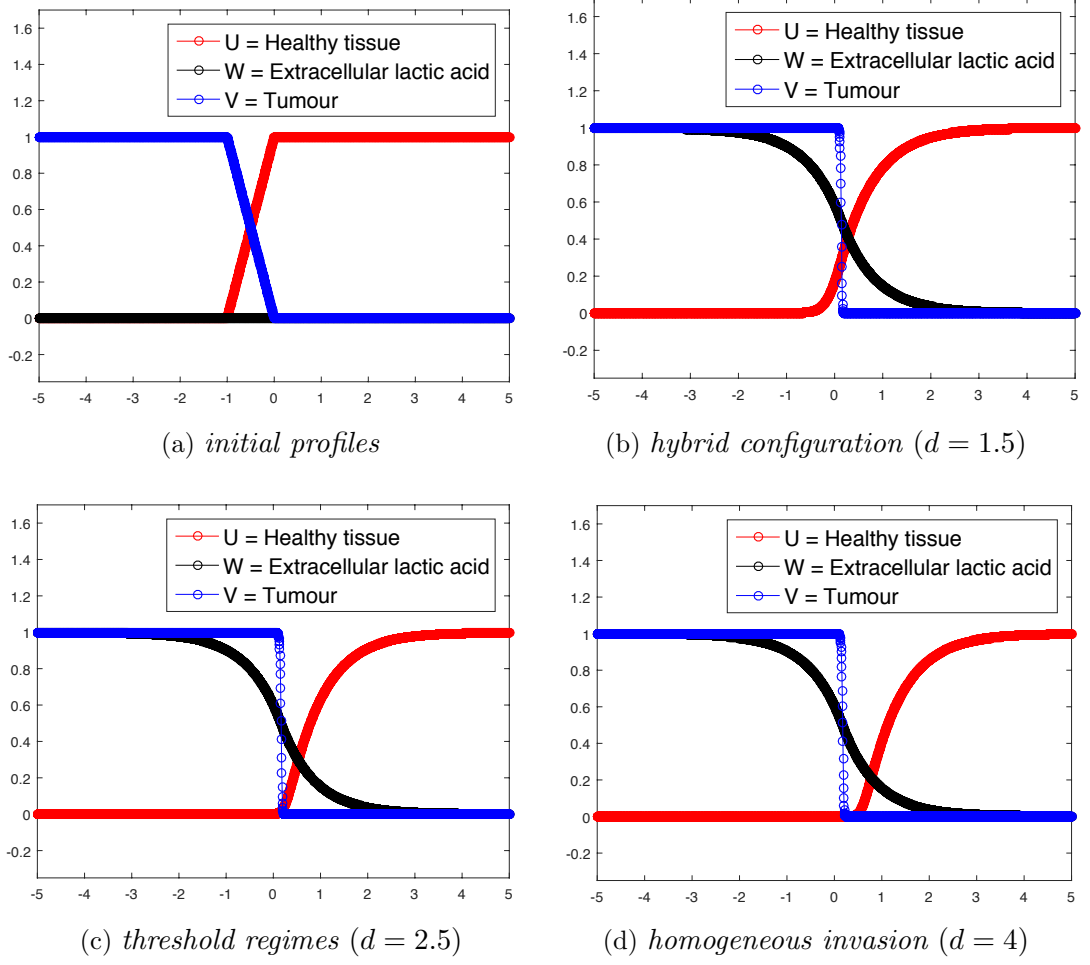


Figure 3.6. Numerical simulation of the spatial interstitial *gap* formation from heterogeneous evolution (b) to homogeneous invasion (d).

as a function of time, and it is possible to appreciate the convergence towards the asymptotic threshold; furthermore, it is easy to verify that a small waiting time is required before achieving an asymptotic value, that is a common feature of theories involving traveling fronts, simply recognizable by dealing with scalar problems. An analogous graph, of course, can be plotted in the homogeneous invasion case.

It is presently useful recalling the results of analytical asymptotic wave speed estimates provided in [60]. In Table 3.3 the discrete asymptotic wave speed approximations issued from (2.19) are listed in order to make a comparison: in both the homogeneous and heterogeneous cases, the relative error we get is sufficiently small to infer that numerical values are very close to the corresponding quantities

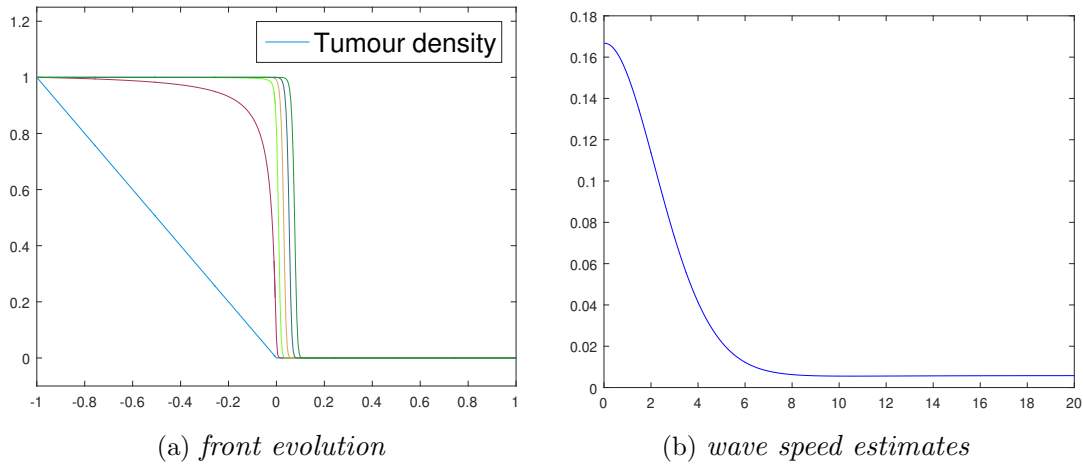


Figure 3.7. Traveling fronts investigation in the heterogeneous invasion case: the tumour density profile is plotted at six equally spaced time instants (a), together with the space-averaged propagation speed approximations as a function of time (b).

computable by using the analytical formulations available in [60]. Moreover, it is interesting to notice that, at least in the homogeneous case, the wave speed prediction  $s \approx 2\sqrt{Dr}$  perfectly matches the analytical formula already known for the Fisher-KPP equation [41, 96].

Table 3.3: Comparison between analytical wave speed formulations [60] and the numerical estimates issued from (2.19).

investigation case	numerics	analytical wave speed	relative error
homogeneous	0.0124	$s \approx 2\sqrt{Dr} = 0.0126$	0.0159
heterogeneous	0.0058	$s \approx \sqrt{2Ddr} = 0.0063$	0.0794

### 3.5 Some useful model reductions

Once that our numerical strategy and the space-averaged propagation speed estimate have been tested, we proceed by setting some simplified versions of the model. The purpose consists in carving a more approachable structure to pursue analytical investigations, trying to set ground rules both for a better mathematical understanding and, as much as possible, for keeping accuracy with respect to the original biomedical phenomena. Firstly we set up a two-equations-based model reduction, exploiting for numerical simulations the explicit-implicit approach de-

scribed in Section 3.3; afterwards, we define a one-equation-based reduction theoretically framed in the degenerate reaction-diffusion equations field [56, 82, 83, 84, 85, 86] and rely on the numerical strategy employed in Section 3.3 as concerns the spatial discretization, while an explicit treatment is taken into account for the time discretization.

### 3.5.1 Two-equations-based model reduction

The assumption we lean on to get a two-equations-based reduction consists in imposing the condition  $w = v$  inside the system (3.2), thus getting a simplified model, namely

$$\begin{cases} \frac{\partial u}{\partial t} = u(1 - u) - duv \\ \frac{\partial v}{\partial t} = rv(1 - v) + D \frac{\partial}{\partial x} \left[ (1 - u) \frac{\partial v}{\partial x} \right] \end{cases} \quad (3.9)$$

and the corresponding homogeneous Neumann boundary data. Such a simplification is achievable taking into account the limit as the parameter  $c$  approaches the infinity inside the third equation of the full model (3.2), and that is motivated by the similarity between tumour cells and lactic acid evolution profiles (see Figure 3.4).

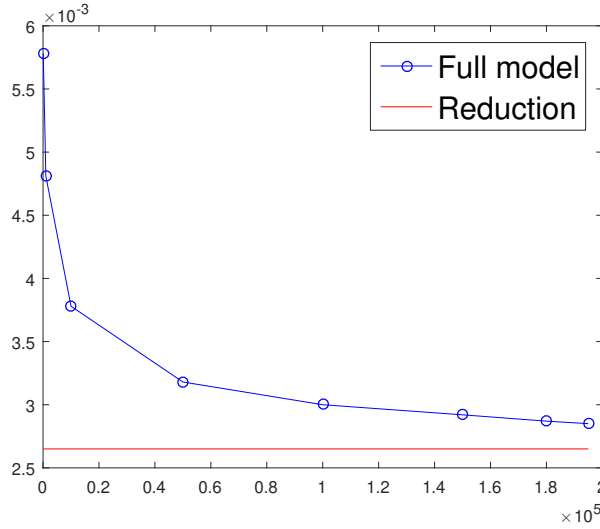


Figure 3.8. Wave speed estimates (blue circles) for increasing  $c$  values within the full model (3.2) and wave speed estimate (red line) provided by the simplified model (3.9).

An interesting analysis can be performed from the graph depicted in Figure 3.8, where the heterogeneous case is considered as an example: for each choice of the

$c$  value, the corresponding propagation speed approximation for the tumour cells density front provided by the Gatenby-Gawliniski model (3.2) is reported, as well as the (constant) wave speed estimate for the simplified model (3.9).

Because this quantity is an asymptotic threshold for the full model, by increasing the  $c$  value a convergence towards the asymptotic regime is expected. At this stage, a further discussion is required since, on the one hand, it is possible to appreciate the convergence, but on the other hand we easily infer that the statement  $w = v$  prevents the reduction from keeping the same wave speed produced by the complete model, thus exhibiting a quantitative mismatch. Specifically, the wave speed computed for the simplified model turns out to be smaller than the asymptotic value achieved by the full model. Such behaviour can be explained noticing that the standard diffusion of the lactic acid concentration in the third equation of (3.2) actually makes it easier to spread for the tumour cells, whose density expansion already relies on the degenerate diffusion term. As a consequence, the tumour spreading is slower for the reduced model (3.9), being no longer sustained by two distinct diffusion mechanisms.

The next step consists in testing numerically our model adjustment by using the same initial profiles (see Figure 3.3) and parameters (see Table 3.1) as for the previous simulations of the standard version in Section 3.4, but omitting the equation for the lactic acid concentration whatever concerns, as shown in Figure 3.9.

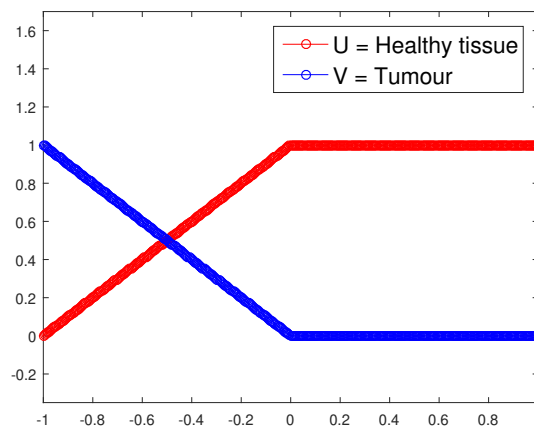


Figure 3.9. Graphs of the initial profiles for the simplified model.

The reduced system (3.9) is still able to reproduce important qualitative features of the full version (3.2), as it can be detected in Figure 3.10, and what is essential for performing a consistent mathematical analysis of the mechanisms underlying the Gatenby-Gawliniski model is the propagating fronts structure. The plots, for both the heterogeneous and homogeneous cases, exhibit similar qualitative behaviours

compared to the analogous graphs in Figure 3.4, although some quantitative differences are obviously detectable.

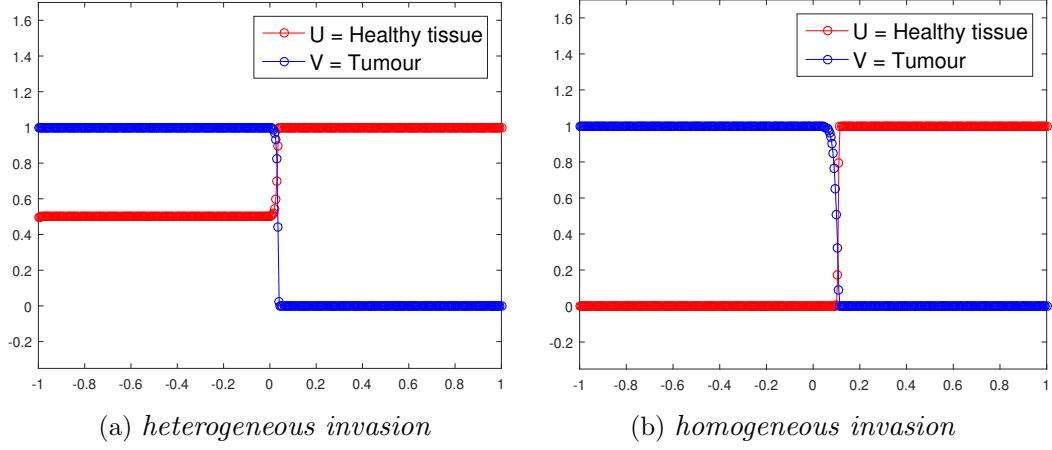


Figure 3.10. Comparison between two different regimes of the numerical solutions for the reduced model configuration.

In order to ensure a better understanding of the dynamics under investigation, for completing the analysis of the heterogeneous case, it is useful to report the same plots as previously shown in Figure 3.7 but contextualized in the model reduction framework. The front evolution for the tumour cells density is plotted in

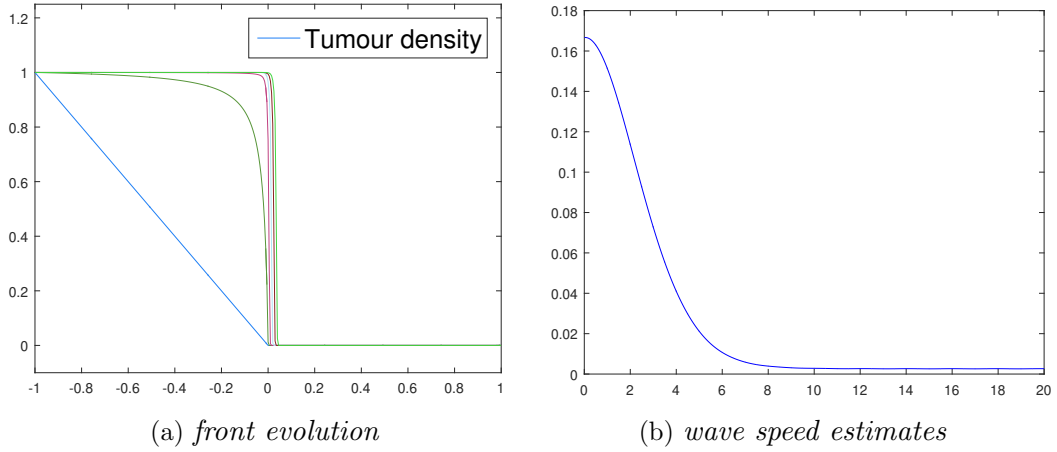


Figure 3.11. Traveling fronts investigation in the heterogeneous invasion case for the reduced model: the tumour density profile is plotted at six equally spaced time instants (a), together with the space-averaged propagation speed approximations as a function of time (b).



Figure 3.11(a) and the discrete wave speed estimates are taken into account in Figure 3.11(b). Despite the wave speed threshold has changed with respect to the value for the full system in Figure 3.7(b), the model reduction upholds the same qualitative structure: indeed, the traveling fronts formation is still observable as well as the wave speed convergence towards a stable default value. Therefore, the transition occurring within the full model (3.2) as the  $c$  value approaches infinity does not prevent the system from keeping its mathematical features. However, we point out that the *gap* formation is no longer recognizable for the simplified model (3.9), and indeed in Section 3.4 we have already observed a delay in its appearance for higher values of the  $c$  parameter from Figure 3.4 with respect to Figure 3.6. Therefore, we can conjecture that for its detection assuming an independent evolution for the lactic acid concentration is needed. That is why, relying on the complete model is required in order to seize the whole biomedical phenomenon, regardless of any employable reductions for performing further mathematical analysis.

### 3.5.2 One-equation-based model reduction

With the aim of getting a one-equation reduction for the Gatenby-Gawliniski model, it is useful to normalize the coefficient  $D$  for the second equation in (3.9). This goal is accomplished imposing the following rescaling

$$\sqrt{D} \frac{\partial}{\partial x} = \frac{\partial}{\partial y},$$

under which, by renaming the variable  $y$  to  $x$ , it is possible to get a two-parameters-dependent reduction that reads as

$$\begin{cases} \frac{\partial u}{\partial t} = u(1 - u) - duv \\ \frac{\partial v}{\partial t} = rv(1 - v) + \frac{\partial}{\partial x} \left[ (1 - u) \frac{\partial v}{\partial x} \right]. \end{cases} \quad (3.10)$$

After that, we consider the system (3.10) and assume the stationarity for the healthy tissue density equation, leading to  $u(1 - u - dv) = 0$ ; finally we impose that

$$u = (1 - dv)^+. \quad (3.11)$$

As a consequence, the tumour cells equation turns out to show the following structure

$$\frac{\partial v}{\partial t} = rv(1 - v) + \frac{\partial}{\partial x} \left[ F(u) \Big|_{u=(1-dv)^+} \frac{\partial v}{\partial x} \right], \quad (3.12)$$

where the degenerate diffusion term is a piecewise linear function defined as

$$F(u)|_{u=(1-dv)^+} = 1 - u|_{u=(1-dv)^+} = 1 - (1 - dv)^+ = \begin{cases} dv & \text{if } v \in [0, \frac{1}{d}) \\ 1 & \text{if } v \in [\frac{1}{d}, 1]. \end{cases} \quad (3.13)$$

Our reduction (3.12) is a degenerate reaction-diffusion equation and the diffusion  $F$  is almost everywhere differentiable, due to the discontinuity located in  $v = \frac{1}{d}$  for the derivative.

An interesting investigation to be carried out, relies in detecting information about the shape of the corresponding traveling waves: specifically, we want to figure out if the fronts exhibit a *sharp-type* or *front-type* trend. Technically, taking as main guideline the traveling waves problem defined by the following one-dimensional, degenerate, reaction-diffusion equation,

$$\frac{\partial v}{\partial t} = \frac{\partial}{\partial x} \left[ F(v) \frac{\partial v}{\partial x} \right] + g(v) \quad \text{with } (x, t) \in (\mathbb{R} \times \mathbb{R}^+), \quad (3.14)$$

where  $g(v)$  is a Fisher-KPP type reaction term,  $F(v)$  is the degenerate diffusion such that  $v \in [0, 1]$  and  $F'(0) \neq 0$ , then, the definition of *sharpness*, according to [84], reads as

**Definition 3.5.1** (sharp-type front). *If there exist a value of the wave speed  $s$ , let us call it  $s^*$ , and a value of  $\xi$ , let it be  $\xi^* \in (-\infty, +\infty]$ , such that  $\phi(x - s^*t) = \phi(\xi)$ , satisfying*

1.  $F(\phi)\phi'' + s^*\phi' + F'(\phi)[\phi']^2 + g(\phi) = 0 \quad \forall \xi \in (-\infty, \xi^*),$
2.  $\phi(-\infty) = 1, \quad \phi(\xi^*) = 0 \quad \text{and} \quad \phi' < 0 \quad \forall \xi \in (-\infty, \xi^*),$
3.  $\phi'(\xi^*) = -s^*/F'(0) \quad \text{and} \quad \phi(\xi) = 0 \quad \forall \xi \in (\xi^*, +\infty],$

where the superscript is meant to denote differentiation with respect to  $\xi$ , then the function  $v(x, t) = \phi(x - s^*t)$  is called a traveling wave solution of sharp-type for (3.14).

We point out that the other possibility allowed, happens when the function  $v(x, t)$  turns out to be a traveling wave of *front-type*, whose typical smoother trend makes this front to be known as a *smooth-type* wave as well. The former statement about the smoothness of the front-type traveling waves, is easily understandable thinking about the implications framed by the Definition 3.5.1. As a consequence, indeed, a sharp-type wave attains the equilibrium located in  $\mathbf{E} = 0$  in a finite time  $\xi^*$ , with negative slope  $\phi'(\xi^*) = -s^*/F'(0)$  [56], thus resulting a discontinuous derivative in  $\xi^*$ , since the left derivative tends to  $\phi'(\xi^{*-}) \neq 0$ , while the right

derivative tends to  $\phi'(\xi^{*+}) = 0$  [84]. By contrast, a smooth-type front exhibits a continuous derivative in  $\xi^*$ . This last observation provides us with a useful tool in order to quickly, qualitatively detect the distinctive trend for a given traveling wave, especially when the dynamics is ruled by more complex configurations with respect to (3.14).

As concerns the problem (3.14), theoretical results [56, 82, 84, 85] are available for ensuring the existence and uniqueness of sharp/smooth-type traveling waves, provided that some hypotheses about the regularity of the  $v$ -dependent functions  $F$  and  $g$  are satisfied (other outcomes are achieved in [83] for a specific choice of  $F$  and in [86] if  $g$  is a generalization of the Nagumo equation). The results available in [56] require at least the pointwise differentiability in  $[0, 1]$ , so that, strictly concerning the theoretical point of view, it is not possible to state the sharpness/smoothness of the fronts for the equation (3.12). As a matter of a fact, we decide to lean on the numerical assessment, although the possibility of employing a smooth approximation for by-passing the discontinuous point of  $F'$ , so that enough regularity [56, 84] might be ensured, would not seem to jeopardize a theoretical prediction of existence and uniqueness for the fronts in the case of (3.13) as well.

We stress that the reduction (3.12) might be easily rearranged to become a one-parameter-dependent equation, by means of the rescaling  $\partial/\partial t = r\partial/\partial \tau$ ,  $\partial/\partial x = \sqrt{r}\partial/\partial y$ . However, taking advantage of the constraint  $r = 1$  employed for carrying out simulations, it is possible to keep relying on (3.12) and get a one-parameter dependence anyway, thus leading to the following equation:

$$\frac{\partial v}{\partial t} = v(1 - v) + \frac{\partial}{\partial x} \left[ F(u) \Big|_{u=(1-dv)+} \frac{\partial v}{\partial x} \right]. \quad (3.15)$$

**The numerical algorithm** On the heels of what has already described in Section 3.3, we invoke the same cell-centered finite volume approximation for the spatial discretization of (3.15) and take care of considering the corresponding versions the piecewise linear diffusion (3.13) leads to, specifically we have

$$\frac{\partial v}{\partial t} = v(1 - v) + d \frac{\partial}{\partial x} \left( v \frac{\partial v}{\partial x} \right) \quad \text{if } v \in \left[ 0, \frac{1}{d} \right), \quad (3.16)$$

$$\frac{\partial v}{\partial t} = v(1 - v) + \frac{\partial^2 v}{\partial x^2} \quad \text{if } v \in \left[ \frac{1}{d}, 1 \right]. \quad (3.17)$$

The equation (3.16) can be rewritten to get

$$\begin{aligned} \frac{1}{\Delta x_i} \int_{Z_i} \frac{\partial v}{\partial t}(x, t) dx &= \frac{1}{\Delta x_i} \int_{Z_i} v(x, t)(1 - v(x, t)) dx \\ &\quad + \frac{d}{\Delta x_i} \int_{Z_i} \frac{\partial}{\partial x} \left( v(x, t) \frac{\partial v}{\partial x}(x, t) \right) dx \end{aligned}$$

where the finite volume integral average for the diffusion is dealt as follows

$$\begin{aligned} & \frac{d}{\Delta x_i} \left[ v(x_{i+\frac{1}{2}}, t) \frac{\partial v}{\partial x}(x_{i+\frac{1}{2}}, t) - v(x_{i-\frac{1}{2}}, t) \frac{\partial v}{\partial x}(x_{i-\frac{1}{2}}, t) \right] \\ & \simeq \frac{d}{\Delta x_i} \left[ \frac{v_i(t)\Delta x_i + v_{i+1}(t)\Delta x_{i+1}}{\Delta x_i + \Delta x_{i+1}} \cdot \frac{\frac{\Delta x_i}{2} + \frac{\Delta x_{i+1}}{2}}{\frac{\Delta x_i}{2} + \frac{\Delta x_{i+1}}{2}} \right. \\ & \quad \left. - \frac{v_{i-1}(t)\Delta x_{i-1} + v_i(t)\Delta x_i}{\Delta x_{i-1} + \Delta x_i} \cdot \frac{\frac{\Delta x_{i-1}}{2} + \frac{\Delta x_i}{2}}{\frac{\Delta x_{i-1}}{2} + \frac{\Delta x_i}{2}} \right]. \end{aligned}$$

Now, if the quantity  $\Delta x_i$  is constant, we get the following semi-discrete version

$$\begin{aligned} \frac{d}{dt} v_i(t) = & v_i(t)(1 - v_i(t)) + \frac{d}{\Delta x} \left[ \frac{v_i(t) + v_{i+1}(t)}{2} \cdot \frac{v_{i+1}(t) - v_i(t)}{\Delta x} \right. \\ & \left. - \frac{v_{i-1}(t) + v_i(t)}{2} \cdot \frac{v_i(t) - v_{i-1}(t)}{\Delta x} \right] \end{aligned}$$

which easily leads to

$$\begin{aligned} \frac{d}{dt} v_i(t) = & v_i(t)(1 - v_i(t)) + \frac{d}{\Delta x^2} \left[ v_i(t)(v_{i+1}(t) - 2v_i(t) + v_{i-1}(t)) \right. \\ & \left. + \frac{1}{2}(v_{i+1}(t) - v_i(t))^2 + \frac{1}{2}(v_i(t) - v_{i-1}(t))^2 \right]. \end{aligned} \quad (3.18)$$

As concerns the equation (3.17), by following the same path, in case of nonuniform mesh we have

$$\frac{d}{dt} v_i(t) = v_i(t)(1 - v_i(t)) + \frac{1}{\Delta x_i} \left[ \frac{v_{i+1}(t) - v_i(t)}{\frac{\Delta x_i}{2} + \frac{\Delta x_{i+1}}{2}} - \frac{v_i(t) - v_{i-1}(t)}{\frac{\Delta x_{i-1}}{2} + \frac{\Delta x_i}{2}} \right].$$

while, setting  $\Delta x_i$  as a constant value,

$$\frac{d}{dt} v_i(t) = v_i(t)(1 - v_i(t)) + \frac{v_{i+1}(t) - 2v_i(t) + v_{i-1}(t)}{\Delta x^2}. \quad (3.19)$$

For the time discretization of (3.18) and (3.19), we simply employ an explicit strategy, where  $\Delta t$  is the fixed time step, so that the final numerical scheme reads as

$$v_i^{n+1} = v_i^n + \Delta t v_i^n (1 - v_i^n) + H(v_{i+1}^n, v_i^n, v_{i-1}^n, \Delta x, \Delta t, d) \quad (3.20)$$

where the function  $H$  is defined as

$$H = \begin{cases} d \frac{\Delta t}{\Delta x^2} \left[ v_i^n (v_{i+1}^n - 2v_i^n + v_{i-1}^n) + \frac{1}{2} (v_{i+1}^n - v_i^n)^2 + \frac{1}{2} (v_i^n - v_{i-1}^n)^2 \right], \\ \quad \text{if } v_i^n \in \left[ 0, \frac{1}{d} \right) \\ \frac{\Delta t}{\Delta x^2} (v_{i+1}^n - 2v_i^n + v_{i-1}^n), \quad \text{if } v_i^n \in \left[ \frac{1}{d}, 1 \right]. \end{cases}$$

It is noticeable that the function  $H$  exhibits a jump due to the discontinuity located in  $v = 1/d$  for the derivative of the diffusion  $F$ . It is also important to point out that although the numerical scheme in (3.20) turns out to be conservative as long as either  $v_i^n \in [0, 1/d)$  or  $v_i^n \in [1/d, 1]$  for every suitable choice of  $i$  and  $n$ , such a property is lost when a transition between the regimes occurs. Nevertheless the numerical scheme is able to retrieve a conservative structure, as  $\Delta x \rightarrow 0$ .

**Simulations results** We take advantage of (3.20) and perform numerical simulations in order to validate our one-equation-based reduction (3.15) for the Gatenby-Gawlinski model. As regards the initial profile, we consider the Riemann problem whose states are  $\mathbf{P}_L = 1$  at the left and  $\mathbf{P}_R = 0$  at the right; all the parameters employed are listed in Table 3.4.

Table 3.4: Numerical default values for the parameters involved in the one-equation-based reduction.

$d$	$\Delta x$	$\Delta t$	$T$
$\{0.5, 2\}$	0.05	0.001	20

The results are depicted in Figure 3.12(a) and Figure 3.12(b) for the heterogeneous and homogeneous invasion, respectively, by means of the front evolution representation. The cancerous cells density is plotted at equally spaced time instants and, in both the cases, the corresponding traveling waves turn out to be of sharp-type.

For ensuring the effectiveness of the one-equation-based reduction (3.15), it is important to establish if trends related to tumour invasions are correctly caught. In this respect, Figure 3.12, as well as providing information about the sharpness of the fronts, certifies as cancerous cells front moves forward faster in the homogeneous invasion. Specifically, adopting the space-averaged estimate (2.19), we get  $s \approx 0.499958$  for the heterogeneous case and  $s \approx 0.968813$  for the homogeneous case: these two values are the asymptotic wave speeds of the tumour front. Figure 3.13 shows the discrete wave speed approximation computed as a function of

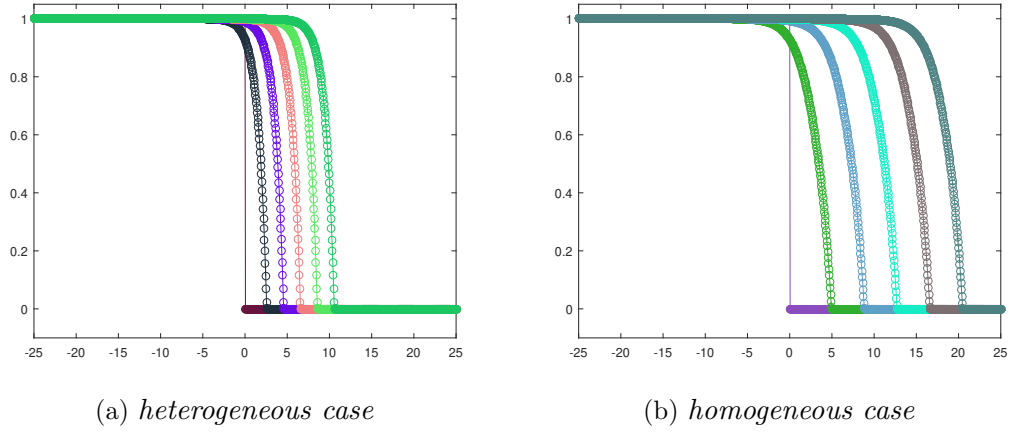


Figure 3.12. Front evolution for the tumour cells density in the heterogeneous case (a) and the homogeneous case (b). The parameters used are listed in Table 3.4.

time ( $d = 0.5$  is taken as a sample) and allows us to appreciate the convergence towards the corresponding asymptotic threshold.

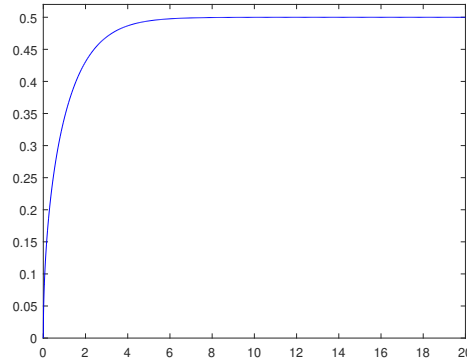


Figure 3.13. Space-averaged propagation speed approximations as a function of time for the heterogeneous invasion. The parameters used are listed in Table 3.4.

Finally, as further evidence of the reliability of (3.15), we can get information about the healthy cells density too, by simply leaning on (3.11). The related graphs are depicted in Figure 3.14(a) and Figure 3.14(b). The plots are realized by simultaneously reporting numerical approximations for the cancerous cells densities, along with the induced healthy cells densities defined by means of (3.11). The results qualitatively allow to retrieve the characteristic trends proper of the Gatenby-Gawlinski model.

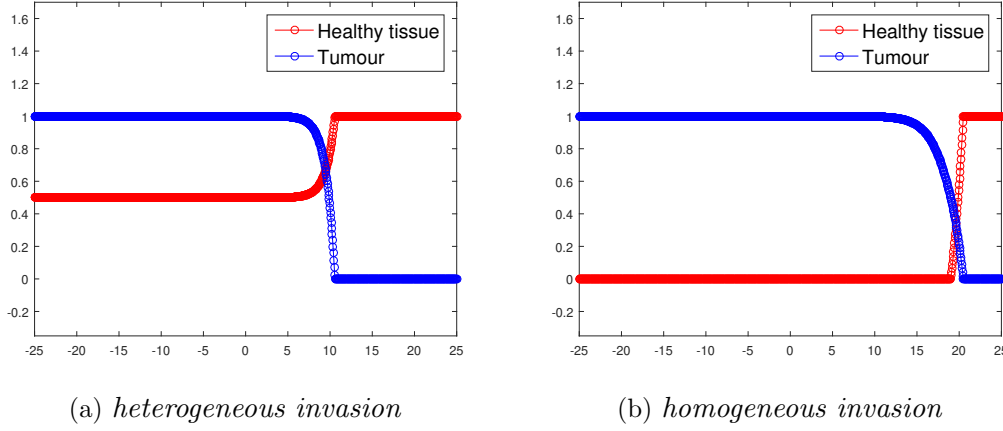


Figure 3.14. Numerical approximation of the tumour cells density along with the corresponding healthy cells profile, recovered by means of (3.11), for both the heterogeneous case (a) and the homogeneous case (b). The parameters used are listed in Table 3.4.

As far as the model described by (3.15), it is useful to notice that at least for the heterogeneous invasion, namely when  $d < 1$ , the diffusion term turns out to be identically  $F(v) = dv$ : in order to easily check this statement, recalling the  $F(v)$  definition in (3.13), it follows that  $v$  is always in  $[0, 1/d)$  if  $d < 1$ , being  $1/d > 1$  and taking in mind the constraint  $v \leq 1$ . Due to this fact, the one-equation-based model in this specific case becomes

$$\frac{\partial v}{\partial t} = v(1 - v) + d \frac{\partial}{\partial x} \left( v \frac{\partial v}{\partial x} \right). \quad (3.21)$$

For degenerate reaction-diffusion equations such as (3.21), it is possible to get an analytical solution [72, 73]. In this context, we simply impose that  $v(x, t)$  is a propagating front of the form  $\phi(x - st)$  being  $s$  the associated wave speed and, after some conventional operations, the exact solution reads as

$$v(x, t) = \begin{cases} 1 - \exp\left(\frac{1}{\sqrt{2d}}(x - st)\right) & \text{if } x \leq st \\ 0 & \text{if } x > st, \end{cases} \quad (3.22)$$

where  $s = \sqrt{d/2}$ . Assuming the previous choice  $d = 0.5$ , it follows that  $s = 0.5$ , which is a threshold very close to our numerical estimate  $s \approx 0.499958$ . For the sake of completeness, we provide a graphical check as well, the plot being depicted in Figure 3.15. We have chosen to exploit a refined spatio-temporal mesh, namely  $\Delta x = 0.01$  and  $\Delta t = 0.0001$ , compared to the parameters listed in Table 3.4, with

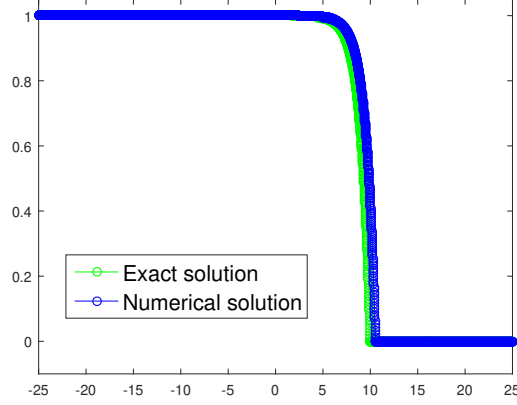


Figure 3.15. Exact solution and corresponding tumour density numerical approximation for the one-equation-based model in case of heterogeneous invasion.  $\Delta x = 0.01$  and  $\Delta t = 0.0001$  are the choices for the spacial and time steps, respectively.

the aim of achieving a very effective graphical result. The resulting trajectories are very close and the wave speed approximation is good too, being  $s \approx 0.499983$ .

Finally, by analogy with what has been shown in Section 3.5.1 in order to numerically appreciate the transition occurring from the complete Gatenby-Gawlinski model towards the two-equations-based reduction by increasing the parameter  $c$  in (3.2), we propose a similar analysis regarding the one-equation-based model. Indeed, recalling the assumption (3.11) exploited in (3.10) for justifying the model simplification, it is possible studying the transition occurring between the two-equations-based and the one-equation-based model by defining the  $\epsilon$ -dependent time derivative of the function  $u(x, t)$ . We get

$$\begin{cases} \epsilon \frac{\partial u}{\partial t} = u(1 - u) - duv \\ \frac{\partial v}{\partial t} = v(1 - v) + \frac{\partial}{\partial x} \left[ (1 - u) \frac{\partial v}{\partial x} \right] \end{cases} \quad (3.23)$$

At this stage, we can easily infer that, taking the limit as the parameter  $\epsilon$  approaches zero in the first equation of (3.23), perfectly matches, from a theoretical point of view, the idea behind the hypothesis (3.11), which automatically leads to (3.15). Now, we want to catch the transition, either employing the wave speed numerical estimate (2.19), which is the approach already exploited in Section 3.5.1, either taking advantage of the solution (3.22). As a matter of fact, considering the heterogeneous invasion context, we can rely on the exact solution for the one-equation-based model and exploit it to verify the transition from the two-equations reduction. Figure 3.16(a) exhibits the wave speed numerical approxima-



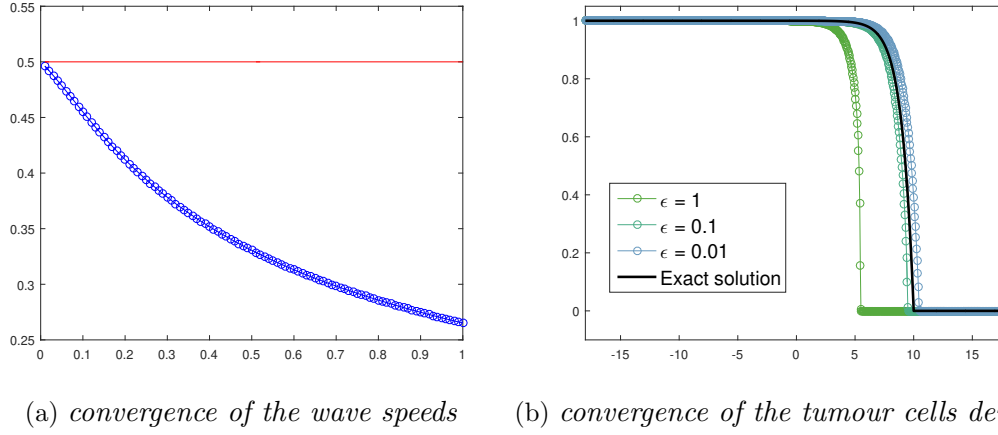


Figure 3.16. Wave speeds estimates (blue circles) for  $v(x, t)$  in (3.23) if  $\epsilon \in [0.01, 1]$  along with the wave speed analytical value (red line) provided by (3.22) (a) and convergence of the tumour density numerical approximation from (3.23), as a function of specific  $\epsilon$  values, towards the exact solution (3.22) (b). The parameters used are listed in Table 3.4.

tions achieved by assuming decreasing  $\epsilon$  values in (3.23) in the case of tumour cells front. The resulting trend correctly reports a convergence towards the asymptotic threshold  $s = 0.5$ , which is the analytical prediction for (3.21). Moreover, the exact solution (3.22) allows us to graphically recognize the transition towards (3.21) by means of a convergence check: Figure 3.16(b) reports the tumour density numerical approximation provided by (3.23) as a function of some  $\epsilon$  values taken as sample. It is possible to detect a progressive alignment with the analytical solution (3.22).

We conclude the section pointing out that the study of the Gatenby-Gawlinski model reductions is constantly under development: the next step consists in trying to extend the smoothness/sharpness investigation carried out for the one-equation-based reduction in order to get analytical and numerical results about the two-equations-based simplified version.

### 3.6 Multidimensional simulations

Henceforward, the analysis is carried out on the ground of two-dimensional and three-dimensional domains. The main purpose consists in exploring the multidimensional framework, both for recovering the qualitative features already exhibited in the one-dimensional context and for better investigating the phenomenon of the *gap* formation, along with its geometry and evolution. For the numerical strategy, the finite element method [78] has been employed, due to its versatility in dealing

with more complex geometric domains. Another advantage of this approach lies in avoiding specific treatment for the boundary conditions, which are automatically incorporated within the *weak formulation* of the system (refer to [79] for a similar methodology). Specifically, we have used *Lagrange P2 finite elements* for the numerical functions, while triangular and tetrahedral meshes have been adopted for two-dimensional and three-dimensional simulations, respectively (see Figure 3.17).

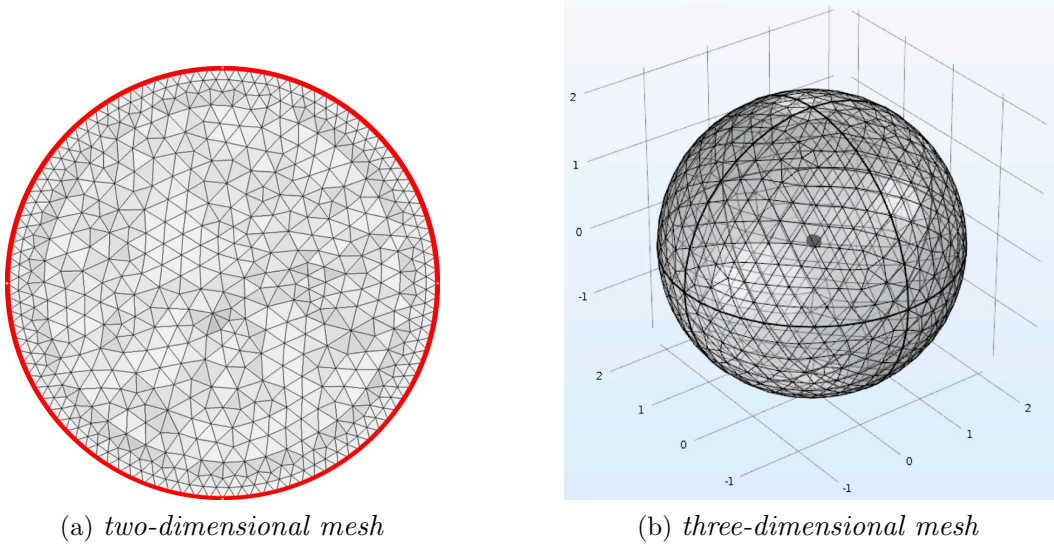


Figure 3.17. Finite element triangular (a) and tetrahedral (b) meshes for radially symmetric experimental domains.

We proceed to write the multidimensional non-dimensionalized Gatenby-Gawlinski model, namely the generalized version of system (3.2), as follows

$$\begin{cases} \frac{\partial u}{\partial t} = u(1 - u) - duw \\ \frac{\partial v}{\partial t} = rv(1 - v) + D \nabla \cdot [(1 - u) \nabla v] \\ \frac{\partial w}{\partial t} = c(v - w) + \nabla^2 w \end{cases} \quad (3.24)$$

which is defined for some time interval  $(0, T)$  and over a suitable domain  $\Omega \subset \mathbb{R}^m$ ,  $m = 2$  or  $3$ , so that the differential operators are  $\nabla = (\partial/\partial x_1, \dots, \partial/\partial x_m)$  and  $\nabla^2 = \sum_{i=1}^m \partial^2/\partial x_i^2$ , with  $m = 2$  or  $3$ . Afterwards, let us assume that  $V$  denotes some functional space relevant to (3.24), then a weak solution  $(u, v, w) \in V \times V \times V$  is a triplet of functions that satisfies, for all test functions  $(g_1, g_2, g_3) \in V \times V \times V$ ,

the following system

$$\begin{cases} \int_{\Omega} \left( \frac{\partial u}{\partial t} g_1 - u(1-u)g_1 + duwg_1 \right) d\mathbf{x} = 0 \\ \int_{\Omega} \left( \frac{\partial v}{\partial t} g_2 - rv(1-v)g_2 + D(1-u)\nabla v \cdot \nabla g_2 \right) d\mathbf{x} = 0 \\ \int_{\Omega} \left( \frac{\partial w}{\partial t} g_3 - c(v-w)g_3 + \nabla w \cdot \nabla g_3 \right) d\mathbf{x} = 0 \end{cases} \quad (3.25)$$

and the homogeneous Neumann boundary conditions are directly built into (3.25).

The above mentioned weak formulation of system (3.24) is needed to establish the mathematical context for performing simulations by using the COMSOL Multiphysics environment [108].

### 3.6.1 Two-dimensional experiments

The first important step is certainly trying to reproduce the two different kinds of tumour invasion previously described in Section 3.4. As concerns the domain, we consider the 2-ball of radius  $R$  centered at the point  $C$ , namely  $\Omega = \overline{B_R(C)}$ , such a choice for the geometry being inspired by the circular *Petri dish* widely employed in biology for cell cultures (see Figure 3.18). For instance, we have taken  $R = 8$  and  $C = (0, 0)$  as simulation parameters.



Figure 3.18. Sample of a circular *Petri dish* for cell cultures.

For the initial profiles, we assume the evolution of a cancerous peak located in the neighborhood of the origin and a complementary shape for the healthy cells density (see Figure 3.19), while the extracellular lactic acid concentration is initially assumed equal to zero. For  $\mathbf{x} \in \Omega$ , the corresponding functions are

$$u(\mathbf{x}, 0) = 1 - \frac{\exp(-\|\mathbf{x}\|^2)}{\sqrt{\pi}}, \quad v(\mathbf{x}, 0) = \frac{\exp(-\|\mathbf{x}\|^2)}{\sqrt{\pi}}, \quad w(\mathbf{x}, 0) = 0. \quad (3.26)$$

Numerical simulations have been performed until  $T = 13$  and the time instant  $T = 6$  has been selected for checking the progress of plots also at an intermediate stage. The other simulation parameters are summarized in Table 3.1.

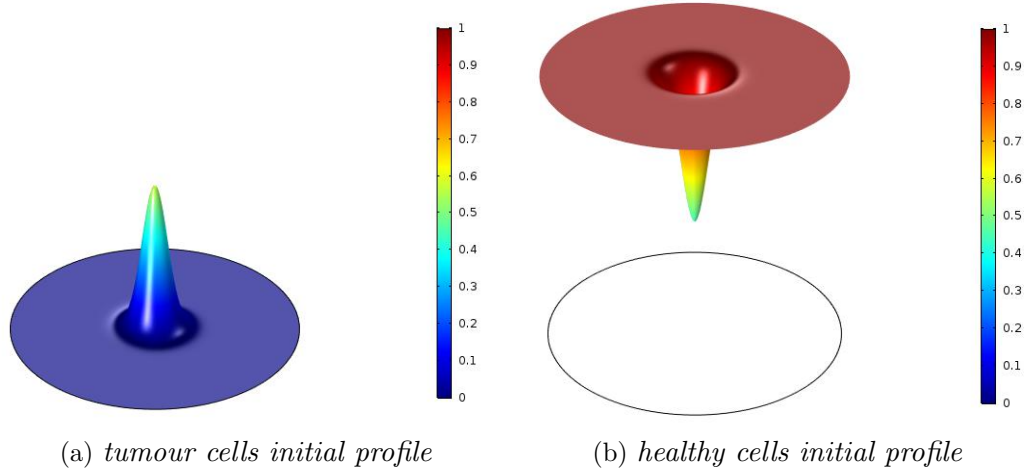


Figure 3.19. Plots of the initial profiles for tumour and healthy cells densities.

From now on, we decide to omit graphic information about the lactic acid concentration, having again recognized a persistent similarity with the behaviour of the tumour cells density (refer also to Figure 3.4).

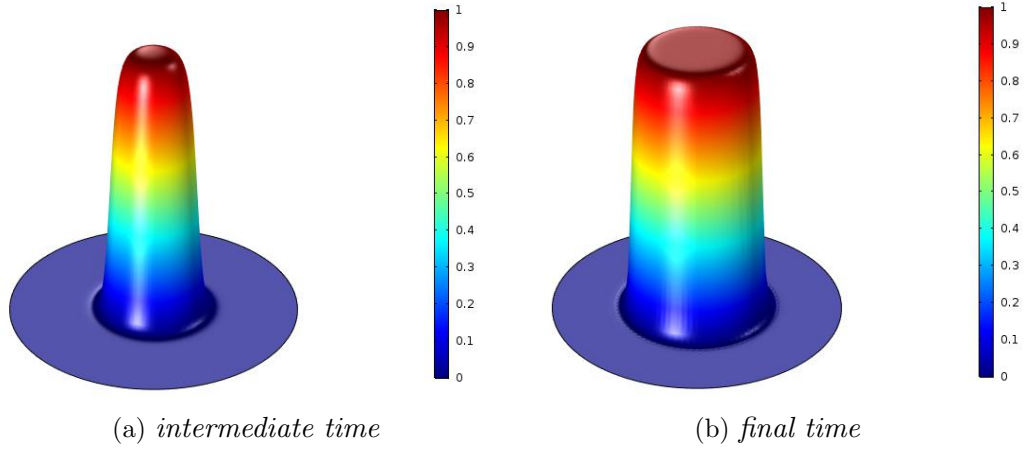


Figure 3.20. The homogeneous invasion: tumour cells density evolution at two different time instants  $T=6$  (a) and  $T=13$  (b).

The homogeneous invasion, which is expected to characterize the solutions to system (3.24) for  $d > 1$ , is the first case to be examined: Figure 3.20 and Figure 3.21 depict the related trends for tumour and healthy cells densities, respectively.

Starting from the graphs at the intermediate time instant, reported in Fig-

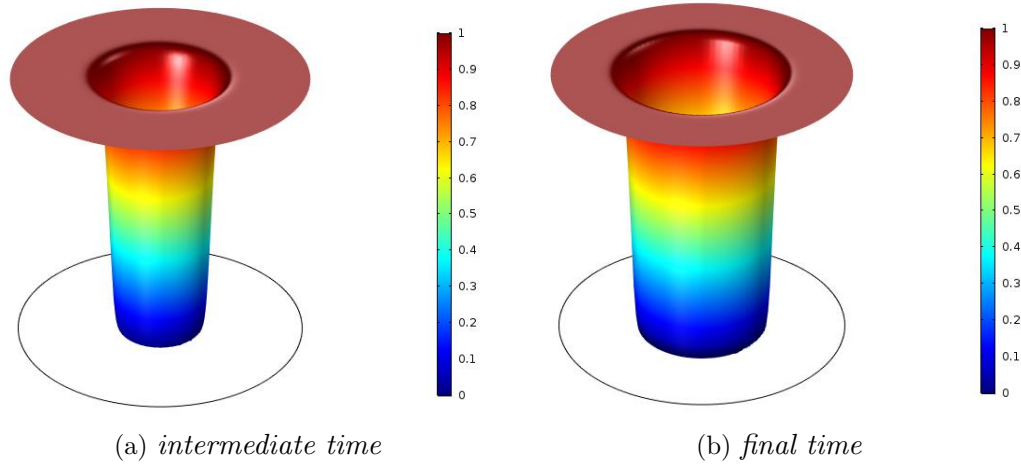


Figure 3.21. The homogeneous invasion: healthy cells density evolution at two different time instants  $T=6$  (a) and  $T=13$  (b).

ure 3.20(a) and Figure 3.21(a), the qualitative dynamics shows clearly the initial cancerous peak growing and spreading out at the expense of the local healthy tissue. Then, the tumour invasion gradually extends towards the outermost

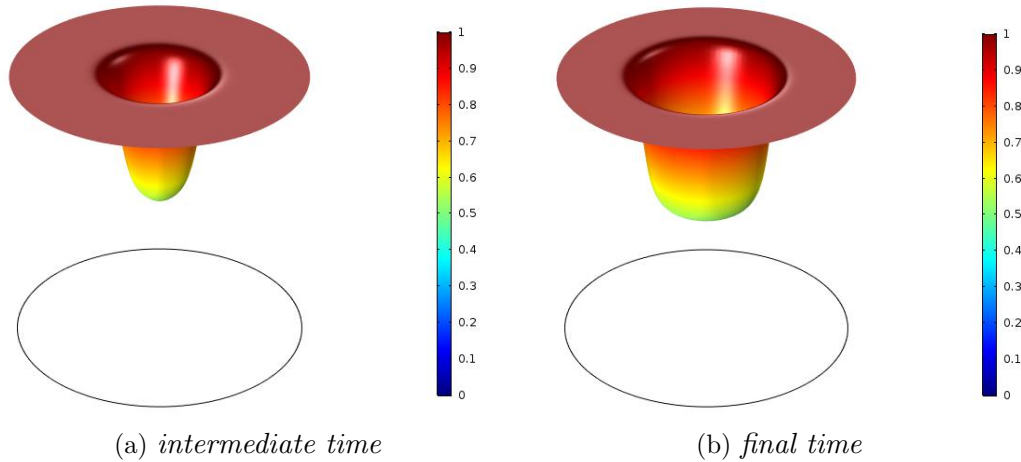


Figure 3.22. The heterogeneous invasion: healthy cells density evolution at two different time instants  $T=6$  (a) and  $T=13$  (b).

regions of the domain (see Figure 3.20(b)), where the healthy cells density is finally being confined (see Figure 3.21(b)). It is therefore confirmed that the homogeneous invasion is the most aggressive situation, due to the complete annihilation of healthy cells behind the advancing radially headed cancerous core.

As concerns the case of heterogeneous invasion, namely for  $d < 1$  into (3.24), we focus on the healthy cells density evolution (see Figure 3.22) but omit reporting plots related to the cancerous peak spreading, which turns out to be very similar to the counterpart in Figure 3.20 for the homogeneous configuration. As a matter of fact, it is possible to infer that the local healthy tissue is not being completely repulsed by the tumour, in contrast to what observed in Figure 3.21 because healthy cells are destroyed through the strong effect of the lactic acid concentration. Figure 3.22 shows instead that the healthy cells density reaches an asymptotic threshold within the inner region of the experimental domain, where the cancerous core is already detectable.

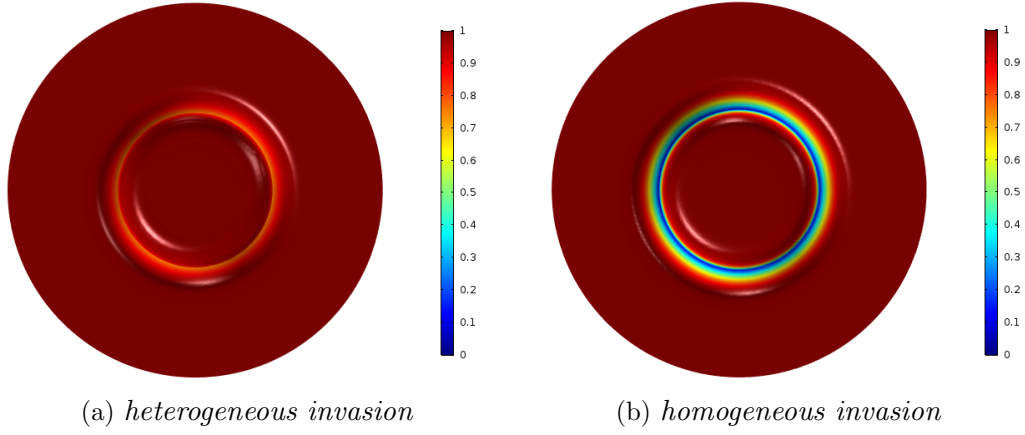


Figure 3.23. Identification of the two-dimensional *gap* formation for the homogeneous case (b) with respect to the heterogeneous case (a).

On the heels of the results available in the one-dimensional framework (refer to Section 3.4), the essential qualitative difference arising when comparing the two kinds of tumour invasion lies in the coexistence of healthy and cancer cells on one side (heterogeneous invasion), and the annihilation of the local healthy tissue out of the cancerous core on the other side (homogeneous invasion). However, there is something more to be evaluated: in the homogeneous case, we have appreciated that there is not intersection between healthy and tumour cells densities, as shown in Figure 3.4(b). Specifically, we have recognized the existence of a spatial interstitial *gap*, and we aim at detecting an analogous phenomenon within the two-dimensional context as well. To accomplish this assignment, the healthy and tumour cells densities have been plotted simultaneously and a bird-eye viewpoint is required to investigate the circular crown placed between the advancing tumour front and the retiring healthy tissue (see Figure 3.23). On the one hand, it is possible to appreciate the *gap* formation around the cancerous peak for the homo-

geneous invasion, as exhibited in Figure 3.23(b): a smaller blue ring, corresponding to a null density zone, is recognizable within the circular crown located between the fronts, confirming that no intersection is allowed in this aggressive regime. On the other hand, for the heterogeneous invasion, Figure 3.23(a) shows that healthy and tumour cells densities are actually conflated in the area lying between the fronts.

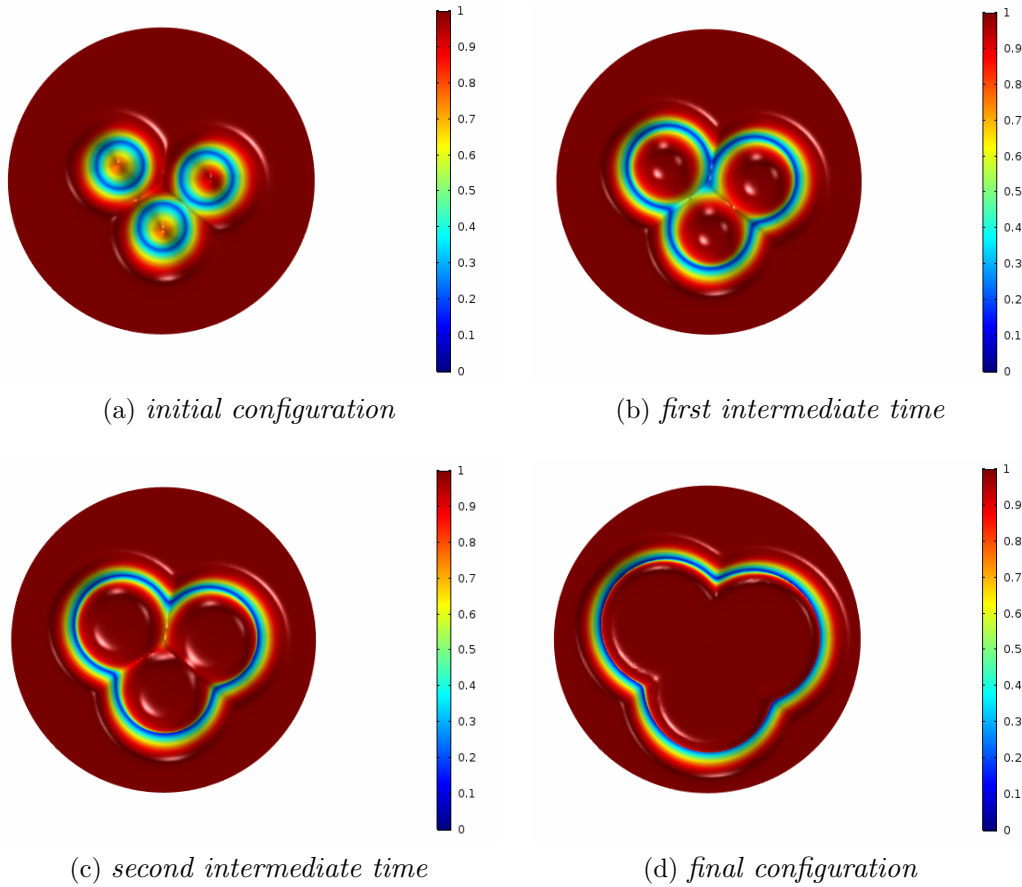


Figure 3.24. The homogeneous invasion: formation and evolution of a two-dimensional *gap* from three initially distinct cancerous peaks.

Finally, in order to further investigate the *gap* formation for the case of homogeneous invasion, we build a more complex configuration for the initial profiles made of three distinct cancerous peaks, by suitably rearranging the formulation (3.26). We report in Figure 3.24 the simultaneous plots of healthy and tumour cells densities at different time instants, by adopting the bird-eye viewpoint. We skip over the details concerning the single densities and we exploit Figure 3.24 both for analyzing the *gap* evolution and for qualitatively interpreting the resultant dynamics



of the fronts. In Figure 3.24(a), we notice the formation of three blue rings characterized by null densities around the cancerous circular crowns; then, by means of two intermediate evaluations (see Figures 3.24(b) and 3.24(c)), it is shown how these rings gradually increase their size and are opening, as the corresponding cancerous peaks are colliding and going into meltdown; eventually, once the novel tumour core is well-defined, as exhibited in Figure 3.24(d), the resultant *gap* consists of a single contour cordoning off the cancerous crown from the surrounding marginal area, where the local healthy tissue is regressing.

We conclude this section by remarking that, despite the triangular arrangement of the finite element meshes (see Figure 3.17(a)), the structure of radially symmetric solutions is preserved by the model dynamics: such property is indeed intrinsic to system (3.24), for which it can be proven analytically, and numerical evidence also emerges from the simulation results in Figure 3.20 and Figure 3.21, for example. Moreover, Figure 3.24 constitutes an experimental proof of the tendency to recover radially symmetric structures even starting from different initial configurations.

### 3.6.2 Three-dimensional experiments

The next step consists in exploring the three-dimensional framework, and we focus on the homogeneous invasion, in order to investigate the phenomenon of the spatial interstitial *gap* and its geometry. The COMSOL Multiphysics environment is still the principal resource for performing simulations, and we rely on ParaView [109] for post-processing graphical results.

By analogy with the two-dimensional experiments, the 3-ball of radius  $R$  centered at the point  $C$  is chosen as simulation domain, and we build the corresponding finite element mesh as shown in Figure 3.17(b) for the volume  $\Omega = \overline{B_R(C)}$  with  $R = 3.5$  and  $C = (0, 0, 0)$ , for instance. The three-dimensional version of the initial profiles given in (3.26) is also considered, and  $T = 7$  is assumed as final time instant. All the plots are realized by exploiting a graphical *heat map* and setting the color palette ranging from blue to red, as the magnitudes go from the lower values to the higher ones.

As concerns the qualitative evolution, the resulting dynamics displays the cancerous peak spreading out at the expense of the local healthy tissue, that is what we have expected on the ground of the results previously described for the two-dimensional framework (refer to Section 3.6.1). Figure 3.25(a) shows the cancer cells initial profile, while Figure 3.25(b) reports the evaluation at an intermediate time instant  $T = 4$ . By means of a transparency technique, that allows to appreciate the numerical data distribution throughout the three-dimensional volume, the tumour growth is suitably emphasized. The final configuration for both



healthy and cancer cells densities is depicted in Figure 3.26(a) and Figure 3.26(b), respectively.

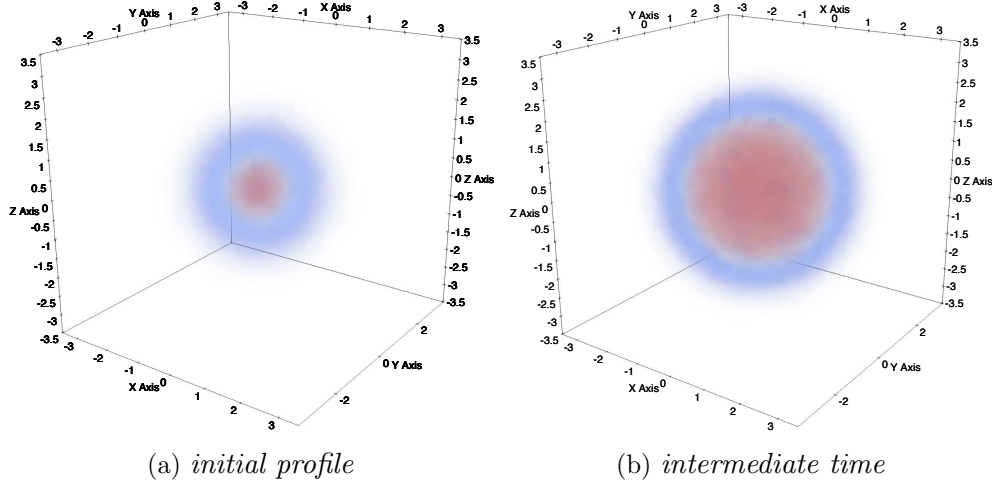


Figure 3.25. Tumour cells density evolution from the initial profile (a) towards an intermediate stage  $T=4$  (b).

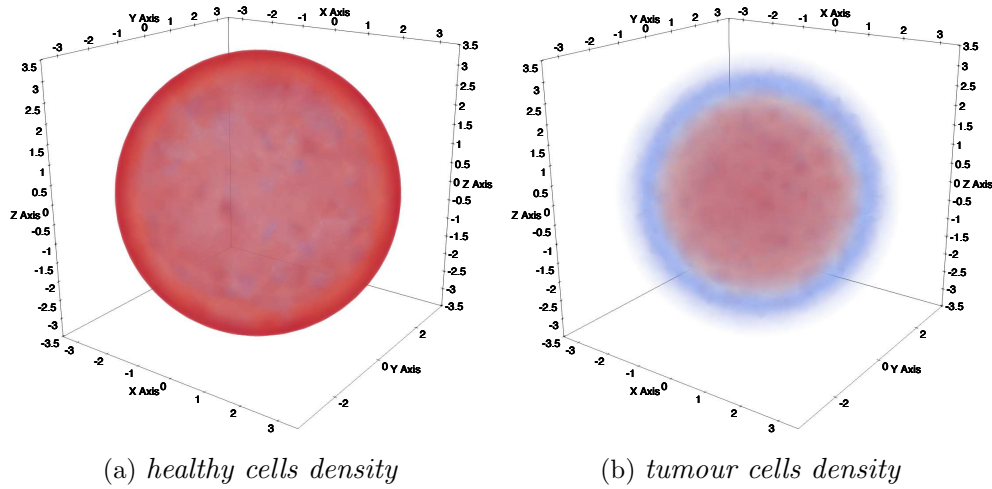


Figure 3.26. Healthy and tumour cells densities evaluation at final time  $T=7$ .

For collecting information about the *gap* formation and understanding how the densities are actually distributed within the experimental domain, let us have a look inside the volumes plotted in Figure 3.26. We cut the domain by means of a section plan passing through the origin and exploit the radial symmetry of

the solutions to system (3.25) to state that any other section plan would produce similar results.

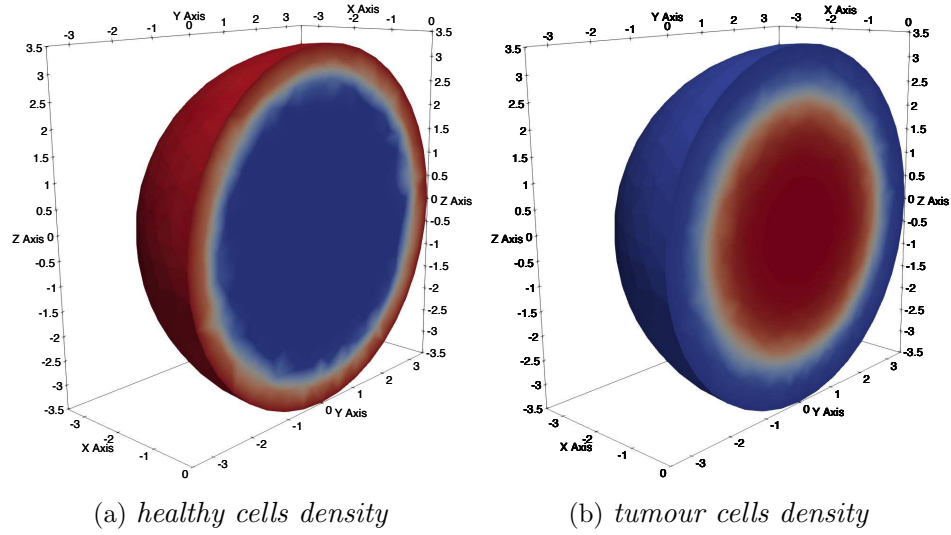


Figure 3.27. The half balls arising from domain sectioning and provided with numerical data throughout the external spherical surface.

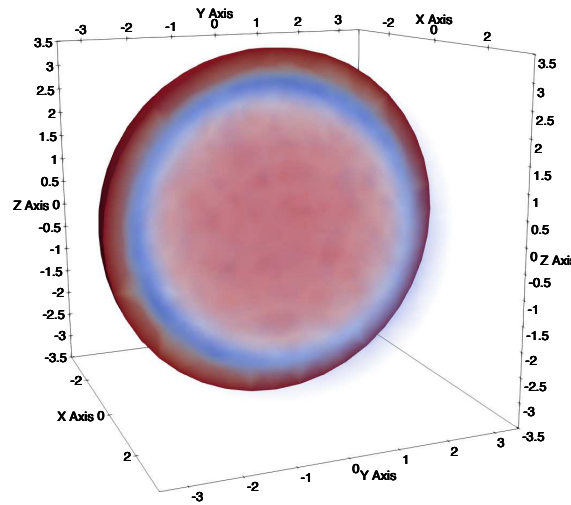


Figure 3.28. Three-dimensional tumour cells density profile located inside the half ball provided with healthy cells density data reproduced throughout the external spherical surface.

We report in Figure 3.27 the graphs corresponding to the half ball for both healthy and tumour cells densities, where the numerical data under examination

are represented on the external spherical surface only. This choice provides us with a clearer viewpoint to better detect the inner regions characterized by different density distributions. Indeed, taking advantage of symmetry arguments, we can easily infer that data distributions arising from surface representation retain an analogous behaviour inside any inner layer. Moreover, the healthy cells density is identically null throughout a ball contained inside the domain (see Figure 3.27(a)), while the innermost cancerous core reveals itself in bright red (see Figure 3.27(b)).

As a matter of fact, Figure 3.27 turns out to be a sort of *graphical proof* for assessing the presence of a separation zone between the healthy and cancer cells densities, preventing them from being in touch as the evolution is going on. Therefore, available space emerges to include the tumour cell density without producing intersection, as it has been already observed for the one-dimensional and the two-dimensional framework (see Figure 3.4(d) and Figure 3.23(b), respectively).

On that account, Figure 3.28 shows a simultaneous plot consisting of numerical data merging from Figure 3.26(b) and Figure 3.27(a), where the cancerous core is placed in its corresponding spacial domain with respect to the half ball provided with the healthy cells density profile throughout the external spherical surface. At

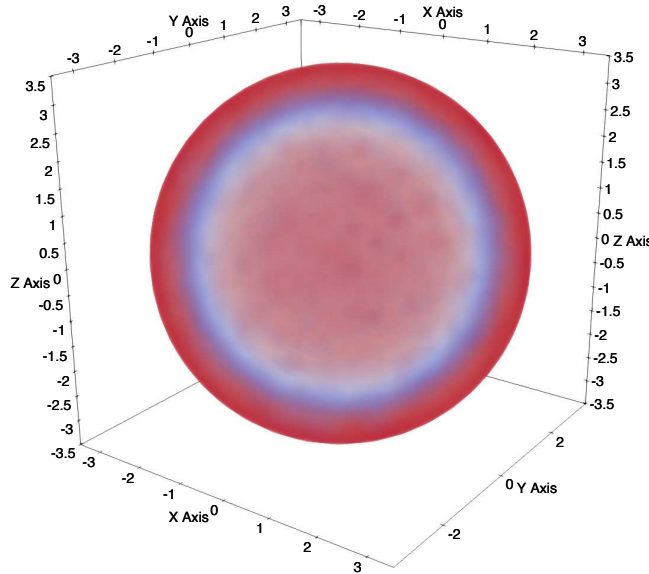


Figure 3.29. Detection of the three-dimensional spatial interstitial *gap* by means of the transparency technique.

this stage, identifying the three-dimensional version of the spatial interstitial *gap* becomes possible: we are dealing with a null density solid shell located between the healthy and tumour cells profiles, which is quite well recognizable in Figure 3.28. Finally, in order to provide the most effective three-dimensional representation of

the qualitative dynamics of the Gatenby-Gawlinski model (3.24), we have realized a meaningful simultaneous plot of Figure 3.26(a) and Figure 3.26(b) by exploiting the transparency technique, and the resulting graph is depicted in Figure 3.29, where the geometry of the spatial interstitial *gap* is now clearly noticeable.

# Chapter 4

## Study of the Burridge-Knopoff model<sup>1</sup>

### 4.1 Introduction

Earthquakes are doubtless an open research field. The need to improve our knowledge of this kind of geophysical mechanisms and related topics is very strong. Specifically, an earthquake occurs along fractures in the Earth's crust, named *faults*, characterized by a steady accumulation of tension, when big quantities of energy are suddenly released due to the relative motion of the two sides involved. To understand better we recall that Earth's lithosphere includes the crust and is also composed of a part of the upper mantle. Moreover, it presents a complex structure divided into distinct blocks, the *tectonic plates*. This point is crucial, because it is along the borders of tectonic plates that the great accumulation of tension we mentioned above takes place. The plates are indeed continually stressed by external forces, whose nature has been investigated and is continuing being object of study: scientists think this stress to be caused by the mantle convection [21] but a gravitational contribution is not ignored [22].

A central role in our analysis is played by the friction. Indeed, although the existence of forces able to solicit plates is of course an important factor to explain seismic events, nothing would happen if friction did not inhibit the relative motion between the two different sides of an active fault. Strongly connected with these concepts is the *stick-slip phenomenon*, associated to the earthquakes by Brace and Byerlee [13]. The borders of a fault exhibit asperities which make the local slip very difficult: as a consequence tension increases and the motion is inhibited by the balance between tension and friction. Once that this equilibrium is compromised, due to the steady accumulation of stress, a slip of the sides involved occur and a

---

<sup>1</sup>The contents are collected in [58].

great quantity of energy is released, generating an earthquake. The alternation between period of quiescence, in which tension increases, and phases in which tension is released along the fault, through the motion of the plates, is a typical example of the stick-slip behaviour.

It is important to notice that in the last decades a great effort has been made to investigate the statistical properties of earthquakes. This way of thinking is strongly connected with the idea of *self-organized criticality*, SOC, developed by Bak et al. [5] and its influence on seismic events [6]. By following this concept lots of natural phenomena are explainable in terms of criticality: these kinds of processes can self-organize and reach critical states. When similar states are reached, little perturbations affecting the elements belonging to the systems can propagate and involve items of any size [112]. In the SOC framework this behaviour is often illustrated by basic laws collecting the statistical properties of the process studied. As concerns the earthquakes, two important power laws would be a concrete manifestation of the SOC principles: the *Gutenberg-Richter law* [40] for the magnitude distributions and the *Omori law* for the aftershocks sequences [87]. In order to point out the SOC idea, the earthquake models are often analyzed with cellular automaton approach, as in the work by Olami, Feder and Christensen [6, 74].

One of the most famous mathematical models developed to study earthquakes and its statistical properties, especially pursuing the idea of a qualitative comparison with real phenomena, is the *Burridge-Knopoff model*, proposed in 1967 [14]. This is a deterministic dynamical system whose computational investigation provides lots of useful results to achieve a sufficiently accurate analysis of seismic events. The Burridge-Knopoff model has been deeply investigated in order to pursue a statistical study of earthquakes [45] and continues to be a landmark in this research field, due to its nontriviality but, at the same time, its simplicity [21]. On a mathematical level the associated differential system exhibits a discontinuous right hand side, arising from the choice of the friction law. This is a direct consequence of the alternation caused by the stick-slip dynamics and expressed by the friction, the only source of nonlinearity in the model. This alternation produces a dry friction. Lots of models arising from applications exhibit similar characteristics and require careful analysis. An analytical study of a non-smooth friction-oscillator model, qualitatively very close to the Burridge-Knopoff model, is provided in [48]. Obviously also the related numerical problem must be adequately approached: in this sense some numerical methods are employed for non-smooth systems [1] and suitable regularizations are often performed [39].

In this work we want to investigate the model in order to prove the almost convergence [8, 54] of wave speeds: we proceed as in the context of traveling waves theory, specifically, by numerically recognizing the existence of an asymptotic threshold. Indeed, the Burridge-Knopoff model has been proved to exhibit

features related to propagating fronts: some results have been achieved in [71], by means of a continuum version of the model, while in [65], the existence of solitary waves in the excitable Burridge-Knopoff model is reported. With the aim of achieving our main purpose, we develop a space-averaged wave speed estimate and perform simulations by employing a numerical adjustment of the system based on a Predictor-Corrector approach. The idea behind a Predictor-Corrector strategy [77] is inspired by the necessity of furnishing a good initial guess to start fixed-point iterations when an implicit method is invoked. Indeed, because several function evaluations are generally needed by using the fixed-point method, trying to reduce the computational cost becomes important. So the basic idea consists in using an explicit multistep method to compute a better initial guess and take advantage of this value by employing an implicit multistep method within a fixed-point scheme. The procedure is then divided into two parts: the first one is the prediction phase, where an explicit algorithm, named *Predictor*, furnishes an adequate initial guess; the second one is the correction phase, where an implicit algorithm is invoked, possibly also several times, to realize the fixed-point scheme. The implicit method used is defined the *Corrector* because acts on the predicted initial value. However, it is important to notice that the overall strategy is totally explicit because the predicted value is employed within the implicit method where the dependence on the incoming time instant appears.

The contents of the chapter are organized as follows. In Section 4.2 we introduce the model and describe a particular version among those available as developments of the original one proposed by Burridge and Knopoff, mentioning the important connection with the Gutenberg-Richter law. In Section 4.3 we present the numerical algorithm and analyze the computational strategy used; also we comment on the results of simulations by starting from the simplest case in order to increase the complexity and consider more articulated configurations. In Section 4.4 we perform simulations aimed at detecting the almost convergence of wave speeds, by means of a suitable wave speed estimate, to get information about traveling fronts: we numerically prove the existence of an asymptotic threshold and discuss a phenomenological explanation concerning the convergence of the wave speeds averages.

## 4.2 The Burridge-Knopoff model

The system studied by Burridge and Knopoff is a spring-block model. Their purpose consists in trying to reproduce the typical dynamics which take place along an active fault. The goal is pursued through a discrete representation given by a chain of  $N$  identical blocks, with mass  $m$ , mutually connected by linear springs with elastic constant  $k_c$ . A sort of one-dimensional array is generated

(Figure 4.1). It is also possible studying the dynamics produced by a grid of blocks, within a multidimensional version of the system, thus focusing on a two-dimensional array [67, 68]. The blocks are supposed to rest on a rough surface,

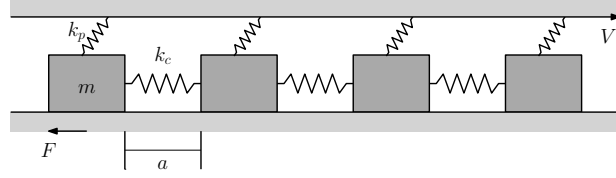


Figure 4.1. Scheme of the Burridge-Knopoff model.

where  $F$  is the friction, and connect to a moving upper plate by linear springs with elastic constant  $k_p$ . As regards the approximation of a real fault, the opposite sides of two different tectonic plates are assumed to be represented by the rough surface and the chain of blocks. The upper surface is supposed to be in motion, precisely at constant velocity  $V$ : this contribution induces a solicitation explainable thinking about the role of the external forces acting on a fault. It is assumed that the blocks are initially equally spaced and that the reciprocal distance is  $a$ . This means that  $a$  does not explicitly appear within the equation of motion for the block  $i$ , which is

$$m\ddot{x}_i = k_c(x_{i+1} - 2x_i + x_{i-1}) + k_p(Vt - x_i) - F(\dot{x}_i), \quad (4.1)$$

where  $x_i$  is the displacement from the initial equilibrium position. Let us investigate the structure of (4.1) by analyzing each contribution.

**Internal elastic energy** As concerns the horizontal springs, it is assumed that a linear interaction takes place among the blocks. This is the conventional adjustment adopted within the Burridge-Knopoff model, but a linear coupling is not the only possibility. For instance, the eventuality of a nonlinear coupling is considered in [19]. Due to the chain structure, producing two neighbors for each block, the internal elastic solicitation consists of two contributions, obviously except for the masses at the edges (in this case adequate boundary conditions are required as we will discuss in Section 4.3). By considering the elastic forces and recalling that the expression  $x_i$  is associated to the displacements from equilibrium position, the contribution provided by springs with stiffness  $k_c$  takes the form of the one-dimensional discrete Laplace operator.

**External forces** We said above that the action of the external forces is realized within the model by the upper surface, in motion with constant velocity  $V$ . The blocks deal with this external element through the springs with stiffness  $k_p$ . So each mass is affected by another elastic solicitation besides that produced by the



horizontal coupling. Of course, to quantify the vertical elastic force, it is necessary taking into account the elongation of springs caused by the upper plate. This consideration simply justifies the presence of the product  $Vt$ . It just has to combine this quantity with  $x_i$  and  $k_p$  according to the linear elasticity as in (4.1).

**Friction** The friction force  $F(\dot{x}_i)$  is velocity-dependent. This law allows to reproduce the typical stick-slip behaviour and introduces an essential instability inside the model. It is possible to distinguish different forms of friction, for instance, the Dieterich-Ruina friction law [24, 25, 80, 88], the Coulomb friction law used by Muratov in [71] or the velocity-weakening friction proposed by Carlson and Langer [15, 16, 17]. We adopt this last point of view henceforth. It is important to point out that another choice can be made between two different qualitative behaviours, the so-called asymmetric and symmetric versions, whose main difference is the constraint of non-negative velocity assumed in the asymmetric version. This means that back slip is inhibited for each block. We assume this constraint according to [17, 49, 66, 69, 81, 101] and adopt the following (multi-valued) functional form

$$F(v) = \begin{cases} \frac{F_0(1-\sigma)}{1 + \frac{2\alpha v}{1-\sigma}} & \text{if } v > 0 \\ (-\infty, F_0] & \text{if } v \leq 0, \end{cases}$$

where  $v = \dot{x}_i$ . This double structure is easily understandable because a law based on the stick-slip dynamics must exhibit a discontinuity, as a consequence of the alternation between sticking and sliding motion for each block. The back sliding motion is forbidden by formally imposing  $F(v) = -\infty$  for  $v < 0$ . The value  $F_0$  corresponds to the maximum static frictional force, so the static friction formally may range in the interval  $(-\infty, F_0]$ . During a sticking period the elastic resultant force acting on a block is perfectly balanced by the static friction, which means no motion: in this case the equation (4.1) simply becomes  $m\ddot{x}_i = 0$  with initial zero velocity. When the resultant force exceeds the threshold  $F_0$ , a slipping period starts with dynamic friction. Friction becomes weaker now, it decays monotonically to zero, as the velocity increases (see Figure 4.2). Another important feature of the friction law is the role of the parameters  $\sigma$  and  $\alpha$ . The first one quantifies a small drop of the friction at the end of a sticking period; the second one provides information about the decreasing of the dynamic friction force in relation to the increasing of the sliding velocity.

One of the most interesting features of the Burridge-Knopoff model consists in the reproducibility of some important properties related to complex phenomena as real earthquakes, although the system exhibits a relatively simple structure. Among these typical behaviours, the *Gutenberg-Richter law* plays a significant role and can be used as a powerful instrument to assess the reliability of the model.

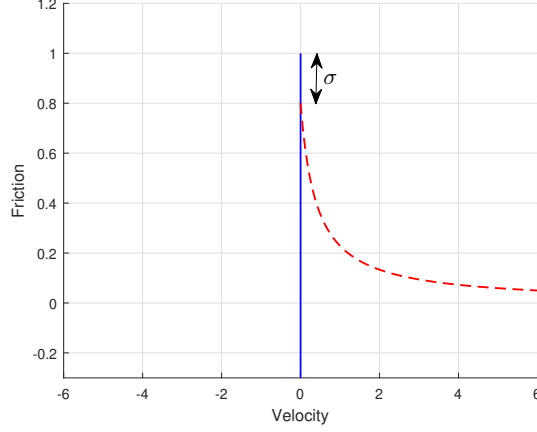


Figure 4.2. The form of the friction law: the solid line is referred to the sticking friction, the dash one, to the slipping friction.  $F_0$  is assumed to be unity. As samples for the plot,  $\sigma = 0.2$  and  $\alpha = 1$  are considered.

This power law establishes that, in a seismic zone, the relationship between the number  $N$  of earthquakes with intensity greater than or equal to a given magnitude  $M$  and the magnitude itself has the form

$$\log_{10} N = a - bM, \quad (4.2)$$

for some parameters  $a$  and  $b$ . In order to represent the rate of seismic events, by introducing the total number of events expressed as  $N_T = 10^a$ , it is possible to reformulate the relationship (4.2) as

$$\log_{10}(N/N_T) = -bM. \quad (4.3)$$

This substitution allows us to understand the meaning of the quantity  $a$  in terms of total seismicity rate of an active zone. Finally, as regards the parameter  $b$ , in real situations its values are usually very close to 1 in seismic zones [21].

It would be very interesting to make comparisons also within the aftershocks field, by studying the *Omori law*. However, at least in a such simple version of the Burridge-Knopoff model as the current one, it is impossible recognizing aftershocks sequences, as pointed out in [21, 45]. Further contributions, as viscosity, would be required.

### 4.3 Numerical algorithm and its reliability

To start with, we discuss the computational strategy adopted and the numerical algorithm chosen. Once the number of blocks  $N$  is established, it is possible to

obtain a differential system composed of equations like (4.1), namely

$$\begin{cases} \dot{x}_i = y_i \\ m\dot{y}_i = k_c(x_{i+1} - 2x_i + x_{i-1}) + k_p(Vt - x_i) - F(y_i), \end{cases}$$

for  $i = 1, \dots, N$ , where we assume that  $x_0 = x_1$  and  $x_{N+1} = x_N$  for the boundary conditions [14].

**Initial conditions** Following [102], in order to avoid a periodic evolution and with the aim of reproducing realistic local tension along a fault, we assign small random displacements from the equilibrium positions for each mass. The blocks are supposed to be at rest, so we put zero velocities. Remembering that the blocks are initially equally spaced with distance  $a$ , the equilibrium positions are  $P_i = a(i - 1)$  for  $i = 1, \dots, N$ . Because zero velocities are imposed, all blocks are initially stuck. However, if a simulation would have started with the actual initial conditions, some irregular dynamical motion would be recognized, due to the action of spring and friction forces. On the contrary, we wish to appreciate a realistic charge cycle, that is why we identify the next incoming time of global stick,  $\bar{t}$ , and select this one as initial time. This implies that the original initial conditions, and corresponding perturbations, must be updated in  $\bar{t}$ : the simulation is now ready to be restarted by setting  $t = 0$ .

**Stick-slip detection** To identify a time of stick for a block within the numerical code, we use a criterion based on both the resultant force and velocities: a block is stuck if and only if the elastic resultant force is less than the maximum static frictional force and the velocity is equal to zero. Obviously, it is very difficult detecting an absolutely zero velocity in simulations so that we use a workaround: because back slip is inhibited, sign changes of the velocity are interpreted as the tendency of being stuck, so negative values are suppressed and replaced by zero values. That is why we do not need to introduce a threshold parameter to create a range for the zero value as it is often done working with the asymmetric friction law.

**Seismic events** Talking about the statistical properties of the model, specifically referred to the Gutenberg-Richter law, we have to assume an operative definition to judge whether a seismic event is happening: an earthquake occurs when a blocks starts to slip and ends only where all the blocks are stuck again. This definition implies that, during an event, a block can slip and become stuck alternately; moreover, the elastic coupling produces a sort of propagation along the chain of masses, because a block can trigger the slipping of its neighbors. In order to

quantify the magnitude of an earthquake, we introduce the following definition for the magnitude  $M$ :

$$M = \log_{10} \left( \sum_{i=1}^N \Delta x_i \right), \quad (4.4)$$

where  $\Delta x_i$  is the cumulative displacement of the block  $i$  during a given earthquake.

### 4.3.1 Numerical adjustment

As regards the numerical integration of the Burridge-Knopoff model with velocity-weakening friction, various methodologies have been employed by using either explicit methods, such as explicit Runge-Kutta [66, 67, 68, 69, 101], or implicit methods, such as Implicit Euler [102].

We adopt a Predictor-Corrector strategy [77] and here, for reader's convenience, we recall the basic procedure. First of all we start by considering a general implicit multistep method, for instance, by selecting the Adams-Moulton methods from the Adams Family. The following equation groups all the Adams methods,

$$y_{n+1} = y_n + h \sum_{j=-1}^p b_j f_{n-j}. \quad (4.5)$$

If  $b_{-1} \neq 0$ , an implicit method, named Adams-Moulton, is generated; otherwise, when  $b_{-1} = 0$ , an explicit method, named Adams-Bashforth, is obtained. That is why we assume  $b_{-1} \neq 0$ . In (4.5)  $y_n$  indicates the approximate solution evaluated at time  $t_n$ ; the symbol  $f_{n-j}$ , corresponding to  $f(t_{n-j}, y_{n-j})$ , is the vector field;  $h$  is the step size;  $b_j \in \mathbb{R}$ ;  $p \in \mathbb{N}$  is used to quantify the number of steps of the method, precisely  $p + 1$ , without including the implicit part associated to  $j = -1$ . We recall that the Adams methods are derived from the integral representation of the Cauchy's problem for a given differential system, namely

$$x(t) = x_o + \int_{t_0}^t f(s, x(s)) ds,$$

by using interpolating polynomials in the Lagrange form to approximate the vector field. In order to solve a Cauchy's problem by using an implicit method such as (4.5) it is necessary to approach a nonlinear equation. We can rewrite (4.5) as follows

$$y_{n+1} = y_n + h \sum_{j=-1}^p b_j f_{n-j} = \Phi(y_{n+1}). \quad (4.6)$$

By taking advantage of (4.6) we can adopt fixed-point iterations and thus solve the nonlinear equation. For  $k = 0, 1, \dots$ , we get

$$y_{n+1}^{(k+1)} = \Phi(y_{n+1}^{(k)}). \quad (4.7)$$

However the procedure triggered by (4.7) requires several function evaluations to achieve convergence, due to the iterations needed. The idea behind a Predictor-Corrector strategy, which is inspired by the purpose of reducing the computational cost, is to compute a good initial guess for the fixed-point iterations by recalling an explicit multistep method. This method, called *Predictor*, provides an adequate guess to be used within the fixed-point scheme (4.7) generated by the implicit algorithm (4.5). The implicit method, named *Corrector*, can be invoked  $m$  times, with  $m \geq 1$ . When  $m > 1$  the procedure is called *Predictor-Multicorrector*. In this work we choose  $m = 1$ , so we will continue using simply the wording Predictor-Corrector. The algorithm produced by starting from the Adams methods can be summed up as follows

$$\left\{ \begin{array}{l} \text{Predict: } y_{n+1}^{(0)} = y_n^{(1)} + h \sum_{j=0}^{\bar{p}} \bar{b}_j f_{n-j}^{(0)} \\ \text{Evaluate: } f_{n+1}^{(0)} = f(t_{n+1}, y_{n+1}^{(0)}) \\ \text{Correct: } y_{n+1}^{(1)} = y_n^{(1)} + hb_{-1}f_{n+1}^{(0)} + h \sum_{j=0}^p b_j f_{n-j}^{(0)}, \end{array} \right.$$

where the *Evaluation step* of the vector field  $f$  is included. The superscript (0) denotes the guess provided by the Predictor, the superscript (1), instead, indicates the values furnished by the Corrector. The abbreviation usually employed for the overall procedure is *PEC*. We notice that a Predictor-Corrector strategy, also in the general case  $m \geq 1$ , is by construction totally explicit. As regards our numerical adjustment, we adopt the Predictor-Corrector technique in a bit different form, called *PECE*, in which a further evaluation of  $f$  is performed at the end of the sequence. Moreover, the second-order Adams-Bashforth scheme (AB2) is used as Predictor, while the third-order Adams-Moulton method (AM3) is chosen as Corrector. We thus obtain

$$\left\{ \begin{array}{l} \text{Predict: } y_{n+1}^{(0)} = y_n^{(1)} + \frac{h}{2}[3f_n^{(1)} - f_{n-1}^{(1)}] \\ \text{Evaluate: } f_{n+1}^{(0)} = f(t_{n+1}, y_{n+1}^{(0)}) \\ \text{Correct: } y_{n+1}^{(1)} = y_n^{(1)} + \frac{h}{12}[5f_{n+1}^{(0)} + 8f_n^{(1)} - f_{n-1}^{(1)}] \\ \text{Evaluate: } f_{n+1}^{(1)} = f(t_{n+1}, y_{n+1}^{(1)}). \end{array} \right.$$

We point out that the order,  $q$ , of the *PECE* procedure, can be computed as follows

$$q = \min(q_p + 1, q_c),$$

where  $q_p$  and  $q_c$  are the orders of the Predictor and the Corrector steps, respectively. Therefore, we have generated an overall third-order method.

Evaluating the pros and the cons of the Predictor-Corrector technique, the main advantages consist, firstly, in avoiding to solve an implicit system at every step, whose size would increase with the number of blocks, and, secondly, in ensuring a stronger stability when compared to standard explicit methods. On the other hand, we have to adopt a small time-step to achieve a good approximation of the solution to the Burridge-Knopoff model. According to [69, 101], we choose  $h = 0.001$  as constant step.

### 4.3.2 One block

As the simplest case, we examine the evolution of the system in which only one block is involved (see Figure 4.3). The aim is to become familiar with the specific

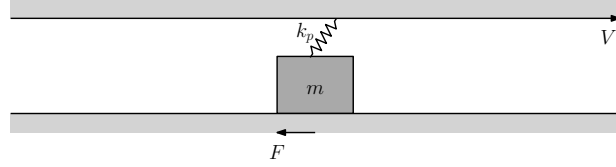


Figure 4.3. The system involving a single block

trend of the stick-slip dynamics. The equation of motion can be easily deduced from (4.1) by omitting the elastic term associated to the horizontal connecting springs, because in this configuration adjacent blocks are not included, so that we get

$$m\ddot{x} = k_p(Vt - x) - F(\dot{x}). \quad (4.8)$$

For the values of the parameters involved in the model, we adopt the list shown in Table 4.1, as in [81]. We deduce from this table all the values useful to in-

Table 4.1: Values of quantities involved in the simulations with one block.

Parameters				
$m$	$k_p$	$k_c$	$V$	$F_0$
1	1	60	0.001	1

tegrate (4.8). Finally, for the remaining parameters, we put  $\sigma = 0.01$  according to [66] and arbitrarily choose  $\alpha = 1$ . In the follow-up we will discuss carefully the role of the quantity  $\alpha$ , which is very significant within the configurations involving lots of blocks.

As initial conditions we simply impose  $x(0) = 0$  and  $\dot{x}(0) = 0$  without adopting artifices as those mentioned previously, very useful in the case of more blocks. It

is obviously possible to assume a more realistic small displacement for  $x(t)$  in  $t = 0$  but the evolution would not change its qualitative behaviour, the only difference consisting in the duration of the first stick period. When only one block is involved, indeed, the motion exhibits a periodic trend. In order to avoid this kind of dynamics, it is crucial introducing more blocks within the system. Figures 4.4 and 4.5 show the results in the case of a single block. In absence of

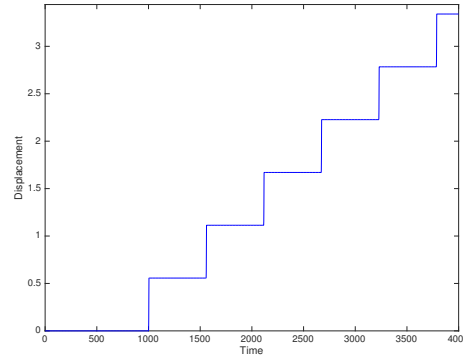
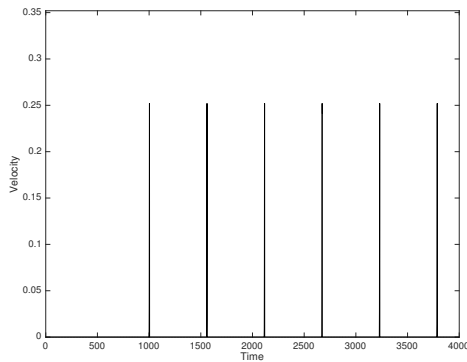
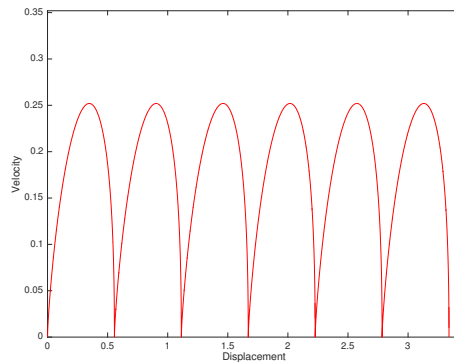


Figure 4.4. Displacement for a single block. All the values used to perform the simulation are available in Table 4.1.

adjacent masses, the motion tends to be periodic. We recognize the alternation between sticking and slipping periods from the qualitative behaviour of the graph in Figure 4.4: a steep trend characterizes the sliding motion, in opposition to the flat one produced when there is not motion. When the block is sliding, its velocity



(a) *velocity graph*



(b) *phase portrait*

Figure 4.5. Velocity and phase portrait for a single block. All the values used to perform the simulation are available in Table 4.1.

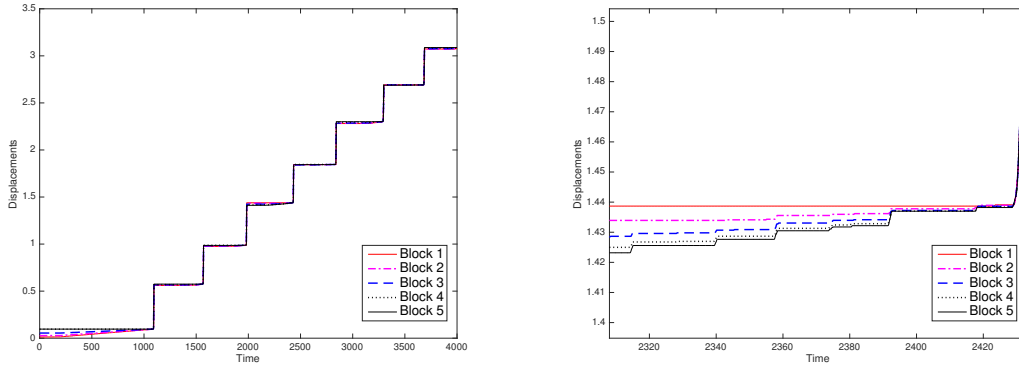
achieves some pronounced peaks as shown in Figure 4.5(a). In Figure 4.5(b) a qualitative summary is provided by the phase portrait. Although this kind of system is very far from being an accurate representation for seismic events, because lots of other contributions would be required, on a geophysical level we could think about a slipping period as an earthquake and a sticking one as a charge cycle.

### 4.3.3 A bit more complex configuration

We proceed to examine a model involving five masses. By adopting the same parameters used in the case of a single block, listed in Table 4.1, and assuming as initial conditions random, small displacements updated at the incoming time of global stick, as described before, we simulate the evolution. The associated differential system is defined by using (4.1) and paying attention to include the boundary conditions. For instance, the equation for the first block becomes

$$m\ddot{x}_1 = k_c(x_2 - x_1) + k_p(Vt - x_1) - F(\dot{x}_1).$$

In Figure 4.6(a) we plot the displacements of the blocks, while in Figure 4.6(b) a zoom-in for these trajectories is provided. It is possible to recognize some great slipping phases in which all the blocks are involved; on the other hand, talking about the flatter trends, very small displacements happen. The pronounced peaks correspond to the most powerful shocks allowed for such a limited configuration. Finally, looking carefully at the zoom-in Figure 4.6(b), a sequence of narrow events happening before one of the peaks mentioned above is captured: these small earthquakes can be interpreted as foreshocks. Although five blocks are not enough to



(a) *displacements as a function of time*

(b) *zoom-in of the previous graph*

Figure 4.6. A system involving five blocks. The graph of the displacements as a function of time and its zoom-in for the parameters listed in Table 4.1.



exhibit a satisfying dynamics, it has been helpful to investigate the results in a qualitative way. As can be observed, indeed, the behaviour is certainly more complex and nontrivial than in the case of a single block. In order to support this point of view, in Figure 4.7 we take one block as sample and plot the velocity and the phase portrait (trends are very similar for the remaining blocks). So more facets and details about the qualitative trend are pointed out.

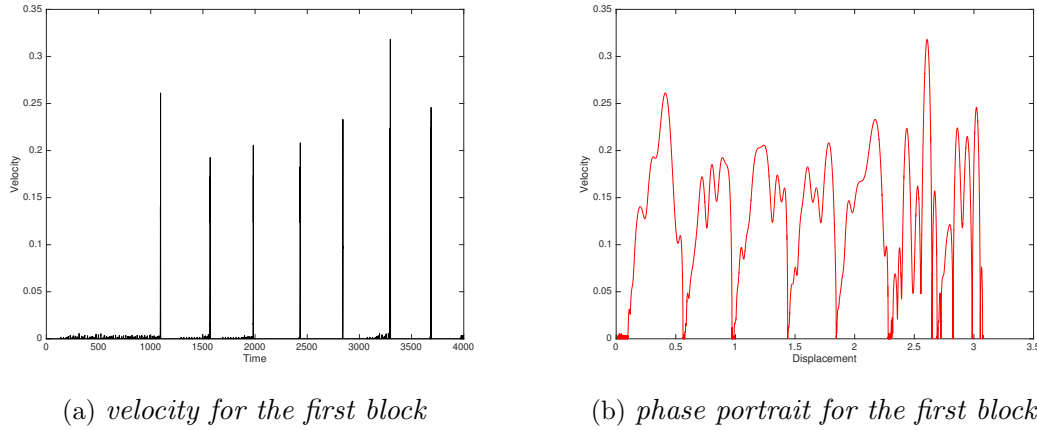


Figure 4.7. Block 1 has been taken as sample for the simulation including five blocks. The graph of velocity as a function of time and corresponding phase portrait are similar for the remaining blocks.

#### 4.3.4 More blocks and the Gutenberg-Richter law

The next steps in our analysis are aimed at arguing the reliability of the Burridge-Knopoff model using the Gutenberg-Richter law exhibited in (4.3). In order to achieve this purpose, we increase the number of blocks and consider a system including two hundred blocks, so  $N = 200$ . In Table 4.2 the parameters used in this last part of Section 4.3 are listed. We collect information about the seismic

Table 4.2: Values of quantities involved in the simulations with several blocks.

Parameters						
$m$	$k_p$	$k_c$	$V$	$F_0$	$\sigma$	$\alpha$
1	1	100	0.001	1	0.01	$\{1, 1.5, 2, 3, 4\}$

events generated by using the criterion described before to distinguish when an

earthquake is happening into the simulation. As regards the magnitude, the relationship (4.4) provides a quantitative definition. First of all, to discuss the results, it is absolutely necessary focusing on the role of the parameter  $\alpha$  introduced by the friction law [16, 49, 66, 101]. As said in Section 4.2,  $\alpha$  expresses the rate of slipping friction decreasing on increasing the sliding velocity. As a result, if  $\alpha$  decreases, friction becomes more dissipative; on the contrary, larger values of  $\alpha$  mean less dissipation because the slipping friction decreases more quickly with sliding velocity. On a quantitative level, the value  $\alpha = 1$  is an important threshold, since values of  $\alpha$  less than unity preventing system from exhibiting great earthquakes, that is why  $\alpha = 1$  is a sort of lower bound. Moreover, different behaviours are noticeable by assuming  $\alpha = 1$  and  $\alpha > 1$ : let us investigate this point. By following [102] we introduce the earthquake distribution  $P(M)$ , which is the ratio between the number of earthquakes greater than or equal to a given magnitude  $M$  (see (4.4)) and the total number of events  $N_T$ . Operatively we classify magnitudes by establishing the belonging to different ranges such as  $[M, M + dM]$ , where  $dM$  is fixed to be equal to 0.2. According to (4.3), we represent the distribution of earthquakes by the graph of the function  $M \mapsto \log_{10}[P(M)]$ . In the first case considered  $\alpha = 1$  is employed and the result is shown in Figure 4.8(a). By observing

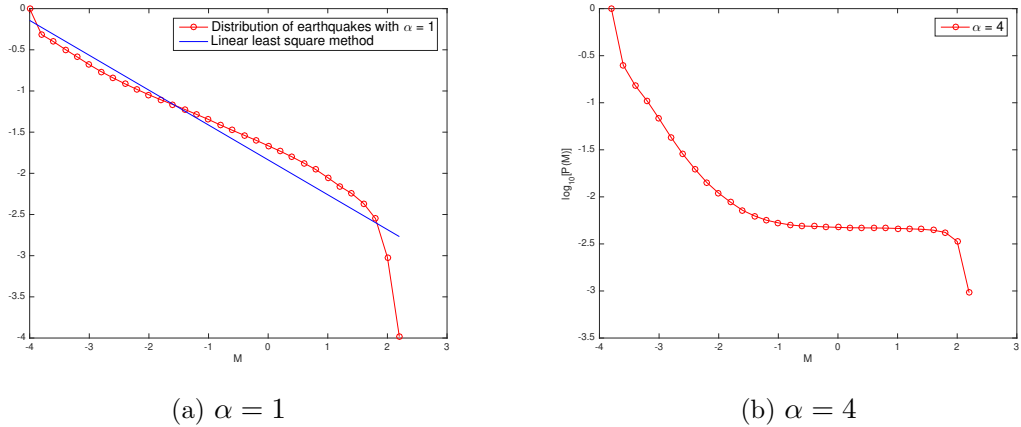


Figure 4.8. Earthquakes distribution for a system with 200 blocks: graph of the function  $M \mapsto \log_{10}[P(M)]$ . The simulations are realized by using the parameters listed in Table 4.2.

the graph, it is possible to recognize a behaviour very close to a straight line in the central part (between  $M = -3.7$  and  $M = 1.7$ , approximately), which can be interpreted coherently with the Gutenberg-Richter law. By adopting the linear least squares method (see Figure 4.8(a)) we estimate an exponent  $B \simeq 0.42$  for the power-law trend. We point out that the exponent derived from the simulations of

the Burridge-Knopoff model cannot be directly matched to the  $b$ -value appearing in the Gutenberg-Richter law (4.3), indeed a rescaling would be required in order to make a comparison with the real data [21, 45]. We can take as a reference the relationship  $b = \frac{3}{2}B$  described in [45]. Moreover, according to the results in [66], we notice that by varying the ratio between the stiffness of the springs,  $k_c/k_p$ , usually called  $l^2$  in the literature, a bit different exponent  $B$  is computed: the lower the ratio the higher the exponent, of course preserving the constraint  $k_c > k_p$ . For instance, by imposing  $l^2 = 36$  we find  $B \simeq 0.45$  or choosing  $l^2 = 9$  we obtain  $B \simeq 0.54$ . As regards the data providing the results plotted in Figure 4.8, a ratio  $l^2 = 100$  can be deduced from Table 4.2.

All these considerations make our  $b$ -value ranging in the interval  $[0.63, 0.81]$ , that means a bit flatter slope for the graph in Figure 4.8(a): indeed it is less than the empiric value  $b = 1$  in (4.3). Finding a flatter slope is consistent with other observations available in the literature, as in [17, 66, 102]. At very small magnitude we notice a steep linear segment in the graph, probably caused by the discreteness of the model [66, 102].

By increasing  $\alpha$ , a different qualitative behaviour is provided by simulations. For instance, we assume now  $\alpha = 4$  (see Figure 4.8(b)) in order to show the main differences, without neglecting to provide an accurate screening, by employing more values of  $\alpha$ , in what follows. All the other parameters are the same as in the case  $\alpha = 1$ . In Figure 4.8(b) we recognize a deviation from the Gutenberg-Richter law at large magnitudes: it is noticeable a sort of peak structure; the trend close to a straight line persists instead in the middle-small range of magnitude, in agreement with the empirical expectation. Finally, at smallest magnitude, as in the case analyzed before, a steep linear segment is observable due to the discreteness of the model. All these qualitative behaviours are consistent with previous works, for example [17, 66, 81, 102].

Now we want to discuss the importance of the parameter  $\alpha$  in terms of how much it can affect the results, by pointing out another interesting outcome of the  $\alpha$ -dependence. We said that the lower the value the higher the dissipation: as a result, in agreement with [16], we notice that in each earthquake the displacements become smaller. By assuming the smallest value employable, namely  $\alpha = 1$ , we can provide a qualitative proof of this property. As in [81] we consider the displacement of the location of the center of gravity during the time period  $[0, 10^4]$ . Our purpose consists in making a comparison between the cases  $\alpha = 1$  and  $\alpha = 4$ . Figure 4.9 shows the results and indicates that when  $\alpha$  is set to unity, the displacements are effectively smaller.

Let us proceed by investigating more accurately how the distribution of earthquakes changes when  $\alpha$  increases. In Figure 4.10 some distributions are plotted by assuming  $\alpha \in \{1, 1.5, 2, 3, 4\}$ , so that we have added three different  $\alpha$ -values

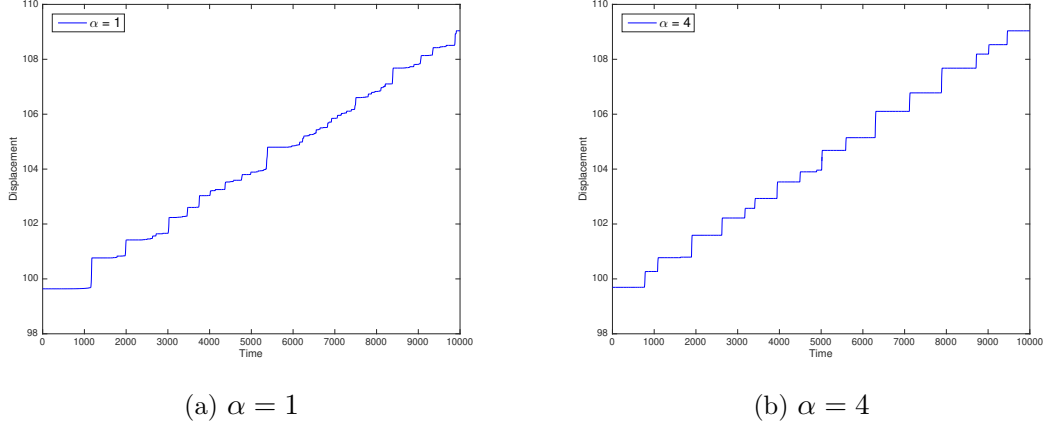


Figure 4.9. Displacement of the location of the center of gravity: comparison between  $\alpha = 1$  and  $\alpha = 4$ .

beyond those already analyzed. These values would be equally spaced if  $\alpha = 1.5$  was not considered, but we decided to provide a further value within  $[1, 2]$  in order to control better the evolution of the graph when  $\alpha$  is moving in this range. We are allowed to conclude that the peak structure mentioned above persists when  $\alpha \neq 1$  and that the slope, where there is a linear behaviour qualitatively in agreement with the Gutenberg-Richter law, is steeper as  $\alpha$  increases: it can be deduced simply by noticing that when  $\alpha = 1.5$  a flatter slope affects the distribution in the middle-small range of magnitude, while this slope becomes steeper whether  $\alpha$  increases.

Let us continue by making other comparisons of our results. We defined the magnitude  $M$  in (4.4) by introducing the decimal logarithm. Also in [81] something like this is performed. However, in order to allow further qualitative pairings with some works already mentioned (for example [17, 102]), we recast the results described above by using the natural logarithm to define the magnitude. The relationship (4.4) becomes

$$M_1 = \ln \left( \sum_{i=1}^N \Delta x_i \right),$$

where  $M_1$  denotes the magnitude. If the quantity  $P(M_1)$  is defined as we have done for  $P(M)$ , an analogue of Figure 4.10 is obtainable, qualitatively equivalent. We gave it a try and found a graph very similar to the correspondent plots exhibited in [102]. We also recognized that in our simulations the data, when  $\alpha = 1$ , crosses the other curves at  $M_1 \simeq 4$ , in agreement with the results in [102].

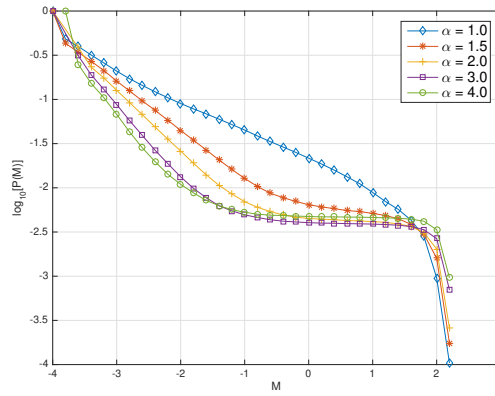
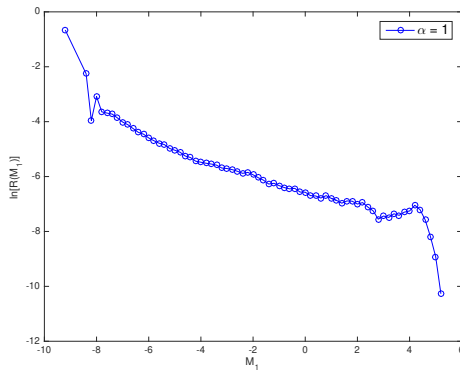
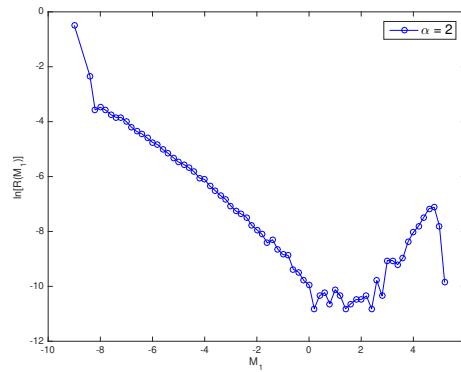


Figure 4.10. Earthquakes distribution for a system with 200 blocks: graph of the function  $M \mapsto \log_{10}[P(M)]$  with  $\alpha \in \{1, 1.5, 2, 3, 4\}$ . The other parameters used are listed in Table 4.2.



(a)  $\alpha = 1$



(b)  $\alpha = 2$

Figure 4.11. Distributions of magnitude for a system including 200 blocks: graph of the function  $M_1 \mapsto \ln[R(M_1)]$ ; comparison between  $\alpha = 1$  and  $\alpha = 2$ .

Finally, if we define another quantity,  $R(M_1)$ , as the rate of seismic events with magnitudes equal to  $M_1$ , operatively in a range such as  $[M_1, M_1 + dM_1]$ , we achieve the results shown in Figure 4.11. With the aim of expressing the qualitative behaviour affecting the dynamics when  $\alpha \neq 1$ , in Figure 4.11(b) we have chosen as example the value  $\alpha = 2$ : it is possible to explain the deviation from the Gutenberg-Richter law previously mentioned in terms of a peak structure, by pointing out that in this case large events are too frequent. These conclusions are consistent with those in [16, 17, 66].

## 4.4 Wave speed estimate and almost convergence

In the previous sections we have performed numerical simulations aimed at providing a comprehensive overview of the typical dynamics the Burridge-Knopoff model is ruled by, through an effective numerical method based on a Predictor-Corrector strategy. All these achievements define a helpful background to reach the core of our study: specifically, we take advantage of the discrete structure of the model in order to get results related to the propagating fronts theory, on the ground of the proceedings described before as far as the numerical discretization.

By means of some simple qualitative considerations, it is possible to recognize that the assessment of mechanisms hypothetically attributable to the traveling fronts field, is something worth working on in seismology and related applied mathematics. So far we have often pointed out how much the Burridge-Knopoff model behaviour is bound to be influenced by phenomena of perturbations spreading, due to the intrinsic structure of the system: indeed, the information about occurring events is conveyed by the connecting springs, allowing distant blocks slipping, within a chain reaction process in which each block can trigger its neighbors motion. This is aimed at reproducing realistic solicitations happening along faults, which are some strengthening geophysical evidences that some information is constantly being spreading.

From a mathematical point of view, a suitable analysis is needed in order to prove that such qualitative and empirical features might be framed by a systematic theory based on traveling fronts. In this respect, as pointed out by Muratov in [71], a class of systems consisting of elastic media and characterized by friction laws allowing the typical stick-slip phenomena, has been proved to be suitable for producing traveling fronts as shocks. Being these systems of great interest for their large usage within the seismological field, it follows that the potential overlapping involving traveling waves theory provides a solid ground for useful deeper analysis. In [71], by using the Coulomb friction law and taking into account a continuum version of the model, propagating fronts are investigated, specifically, their existence is shown and corresponding wave speed computation is performed.

Here, we wish to realize something similar by employing a different approach: basically we are interested in detecting a stable wave speed, that means recognizing the propagating fronts phenomenon, only by making use of the discrete version of the model provided with the velocity-weakening friction investigated so far. As a consequence, a wave speed estimate is needed: our choice falls on the formulation provided by LeVeque and Yee in [52] already exploited in this work, suitably modified and upgraded in order to get a version contextualized in this discrete field. For the ease of the reader, we recall the approximation previously employed,

that reads as

$$c_n = \frac{\Delta x}{[\phi]\Delta t} \sum_{i=1}^N (\phi_i^n - \phi_i^{n+1}), \quad (4.9)$$

where  $c_n$  is the space-averaged wave speed estimate, at time  $t^n$ , related to the traveling wave  $\phi$  approximated over a uniform spatio-temporal mesh ( $\Delta x$  and  $\Delta t$  are the fixed spatial and time steps, respectively), while  $[\phi] := \phi_+ - \phi_-$ , assuming  $\phi_+$  and  $\phi_-$  to be stationary states of  $\phi$ .

Our modified version of (4.9) arises from the requirement of dealing with a system of ODEs, thus implying some specific adjustments leading to the following formulation

$$c_n = \frac{1}{h[z]} \sum_{i=1}^N (z_i^n - z_i^{n-1}) \Delta x_i^n, \quad (4.10)$$

where  $[z] = z_N^n - z_1^n$  plays the role of the term including the stationary states in (4.9) and, as regards the quantity  $\Delta x_i^n$ , we have:

$$\Delta x_i^n = \begin{cases} z_2^n - z_1^n & \text{if } i = 1, \\ \frac{z_{i+1}^n - z_{i-1}^n}{2} & \text{if } 2 \leq i \leq N-1, \\ z_N^n - z_{N-1}^n & \text{if } i = N. \end{cases}$$

The relation (4.10) is again a space-averaged wave speed estimate for the velocity  $c$  evaluated at time  $t^n$ : the notation  $z_i^n$  is related to the position of the block  $i$  at time  $t^n$ ; the multi-valued function  $\Delta x_i^n$  is meant to be a measure of the distance between adjacent blocks, replacing the spatial contribution  $\Delta x$  involved in (4.9); finally, as in the simulations performed in the previous sections,  $h$  is a fixed time step, while  $N$  is the total number of blocks. We point out that, being needed a couple of temporal indices for each wave speed evaluation in (4.10), the resulting computed value might be equivalently referred to both the indices involved: that is why, as a convention, we decide to rely on the last temporal instant, for each couple, to relate the corresponding estimate.

In an attempt to start a preliminary test aimed at detecting useful information about the wave speed, our pressing purpose consists in considering the simplest conceivable trend for the velocity, that is  $c$  as a function of the discrete time  $t^n$ . As regards the parameters, we adopt the same quantities listed in Table 4.2 and select  $\alpha = 1$  among the available values, while, as far as the time period, we opt for  $[0, 10^5]$ . In Figure 4.12 the evolution for the wave speed is shown: although it is not possible to recognize a convergence towards a stable wave speed, from a qualitative point of view we can assert that this kind of behaviour is not surprising at all, due to its close similarity with respect to the plot in Figure 4.5(a) or in Figure 4.7(a). Indeed, all these graphs provide information about the velocity trend, that is

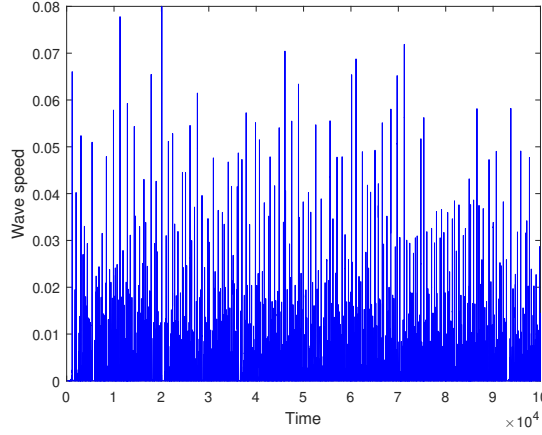


Figure 4.12. Wave speeds estimates trend for a system involving 200 blocks.

why getting profiles characterized by a collection of pronounced peaks, namely having reported some seismic events, is something consistent with our empirical expectation, regardless of the number of blocks involved. These kind of graphs, in which the velocity is heavily concentrated in peaks, are a logical consequence of the particular dynamics analyzed, whose specificity consists in its being deeply discontinuous. However the problem about the detection of a stable wave speed is still open: if on the one hand the plot in Figure 4.12 is something reasonable, on the other hand, speaking about the study of propagating fronts and their velocity, further analyses are needed.

A possibility consists in defining a more regular function and trying to justify the assumptions in terms of correspondence with respect to the real phenomena object of investigation. Let us define the following quantity:

$$\gamma_n = \frac{1}{n} \sum_{i=1}^n c_i. \quad (4.11)$$

For each  $n$ , the relation (4.11) takes into account the arithmetic mean of the first  $n$  available wave speed estimates. In Figure 4.13 we can see the results: a convergence towards an asymptotic threshold is now appreciable and the limit value numerically computed is  $L \simeq 0.00104$ .

At this stage, from the mathematical point view, a discussion is required: the stable wave speed provided by the limit  $L$  of the sequence  $\{\gamma_n\}$  is related to the averages convergence for the sequence  $\{c_n\}$ , that is why we have numerically proved the summability *in the sense of Cesaro*. Specifically, leaning on the *Cesaro Means Theorem* [90], it is known that if a sequence  $\{\beta_n\}$  is convergent, let us assume  $\lim_{n \rightarrow \infty} \beta_n = b$ , then, considering the sequence made by collecting the



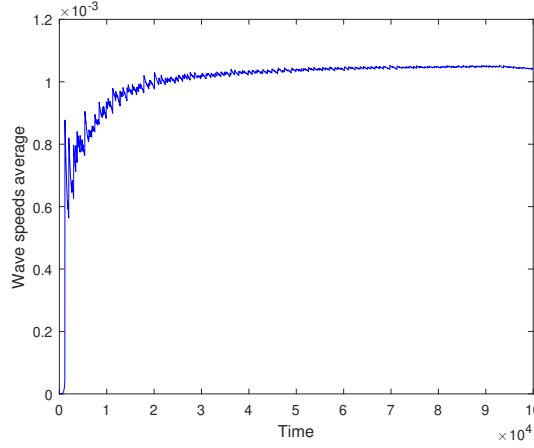


Figure 4.13. Wave speeds average from (4.11) as a function of the time  $t^n$  for a system involving 200 blocks.

corresponding averages, let us say  $\{\sigma_n\}$  such that  $\sigma_n = \frac{1}{n} \sum_{i=1}^n \beta_i$ , it happens that  $\lim_{n \rightarrow \infty} \sigma_n = b$ . In our case,  $L = \lim_{n \rightarrow \infty} \gamma_n = \lim_{n \rightarrow \infty} \frac{1}{n} \sum_{i=1}^n c_i$ , thus, although we have numerically proved that a convergence for the sequence  $\{c_n\}$  is not recognizable (see Figure 4.12), we can certainly state that, if a weaker convergence is verified, it has to happen towards the value  $L$ , being this threshold the limit for the averages sequence.

On the heels of this result, we are going to numerically prove the so-called *almost convergence* [8, 54] for the sequence  $\{c_n\}$ . To accomplish this purpose, let us introduce another average, as follows

$$\gamma_{p,n} = \frac{1}{n} \sum_{i=p}^{p+n-1} c_i, \quad (4.12)$$

which turns out to be equivalent to (4.11) if  $p = 1$ . By invoking the *Lorentz Theorem* [8, 54], it is possible to assert that the sequence  $\{c_n\}$  is said to be *almost convergent* (to  $L$ ) if and only if  $\lim_{n \rightarrow \infty} \gamma_{p,n} = L$  uniformly in  $p$ . We take advantage of this result and numerically test the almost convergence for  $\{c_n\}$  by computing the  $(p, n)$ -dependent mean for different choices of the parameter  $p$ , as a function of the discrete time  $t^n$ . The results are depicted in Figure 4.14 starting from the case  $p = 1$ , happening when the quantity  $\gamma_{p,n}$  in (4.12) perfectly matches  $\gamma_n$  in (4.11). The parameters exploited to carry out the numerical test are listed in Table 4.3. All the graphs clearly converge towards an asymptotic threshold, whose value is  $L \simeq 0.00104$ , namely the limit already recognized in Figure 4.13, thus testifying the almost convergence for  $\{c_n\}$ . This kind of outcome, involving the averages for the wave speeds sequence, provides an interesting interpretation in

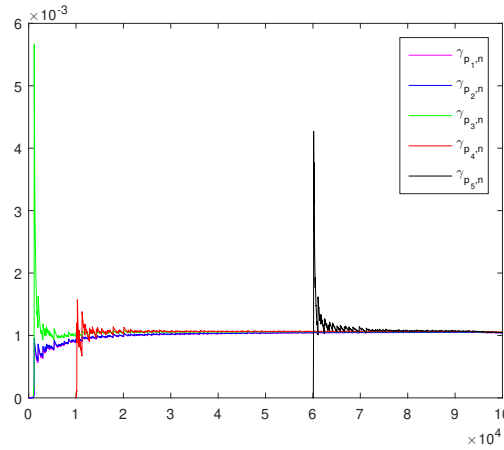


Figure 4.14. Wave speeds averages from (4.12) for different values of the parameter  $p$ , as a function of the time  $t^n$ ; the system involves 200 blocks.

Table 4.3: Values of  $p$  involved in the simulations and corresponding time instants.

Parameter $p$ choices					
$\mathbf{p}$	$p_1 = 1$	$p_2 = 10^5$	$p_3 = 10^6$	$p_4 = 10^7$	$p_5 = 6 \cdot 10^7$
$\mathbf{t}$	$10^{-3}$	$10^2$	$10^3$	$10^4$	$6 \cdot 10^4$

terms of real phenomena as well. Indeed, while the plot in Figure 4.12, reproducing the wave speed trend, can be described as a collection of mutually independent events, the function involving the wave speeds averages (4.12) and the related graphs in Figure 4.14 lead to imply a dependence from the past sequences. The latter interpretation is somehow more acceptable thinking about the mechanism of mutual induction affecting earthquakes along a fault and the reasonable influence that past earthquakes might have on future seismic events. Moreover, speaking about the traveling fronts theory, the presence of a stable threshold for the wave speeds averages is doubtless a powerful key point: it paves the way to state the existence of propagating fronts starting from the specific discrete version of the Burridge-Knopoff model provided with the velocity-weakening friction.

# Bibliography

- [1] Acary, V., Brogliato, B.: Numerical methods for nonsmooth dynamical systems: applications in mechanics and electronics, vol. 35. Springer Verlag (2008)
- [2] Alberghina, L., Gaglio, D., Moresco, R.M., Gilardi, M.C., Messa, C., Vanoni, M.: A Systems Biology road map for the discovery of drugs targeting cancer cell metabolism, *Curr. Pharm. Des.* **20**, 2648–2666 (2014)
- [3] Archetti, M.: Evolutionary dynamics of the Warburg effect: glycolysis as a collective action problem among cancer cells, *J. Theor. Biol.* **341**, 1–8 (2014)
- [4] Astanin, S., Preziosi, L.: Mathematical modeling of the Warburg effect in tumour cords, *J. Theor. Biol.* **258**, 578–590 (2009)
- [5] Bak, P., Tang, C., Wiesenfeld, K.: Self-organized criticality: an explanation of  $1/f$  noise, *Phys. Rev. Lett.* **59**(4), 381–384 (1987)
- [6] Bak, P., Tang, C.: Earthquakes as a self-organized critical phenomenon, *J. Geophys. Res.* **94**(B11), 15635–15637 (1989)
- [7] Barrière, G., Fici, P., Gallerani, G., Fabbri, F., Rigaud, M: Epithelial mesenchymal transition: a double-edged sword, *Clin. Transl. Med.* **4**(14), 1–6 (2015)
- [8] Bennett, G., Kalton, N.J.: Consistency theorems for almost convergence, *Trans. Amer. Math. Soc.* **198**, 23–43 (1974)
- [9] Bertolaso, M.: Philosophy of cancer. A dynamic and relational view. History, Philosophy and Theory of the Life Sciences 18. Springer Netherlands (2016)
- [10] Bertuzzi, A., Fasano, A., Gandolfi, A., Sinisgalli, C.: Necrotic core in EMT6/Ro tumour spheroids: is it caused by an ATP deficit?, *J. Theor. Biol.* **262**, 142–150 (2010)

- [11] Bianchini, L., Fasano, A.: A model combining acid-mediated tumour invasion and nutrient dynamics, *Nonlinear Anal. Real World Appl.* **10**(4), 1955–1975 (2009)
- [12] Bizzarri M., Cucina A., Conti F., D’Anselmi F.: Beyond the oncogene paradigm: understanding complexity in carcinogenesis, *Acta Biotheor.* **56**(3), 173–196 (2008)
- [13] Brace, W.F., Byerlee, J.D.: Stick-slip as a mechanism for earthquakes, *Science* **153**(3739), 990–992 (1966)
- [14] Burridge, R., Knopoff, L: Model and theoretical seismicity, *B. Seismol. Soc. Am.* **57**(3), 341–371 (1967)
- [15] Carlson, J.M., Langer, J.S.: Properties of earthquakes generated by fault dynamics, *Phys. Rev. Lett.* **62**(22), 2632–2635 (1989)
- [16] Carlson, J.M., Langer, J.S.: Mechanical model of an earthquake fault, *Phys. Rev. A* **40**(11), 6470–6484 (1989)
- [17] Carlson, J.M., Langer, J.S., Shaw, B.E., Tang, C.: Intrinisc properties of a Burridge-Knopoff model of an earthquake fault, *Phys. Rev. A* **44**(2), 884–897 (1991)
- [18] Carmona-Fontaine, C., Bucci, V., Akkari, L., Deforet, M., Joyce, J.A., Xavier, J.B.: Emergence of spatial structure in the tumor microenvironment due to the Warburg effect, *Proc. Natl. Acad. Sci. USA* **110**, 19402–19407 (2013)
- [19] Comte, J.C., Tchofo Dinda, P., Remoissenet, M.: Discrete Burridge-Knopoff model, with exact solitonic or compactlike traveling wave solution, *Phys. Rev. E* **65**, 026615 (2002)
- [20] Davies, P.C., Demetrius, L., Tuszynski, J.A.: Cancer as a dynamical phase transition, *Theor. Biol. Med. Model.* **8**, 1–30 (2011)
- [21] de Arcangelis, L., Godano, C., Grasso, J.R., Lippiello, E.: Statistical physics approach to earthquake occurrence and forecasting, *Phys. Rep.* **628**, 1–91 (2016)
- [22] Doglioni, C., Carminati, E., Petricca, P., Riguzzi, F.: Normal fault earthquakes or graviquakes, *Sci. Rep.* **5**, 12110 (2015)
- [23] Enderling, H., Anderson, A.R., Chaplain, M.A., Rowe, G.W.: Visualisation of the numerical solution of partial differential equation systems in three space dimensions and its importance for mathematical models in biology, *Math. Biosci. Eng.* **3**(4), 571–582 (2006)

- [24] Erickson, B., Birnir, B., Lavallée, D.: A model for aperiodicity in earthquakes, *Nonlinear Proc. Geoph.* **15**, 1–12 (2008)
- [25] Erickson, B., Birnir, B., Lavallée, D.: Periodicity, chaos and localization in a Burridge-Knopoff model of an earthquake with rate-and-state friction, *Geophys. J. Int.* **187**, 178–198 (2011)
- [26] Fasano, A., Herrero, M.A., Rodrigo, M.R.: Slow and fast invasion waves in a model of acid-mediated tumour growth, *Math. Biosci.* **220**(1), 45–56 (2009)
- [27] Fife, P.C., McLeod, J.B.: The approach of solutions of nonlinear diffusion equations to travelling front solutions, *Arch. Ration. Mech. Anal.* **65**, 335–361 (1977)
- [28] Folkman, J., Hochberg, M.: Self-regulation of growth in three dimensions, *J. Exp. Med* **38**, 745–753 (1973)
- [29] Fouad, A.M.: A kinetic view of acid-mediated tumor invasion, *Eur. Biophys. J.* **47**(2), 185–189 (2018)
- [30] Gatenby, R.A., Gawlinski, E.T.: A reaction-diffusion model of cancer invasion, *Cancer Res.* **56**, 5745–5753 (1996)
- [31] Gatenby, R.A., Maini, P.K., Gawlinski, E.T.: Analysis of tumor as an inverse problem provides a novel theoretical framework for understanding tumor biology and therapy, *Appl. Math. Lett.* **15**, 339–345 (2002)
- [32] Gatenby, R.A., Gawlinski, E.T.: The glycolytic phenotype in carcinogenesis and tumor invasion: insights through mathematical models, *Cancer Res.* **63**, 3847–3854 (2003)
- [33] Gatenby, R.A., Gillies, R.J.: Why do cancers have high aerobic glycolysis?, *Nat. Rev. Cancer* **4**, 891–899 (2004)
- [34] Gatenby, R.A., Gawlinski, E.T., Gmitro, A.F., Kaylor, B., Gillies, R.J.: Acid-mediated tumour invasion: a multidisciplinary study, *Cancer Res.* **66**, 5216–5223 (2006)
- [35] Gatenby, R.A., Gillies, R.J.: Glycolysis in cancer: a potential target for therapy, *Int. J. Biochem. Cell Biol.* **39**, 1358–1366 (2007)
- [36] Gesztelyi, R., Zsuga, J., Kemeny-Beke, A., Varga, B., Juhasz, B., Tosaki, A.: The Hill equation and the origin of quantitative pharmacology, *Arch. Hist. Exact Sci.* **66**, 427–438 (2012)

- [37] Gilding, B.H., Kersner, R.: Travelling waves in nonlinear diffusion-convection equations. Progress in Nonlinear Differential Equations and Their Applications 60. Springer Basel AG (2004)
- [38] Green, M.W., Sleeman, B.D.: On FitzHugh's nerve axon equations, *J. Math. Biol.* **1**, 153–163 (1974)
- [39] Guglielmi, N., Hairer, E.: Classification of hidden dynamics in discontinuous dynamical systems, *SIAM J. Appl. Dyn. Syst.* **14**(3), 1454–1477 (2015)
- [40] Gutenberg, B., Richter, C.F.: Magnitude and energy of earthquakes, *Ann. Geophys.* **9**(1), 1–15 (1956)
- [41] Hadeler, K.P., Rothe, F.: Travelling fronts in nonlinear diffusion equations, *J. Math. Biol.* **2**, 251–263 (1975)
- [42] Holder, A.B., Rodrigo, M.R., Herrero, M.A.: A model for acid-mediated tumour growth with nonlinear acid production term, *Appl. Math. Comput.* **227**, 176–198 (2014)
- [43] Holling, C.S.: Some characteristics of simple types of predation and parasitism, *Can. Entomol.* **91**(7), 385–398 (1959)
- [44] Jones, M.A., Song, B., Thomas, D.M.: Controlling wound healing through debridement, *Math. Comput. Model.* **40**, 1057–1064 (2004)
- [45] Kawamura, H., Hatano, T., Kato, N., Biswas, S., Chakrabarti, B.K.: Statistical physics of fracture, friction, and earthquakes, *Rev. Mod. Phys.* **84**(2), 839–884 (2012)
- [46] Keener, J., Sneyd, J.: Mathematical physiology, vol. 8. Springer Verlag, New York (1998)
- [47] Kolditz, O.: Computational methods in environmental fluid mechanics. Springer, Berlin, Heidelberg (2002)
- [48] Kunze, M., Küpper, T.: Qualitative bifurcation analysis of a non-smooth friction-oscillator model, *Z. Angew. Math. Phys.* **48**(1), 87–101 (1997)
- [49] Langer, J.S., Carlson, J.M., Myers, C.R., Shaw, B.E.: Slip complexity in dynamic models of earthquake faults, *Proc. Natl. Acad. Sci. USA.* **93**, 3825–3829 (1996)
- [50] Lattanzio, C., Mascia, C., Plaza, R.G., Simeoni, C.: Analytical and numerical investigation of traveling waves for the Allen-Cahn model with relaxation, *Math. Models Methods Appl. Sci.* **26**, 931–985 (2016)

- [51] Lattanzio, C., Mascia, C., Plaza, R.G., Simeoni, C.: Kinetic schemes for assessing stability of traveling fronts for the Allen-Cahn equation with relaxation, *Appl. Numer. Math.* **141**, 234–247 (2019)
- [52] LeVeque, R.J., Yee, H.C.: A study of numerical methods for hyperbolic conservation laws with stiff source terms, *J. Comput. Phys.* **86**(1), 187–210 (1990)
- [53] LeVeque, R.J.: Finite difference methods for ordinary and partial differential equations. Steady-state and time-dependent problems. Society for Industrial and Applied Mathematics (SIAM) (2007)
- [54] Lorentz, G.G.: A contribution to the theory of divergent sequences, *Acta Math.* **80**(1), 167–190 (1948)
- [55] Málaga, C., Minzoni, A., Plaza, R.G., Simeoni, C.: A chemotactic model for interaction of antagonistic microflora colonies: front asymptotics and numerical simulations, *Stud. Appl. Math.* **130**(3), 264–294 (2013)
- [56] Malaguti, L., Marcelli, C.: Sharp profiles in degenerate and doubly degenerate Fisher-KPP equations, *J. Differential Equations* **195**, 471–496 (2003)
- [57] Mascia, C., Moschetta, P., Simeoni, C.: Phase transitions of biological phenotypes by means of a prototypical PDE model, *Commun. Appl. Ind. Math.*, (2019) (in press)
- [58] Mascia, C., Moschetta, P.: Numerical evidences of almost convergence of wave speeds for the Burridge-Knopoff model (submitted)
- [59] Masel, R.I.: Principles of adsorption and reaction on solid surfaces. Wiley Series in Chemical Engineering 3. John Wiley & Sons (1996)
- [60] McGillen, J.B., Gaffney, E.A., Martin, N.K., Maini, P.K.: A general reaction-diffusion model of acidity in cancer invasion, *J. Math. Biol.* **68**(5), 1199–1224 (2014)
- [61] Medina, M.Á.: Systems biology for molecular life sciences and its impact in biomedicine, *Cell. Mol. Life Sci.* **70**, 1035–1053 (2013)
- [62] Medina, M.Á.: Mathematical modeling of cancer metabolism, *Crit. Rev. Oncol. Hematol.* **124**, 37–40 (2018)
- [63] Mojtahedi, M., Skupin, A., Zhou, J., Castaño, I.G., Leong-Quong, R.Y.Y., Chang, H., Trachana, K., Giuliani, A., Huang, S.: Cell fate decision as high-dimensional critical state transition, *PLOS Biol.* **14**(12), p. e2000640 (2016)

- [64] Monod, J., Wyman, J., Changeux, J.P.: On the nature of allosteric transitions: a plausible model, *J. Mol. Biol.* **12**, 88–118 (1965)
- [65] Morales, J.E., James, G., Tonnelier, A.: Solitary waves in the excitable Burridge-Knopoff model, *Wave Motion* **76**, 103–121 (2018)
- [66] Mori, T., Kawamura, H.: Simulation study of the one-dimensional Burridge-Knopoff model of earthquakes, *J. Geophys. Res.* **111**, B07302 (2006)
- [67] Mori, T., Kawamura, H.: Simulation study of earthquakes based on the two-dimensional Burridge-Knopoff model with long-range interactions, *Phys. Rev. E* **77**, 051123 (2008)
- [68] Mori, T., Kawamura, H.: Simulation study of the two-dimensional Burridge-Knopoff model of earthquakes, *J. Geophys. Res.* **113**, B06301 (2008)
- [69] Mori, T., Kawamura, H.: Spatiotemporal correlations of earthquakes in the continuum limit of the one-dimensional Burridge-Knopoff model, *J. Geophys. Res.* **113**, B11305 (2008)
- [70] Moschetta, P., Simeoni, C.: Numerical investigation of the Gatenby-Gawlinski model for acid-mediated tumour invasion, *Rend. Mat. Appl.* **40**, 257–287 (2019)
- [71] Muratov, C.B.: Traveling wave solutions in the Burridge-Knopoff model, *Phys. Rev. E* **59**(4), 3847–3857 (1999)
- [72] Newman, W.I.: Some exact solutions to a non-linear diffusion problem in population genetics and combustion, *J. Theor. Biol.* **85**, 325–334 (1980)
- [73] Newman, W.I.: The long-time behavior of the solution to a non-linear diffusion problem in population genetics and combustion, *J. Theor. Biol.* **104**, 473–484 (1983)
- [74] Olami, Z., Feder, H.J.S., Christensen, K.: Self-organized criticality in a continuous, nonconservative cellular automaton modeling earthquakes, *Phys. Rev. Lett.* **68**(8), 1244–1248 (1992)
- [75] Pera, D., Màlaga, C., Simeoni, C., Plaza, R.G.: On the efficient numerical simulation of heterogeneous anisotropic diffusion models for tumor invasion using GPUs, *Rend. Mat. Appl.* **40**, 233–255 (2019)
- [76] Perumpanani, A.J., Sherratt, J.A., Norbury, J., Byrne, H.M.: A two parameter family of travelling waves with a singular barrier arising from the modelling of the extracellular matrix mediated cellular invasion, *Physica D: Nonlinear Phenomena* **126**, 145–159 (1999)



- [77] Quarteroni, A., Sacco, R., Saleri, F.: Numerical mathematics, vol. 37. Springer Verlag (2000)
- [78] Quarteroni, A.: Numerical models for differential problems. Third edition. Modeling, Simulation and Applications 16. Springer, Cham (2017)
- [79] Quiroga, A.A.I., Fernández, D., Torres, G.A., Turner, C.V.: Adjoint method for a tumor invasion PDE-constrained optimization problem in 2D using adaptive finite element method, *Appl. Math. Comput.* **270**, 358–368 (2015)
- [80] Ruina, A.: Slip instability and state variable friction laws, *J. Geophys. Res.* **88**(B12), 10359–10370 (1983)
- [81] Saito, T., Matsukawa, H.: Size dependence of the Burridge-Knopoff model, *J. Phys. Conf. Ser.* **89**, 012016 (2007)
- [82] Sánchez-Garduño, F., Maini, P.K.: Existence and uniqueness of a sharp travelling wave in degenerate non-linear diffusion Fisher-KPP equations, *J. Math. Biol.* **33**, 163–192 (1994)
- [83] Sánchez-Garduño, F., Maini, P.K.: An approximation to a sharp type solution of a density-dependent reaction-diffusion equation, *Appl. Math. Lett.* **7**, 47–51 (1994)
- [84] Sánchez-Garduño, F., Maini, P.K.: Traveling wave phenomena in some degenerate reaction-diffusion equations, *J. Differential Equations* **117**, 281–319 (1995)
- [85] Sánchez-Garduño, F., Maini, P.K., Kappos, M.E.: A shooting argument approach to a sharp-type solution for nonlinear degenerate Fisher-KPP equations, *IMA J. Appl. Math.* **57**, 211–221 (1996)
- [86] Sánchez-Garduño, F., Maini, P.K.: Travelling wave phenomena in non-linear diffusion degenerate Nagumo equations, *J. Math. Biol.* **35**, 713–728 (1997)
- [87] Scholz, C.H.: The Mechanics of earthquakes and faulting. Cambridge University Press (1990)
- [88] Scholz, C.H.: Earthquakes and friction laws, *Nature* **391**, 37–42 (1998)
- [89] Shamsi, M., Saghafian, M., Dejam, M., Sanati-Nezhad, A.: Mathematical modeling of the function of Warburg effect in tumor microenvironment, *Sci. Rep. Nature Publishing Group* **8**, 1–12 (2018)

- [90] Shawyer, B.L.R., Watson, B.: Borel's methods of summability: theory and applications. Oxford University Press (1994)
- [91] Sherratt, J.A., Marchant, B.P.: Algebraic decay and variable speeds in wave-front solutions of a scalar reaction-diffusion equation, *IMA J. Appl. Math.* **56**, 289–302 (1996)
- [92] Simeoni, C., Dinicola, S., Cucina, A., Mascia, C., Bizzarri, M.: Systems Biology approach and Mathematical Modeling for analyzing phase-space switch during epithelial-mesenchymal transition, Bizzarri M. (eds) *Systems Biology, Methods in Molecular Biology* **1702**, Humana Press, New York, 95–123 (2018)
- [93] Smallbone, K., Gavaghan, D.J., Gatenby, R.A., Maini, P.K.: The role of acidity in solid tumour growth and invasion, *J. Theor. Biol.* **235**(4), 476–484 (2005)
- [94] Smallbone, K., Gatenby, R.A., Maini, P.K.: Mathematical modelling of tumour acidity, *J. Theor. Biol.* **255**, 106–112 (2008)
- [95] Thiery, J.P., Sleeman, J.P.: Complex networks orchestrate epithelial-mesenchymal transitions, *Nat. Rev. Mol. Cell Biol.* **7**(2), 131–142 (2006)
- [96] van Saarloos, W.: Front propagation into unstable states: marginal stability as a dynamical mechanism for velocity selection, *Phys. Rev. A* **37**(1), 211–229 (1988)
- [97] Warburg, O.: The metabolism of tumors. Arnold Constable, London (1930)
- [98] Warburg, O.: On the origin of cancer cells, *Science* **123**, 309–314 (1956)
- [99] Weiss, J.N.: The Hill equation revisited: uses and misuses, *FASEB J.* **11**(11), 835–841 (1997)
- [100] Wesseling, P.: Principles of computational fluid dynamics. Springer, Berlin, Heidelberg (2001)
- [101] Xia, J., Gould, H., Klein, W., Rundle, J.B.: Near-mean-field behavior in the generalized Burridge-Knopoff earthquake model with variable-range stress transfer, *Phys. Rev. E* **77**, 031132 (2008)
- [102] Xiong, X., Kikuuwe, R., Yamamoto, M.: Implicit Euler simulation of one-dimensional Burridge-Knopoff model of earthquakes with set-valued friction laws, *Adv. Comput. Math.* **41**(6), 1039–1057 (2015)

- [103] Xu, J., Lamouille, S., Derynck, R.: TGF- $\beta$ -induced epithelial to mesenchymal transition, *Cell Res.* **19**(2), 156–172 (2009)
- [104] Yao, D., Dai, C., Peng, S.: Mechanism of the Mesenchymal-Epithelial Transition and its relationship with metastatic tumor formation, *Mol. Cancer Res.* **9**(12), 1608–1620 (2011)



# Sitography

- [105] <https://www.spandidos-publications.com/10.3892/ol.2016.5369>
- [106] <https://it.mathworks.com/products/matlab.html>
- [107] <http://luise.me/effetto-warburg-87/>
- [108] <https://www.comsol.it/>
- [109] <https://www.paraview.org/>
- [110] <https://slideplayer.com/slide/5355737/>
- [111] <https://ngmedicine.com/could-cancer-be-a-metabolic-disease/>
- [112] <http://www2.econ.iastate.edu/classes/econ308/tesfatsion/SandpileCA.Winslow97.htm>
- [113] <https://www.sbglab.org>